Study of Biaxial Fatigue Behavior of Fiber Reinforced Polymers Under Tensile and Shear Loadings

by

Raghuram Mandapati

A dissertation submitted in partial fulfillment
of the requirements for the degree of
Doctor of Philosophy
(Automotive Systems Engineering)
in the University of Michigan-Dearborn
2016

Doctoral Committee:

Professor P.K. Mallick, Chair
Associate Professor Hong-Tae Kang
Professor Elsayed Orady
Associate Professor German Reyes-Villanueva

DEDICATION

To three wonderful human beings; my mother, my sister and my wife.

ACKNOWLEDGMENTS

First and foremost, I would like sincerely thank my advisor Dr. P. K. Mallick for having patiently supported me throughout my thesis. Without his technical, financial and moral support this work could never have started. I am indebted to him for having me taught everything I know about research.

I also thank my thesis committee members; Dr. Kang, Dr. Orady and Dr. Reyes for their help during this work.

I would like to thank my family and close friends for having encouraged me at every step of this beautiful learning journey. I cannot even imagine coming this far without their strong and unconditional support.

TABLE OF CONTENTS

LIST OF TABLES

LIST OF FIGURES

ABSTRACT

Fiber reinforced polymers are used in many structural applications in the aerospace and automotive industries because of their high strength to weight and high modulus to weight ratios. In many of these applications, they are used as thin laminated panels comprising of multiple layers of continuous fibers embedded in a polymer matrix. In general, these laminates behave as an orthotropic material and their properties are direction-dependent. While their uniaxial static and fatigue characteristics have been studied extensively, their biaxial static and fatigue characteristics are not well established. One reason for this is the difficulty of conducting biaxial tests, especially under cyclic loading conditions. The objectives of the current research are two folds: (1) develop a biaxial test method that can be applied to a range of normal and shear loadings, and (2) study the biaxial fatigue behavior of a fiber reinforced polymer laminate using the new test method.

The test method developed in this research is based on a butterfly-shaped Arcan specimen. The versatility of the Arcan specimen is that it can be utilized for testing materials under uniaxial normal loading, shear loading or a combination of in-plane normal and shear loadings. The laminate considered in this study was a $[0/90/0_4/\underline{0}]_S$ E-glass/epoxy. Finite element analysis of a butterfly-shaped Arcan specimen was conducted first to establish its optimum geometry and delineate the importance of the stiffness of the test fixture on the stresses in the significant section of the specimen. An Arcan loading fixture was designed with the capability of loading of flat laminate specimens under various combinations of in-plane tensile and shear stresses. Quasi-static and fatigue tests were conducted with four different specimen configurations containing either 0, 30, 45 or 90^o fiber orientations in the outer layers. The quasi-static strength followed a quadratic failure envelope on a normal stress-shear stress plane. Biaxial fatigue tests were conducted under combined tensile and shear stresses to determine the effect of biaxiality on the fatigue performance of the laminate. Development of fatigue

damage under biaxial loading was also studied. A new fatigue life prediction model was proposed that can be used to account for the effect of biaxiality on the fatigue life of fiber reinforced polymer laminates.

CHAPTER 1 : INTRODUCTION

1.1 Introduction

Fiber reinforced polymers (FRP) are used in many different structural forms and applications in the aircraft, space, automotive, marine, sports and many other industries. Their use in engineering and structural applications has increased in the last few decades owing to their higher strength-to-density ratio, higher modulus-to-density ratio, design flexibility and weight saving potential compared to conventional materials, such as steel and aluminum alloys. A recent example of their increased use in the aircraft industry can be seen in Boeing 787 Dreamliner with 50% of its primary structure made of carbon fiber reinforced epoxy. The application of fiber reinforced polymers in automotive structures is also on the rise. To meet the increasingly demanding Corporate Average Fuel Economy (CAFE) standard in the USA and similar regulations in other countries, the automakers worldwide are developing materials, processes and test procedures that may allow them to substitute fiber reinforced polymers for steel in automotive body structures and body panels.

Fiber reinforced polymers are composed of two major parts, one being the fiber, which imparts the strength, modulus and other mechanical properties to the resulting FRP and the second being the matrix, which essentially holds the fibers in place and acts as the load transfer agent between the fibers. It is important to note that the mechanical properties of the resulting composite are in general intermediate between those of the fibers and the matrix. Their mechanical properties also depend on the fiber orientation angle with respect to the loading angle.

The applications of FRP are found in automotive, aerospace, sporting goods, wind power, civil engineering and many other industries. With ever-growing increase in the demand and application of these materials, it is exceedingly important to understand

their mechanical behavior to the greatest extent possible. Unlike conventional metals, which are isotropic, majority of fiber reinforced polymers are anisotropic or directional in nature. Their failure modes are also quite distinct from the ones observed in isotropic materials. Because of their directional properties, special design and test procedures must be involved while developing and fabricating components made of fiber reinforced polymers.

Over the past few decades, research has been conducted in various areas related to fiber reinforced polymers to understand their mechanical behavior under static and dynamic loading conditions. Understanding fatigue behavior of fiber reinforced polymers is an important area of research and is needed to affirm that fiber reinforced polymer components subjected to cyclic loading have an appropriate safe-life design. The anisotropic nature of fiber reinforced polymers is a factor which affects the complexity of their fatigue behavior. Lot of research has and is being carried out around the world to add to the fatigue knowledge database of fiber reinforced polymers. This includes developing newer test methods, which can determine the fatigue behavior of these materials, and fatigue life models, which can predict the material behavior under test or real life conditions.

Fatigue behavior of fiber reinforced polymers under uniaxial cycling loading has been studied extensively by numerous researchers. It has been shown that fatigue S-N diagrams as well as fatigue failure modes depend on the fiber and matrix type, fiber volume fraction, fiber orientation angle, fiber-matrix interface characteristics, mode of cyclic loading (e.g., tension-tension and tension-compression), and frequency of cycling. Reviews of uniaxial fatigue behavior are available in many references [1–12]. In comparison, biaxial fatigue of fiber reinforced polymers has received much less attention, mainly because of the complexity in conducting biaxial fatigue tests. Most of the studies reported in literature on the biaxial fatigue behavior of fiber reinforced polymers have used thin-walled tubular specimens under combined axial tension and torsion or axial tension and internal pressure. Relatively few studies have considered flat plates or panels; yet vast majority of the fiber reinforced polymers used today are in the form of thin laminated plates. With laminated plates, the most common biaxial test method

includes a combination of mutually perpendicular normal stresses applied on cruciform specimens. The effect of the combination of normal and shear stresses on the fatigue behavior of laminated fiber reinforced polymer plates has not been studied in the past. Since fiber reinforced polymers are relatively weak in shear loading, it is important to consider the effect of shear loading on their biaxial fatigue behavior.

The objective of the current research is to study the biaxial fatigue behavior of a glass fiber reinforced epoxy laminate under the combined effect of normal and shear loadings. The test method developed and followed in this research is based on Arcan specimens and can be applied to other laminated composites. This chapter includes a brief review of biaxial fatigue tests, biaxial fatigue data and the models developed to predict biaxial fatigue failure of fiber reinforced composites.

1.2 Background

A laminate is made of a stack of consolidated laminae in which fiber orientation angle may vary from lamina to lamina. Figure 1-1 shows a thin rectangular fiber reinforced composite lamina whose major dimensions are described with respect to x and y axes. Fibers in the lamina are oriented parallel to axis 1, which is inclined at an angle $+\theta$ (measured counter-clockwise) from the x-axis. The 1-2-z and x-y-z are two right-handed coordinate systems where 1-2 are the principal material directions and x-y are the loading directions.

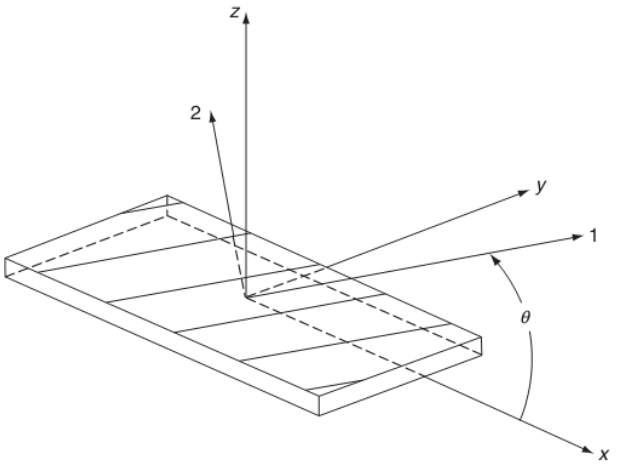

Figure 1-1: Loading axes and principal material directions

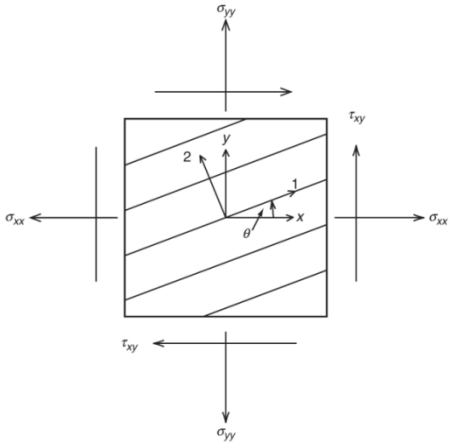

Figure 1-2: Lamina under plane stress condition

1.2.1 Biaxial Loading

Biaxial loading on a thin fiber reinforced lamina can be considered at two levels: (1) external level and (2) internal level. The external level includes the externally applied stresses in the x-y plane, such as σ_{xx}, σ_{yy} and τ_{xy}, on the lamina as shown in Figure 1-2. The stress biaxiality ratios at the external level can be expressed as:

$$\lambda_y = \frac{\sigma_{yy}}{\sigma_{xx}},$$
$$\lambda_{xy} = \frac{\tau_{xy}}{\sigma_{xx}}.$$

The external stress biaxiality creates an internal stress biaxiality due to the principal material directions being different from the external loading directions. This can be seen by transforming stresses σ_{xx}, σ_{yy} and τ_{xy} in the x-y directions due to external loads into internal stresses σ_{11}, σ_{22} and τ_{12} along the 1-2 directions using Equation 1.1 [12], [13].

$$\begin{aligned} \sigma_{11} &= \sigma_{xx}cos^2\theta + \sigma_{yy}sin^2\theta + 2\tau_{xy}cos\theta sin\theta \\ \sigma_{22} &= \sigma_{xx}sin^2\theta + \sigma_{yy}cos^2\theta - 2\tau_{xy}cos\theta sin\theta \\ \tau_{12} &= \left(-\sigma_{xx} + \sigma_{yy}\right)cos\theta sin\theta + \tau_{xy}(cos^2\theta - sin^2\theta) \end{aligned} \quad (1.1)$$

The stress biaxiality ratios at the internal level can be expressed as:

$$\lambda_2 = \frac{\sigma_{22}}{\sigma_{11}}$$
$$\lambda_{12} = \frac{\tau_{12}}{\sigma_{11}}$$

It is seen from Equation (1.1) that depending on the value of θ, a uniaxial stress condition with only σ_{xx} acting on the lamina can produce an internal biaxial stress state in the lamina. This phenomenon has been further detailed in Figure 1-3, which shows the variation of internal stress components σ_{11}, σ_{22} and τ_{12} with increasing fiber orientation angle in response to an external uniaxial stress σ_{xx}. Longitudinal normal stress, σ_{11}, decreases from the highest value at θ = 0° and becomes zero at θ = ±90°, whereas transverse normal stress, σ_{22}, does the opposite, reaching maximum values at θ = ±90° and becoming zero at θ = 0°. The magnitude of shear stress, τ_{12}, is maximum at θ = ±45° and zero at both θ = 0° and ±90°. It is worth noticing that the internal normal stresses are symmetric about θ = 0°, whereas the internal shear stress is anti-symmetric.

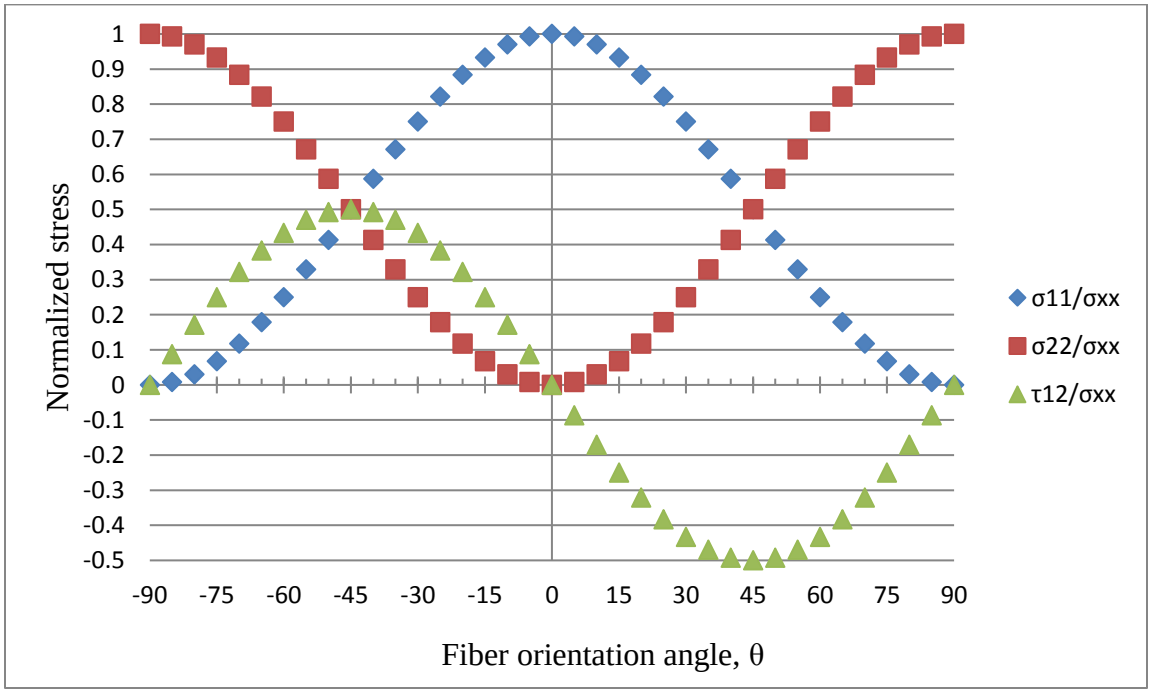

Figure 1-3: Internal stress components (normalized with respect to σ_{xx}) at different fiber orientation angles.

1.2.2 Biaxial Fatigue Tests

Several different biaxial fatigue test methods have been used for fiber reinforced composites. This section will briefly review these test methods and the next section will discuss the fatigue test data obtained from these tests.

a) Off-Axis Specimens

An off-axis specimen is shown in Figure 1-4. It is called off-axis due to the fact that the fibers are oriented at an angle θ from the loading axis in the x-direction. This is the simplest test method used to determine mechanical properties of fiber reinforced composites.

As shown in Equation (1.1) and Figure 1.3, a uniaxial tensile stress σ_{xx} on an off-axis specimen in which $0° < \theta < 90°$ will create an internal biaxial stress condition in the lamina. For a given value of σ_{xx}, the relative magnitudes of the internal stresses, σ_{11}, σ_{22} and τ_{12}, will depend on the fiber orientation angle θ. Thus, using the off-axis specimen, it is possible to create a biaxial stress condition in the lamina in which all three internal stress components will exist producing the following internal biaxiality stress ratios.

$$\begin{aligned} \lambda_2 &= \tan^2\theta \\ \lambda_{12} &= -\tan\theta \end{aligned} \tag{1.2}$$

However, due to normal stress-shear strain coupling, a shear strain γ_{xy} is developed as shown in Equation 1.3.

$$\begin{aligned} \varepsilon_{xx} &= \frac{\sigma_{xx}}{E_{xx}} \\ \varepsilon_{yy} &= -\nu_{xy}\frac{\sigma_{xx}}{E_{xx}} \\ \gamma_{xy} &= -m_x\sigma_{xx} \end{aligned} \tag{1.3}$$

where, ε_{xx}, ε_{yy} and γ_{xy} are normal and shear strains in the x-y directions, E_{xx} is the modulus of elasticity in the x-direction, ν_{xy} is the major Poisson's ratio, and m_x is called the co-efficient of mutual influence. As a result of the shear strain component γ_{xy}, the specimen, which is clamped at both ends, will tend to show twisting deformation.

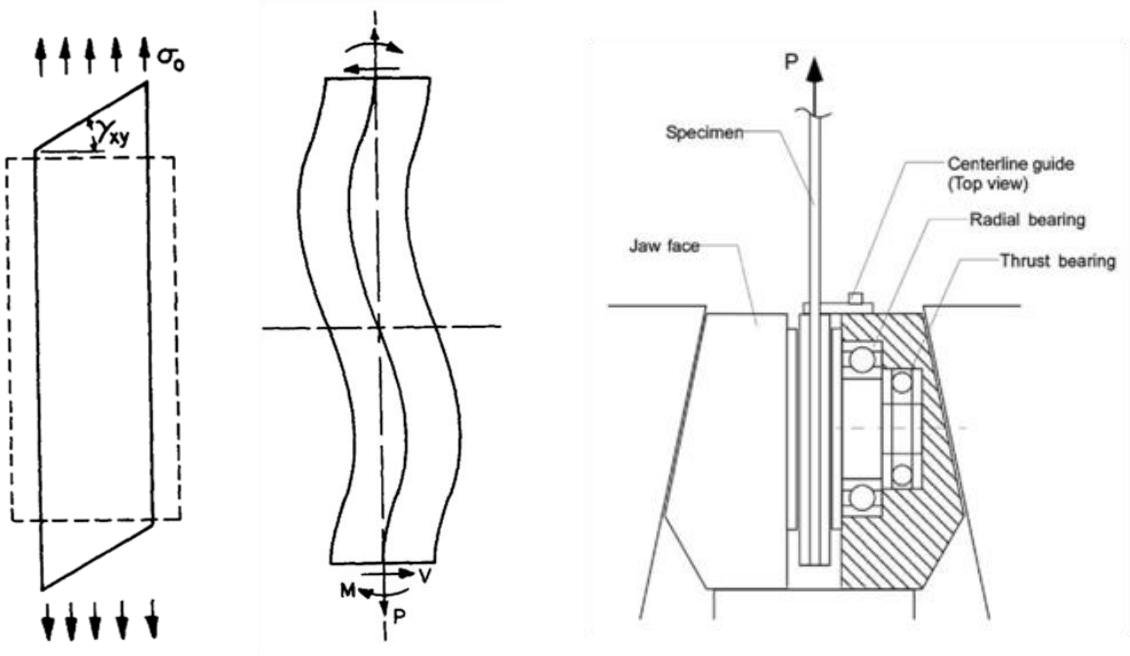

Figure 1-4: (a) Uniform stress state [1] (b) Effect of clamped ends [1] (c) Rotating grips used to allow free expansion along shear direction[2]

To eliminate the extraneous deformation and twisting moment, the off-axis specimens require a special clamping device which permits rotation of the ends while the test is in progress, in the absence of which the specimen tends to curve. Pagano and Halpin [1] were the first to report this behavior of orthotropic materials both theoretically and experimentally by using nylon-reinforced rubber under uniaxial loading. This special requirement is a direct result of the fact that even though a uniaxial load is applied, it actually produces a shear component. Unless the grips used for the off axis test allow rotation (Figure 1-4(c)) the test results may be in serious error.

The off-axis specimens have been utilized for the determination of both static and fatigue strengths of fiber reinforced composites [1–12], [14], [15]. Since the off-axis test method can evaluate mechanical properties only under uniaxial loads, it limits the internal stress biaxiality ratios to single values for any given lamina orientation angle, and therefore, the test data generated from these tests fill a very limited portion of the failure envelope, hence preventing its use to a large extent for fatigue response determination.

Also, an off-axis test method using uniaxial loading does not truly represent the real loading scenarios where the external stresses may be biaxial in nature, and therefore the use of fatigue data obtained from such a test may result in oversimplification causing the design to be either too conservative or too weak. The need to determine fatigue response of fiber reinforced polymers under externally applied biaxial loads led to the development of the following two test methods.

b) Cruciform Specimens

Cruciform specimens and the testing apparatus shown in Figure 1-5 allow the application of two normal loads in two mutually perpendicular directions, thus creating an external biaxial normal stress condition. The two normal loads can be applied independently, not only with respect to their magnitudes but also their directions, hence being able to generate data which covers a larger portion of the failure envelope.

Radon and Wachnicki [16] used cruciform specimens to examine fatigue crack growth of chopped E-glass strand mat reinforced polyester under various biaxiality ratios and in-phase tension. They observed that the embedded cracks followed the original direction for biaxiality ratio (λ_y) up to 1, however for $\lambda_y > 1$ the embedded crack followed a path parallel to the direction of the maximum load.

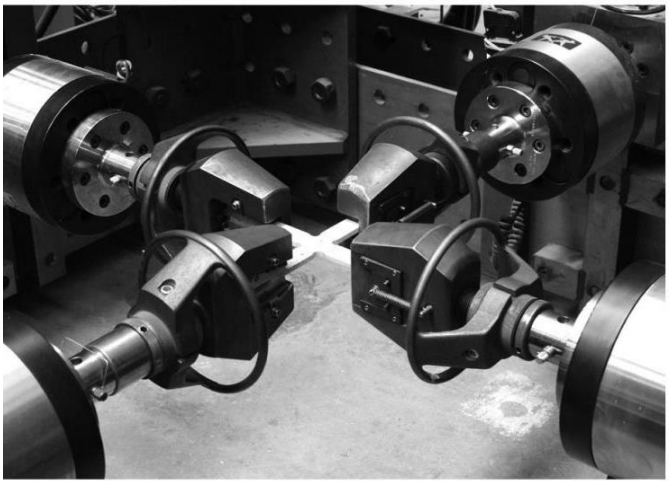

Figure 1-5: Cruciform specimen and the loading device[17]

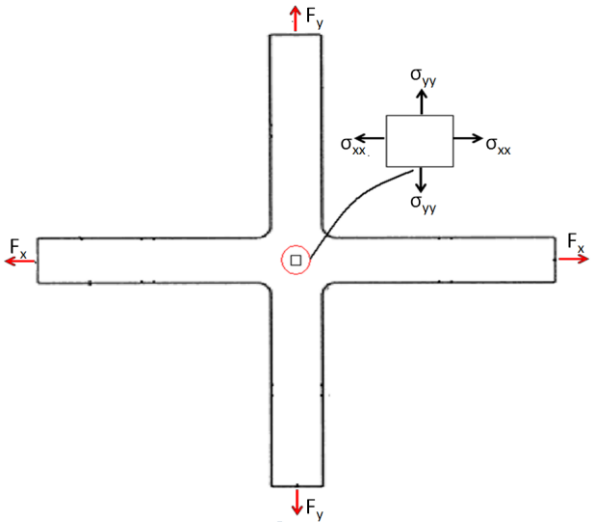

Figure 1-6: Stress state under biaxial loading

Smith and Pascoe's fatigue experiments [18] with cruciform specimens made from laminates of glass fiber woven roving reinforced polyester showed that both the extent and mode of damage were dependent on the biaxiality ratio. They reported that biaxiality ratio of 0.5 produced the highest fatigue strength whereas biaxiality ratios of 1 and higher reduced the fatigue strength of the composites. Furthermore, in both the cases, cracks appeared in the matrix along both the principal material directions which resulted in delamination, but biaxiality ratio of 0.5 had a suppressing effect on the growth of delamination. Negative biaxiality ratios led to low fatigue strengths and the failure mode was matrix shear deformation leading to severe delamination.

Even though cruciform specimens have been used by several researchers, the cruciform specimen tests have several limitations:

I. They do not allow the application of shear load.
II. Possibility of failure initiating at the corner fillet due to stress concentration. This topic has been researched upon by Smits et al. [19] using FEA and digital image correlation technique. The recommendations they make include the design of a cruciform specimen comprising of reduced thickness in the center.
III. The mechanism of conducting biaxial fatigue tests on cruciform specimens is very complex and expensive.

c) Tubular specimens

This test method employs thin tubular specimens and an apparatus which is capable of applying internal pressure, external pressure, axial load and torque, not only individually but also in combinations. Thus, testing of tubular specimens is capable of filling the entire failure envelope due to the fact that a variety of loading combinations can be incorporated in this test method.

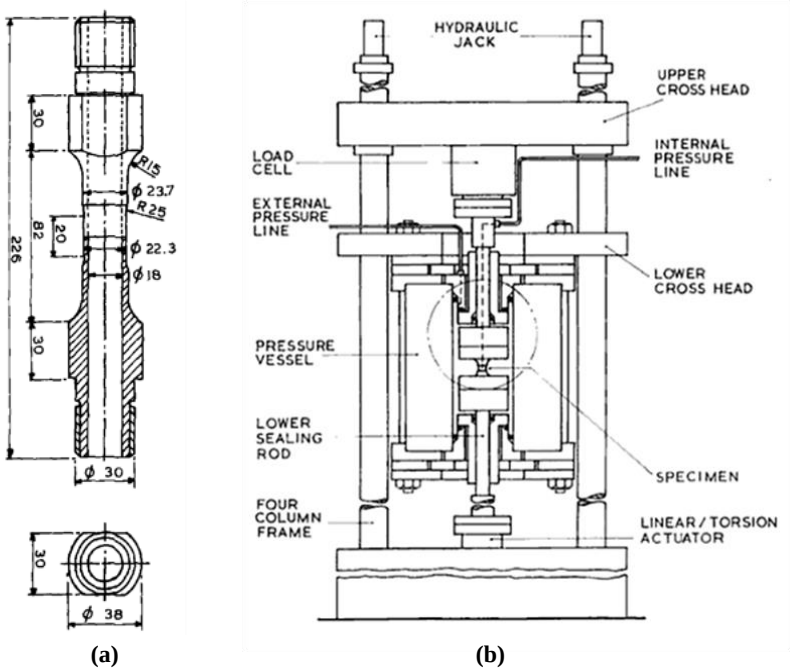

(a) **(b)**

Figure 1-7: (a) Tubular specimen (dimensions in mm) and (b) multiaxial test system [20]

Foral and Humphrey [21] conducted fatigue tests for a few limited number of cycles on AS4 carbon fiber and Kevlar 49 fiber reinforced epoxy composites and their hybrids at axial/hoop stress ratio = 0.5 on tubular specimens. They recorded a small increase in the stiffness in both principal material directions with increasing biaxial loads. They also found that tubular specimens could replicate the behavior of pressure vessels with high accuracy.

Francis et al. [22] by using notched carbon fiber reinforced epoxy tubes and Amijima et al. [23] by using un-notched woven glass fiber reinforced epoxy tubes have individually shown that the S-N curve for fiber reinforced composites actually shifts upwards when using a higher axial tension/torsion ratio. Francis et al. [24] also reported

that fatigue life of specimens loaded in biaxial tension/torsion fatigue decreased considerably when the stress range spanned the first ply failure (FPF) limit, as compared with loadings where the stress range was entirely within the FPF limit.

In their study on fatigue behavior of filament wound (±θ) glass fiber reinforced epoxy tubes, Qi and Cheng [25] have shown that the slopes of the S-N curves are influenced by the winding angles and biaxiality ratios. The fatigue strength of the composite depends on the stress ratio (R). The fatigue strength is higher at R = 0 and lower at R = -1.

The major drawback with this method is the fabrication of tubular specimens, which requires special processes such as filament winding and roll wrapping. Also it is important for the tubular specimens to be thin in the gage section in order to maintain stress/strain uniformity through thickness, which makes them extremely prone to buckling in torsion and compressive loading. If either internal or external pressure is used, a working fluid (mostly hydraulic oil) will be in direct contact with the specimen during the test, which may affect the material due to diffusion and/or chemical reaction. Also, there may be difficulty in conducting the test because of hydraulic connections, pressure fluctuation and the possibility of the leakage from the ends.

1.2.3 Biaxial Fatigue Data

In the recent past, Quaresimin et al. [26] have compiled data from the literature and presented a review of the same, which discusses the influence of factors like biaxiality ratios, off -axis and out-of-phase angles on the fatigue strength of fiber reinforced composites. They have suggested, while the out-of-phase angles do not have a huge impact on the fatigue strength of these composites, the biaxiality ratio λ_{12} (shown as λ_2 on figures. Also λ_1 on figures is λ_2 as per nomenclature used here) has an inverse effect on the fatigue strength of fiber reinforced composites. The data for the basic of this reporting is shown in the Figure 1-8 thru Figure 1-10.

The literature pertaining to multi-axial fatigue loading has indicated that the fatigue strength of composites is highly influenced by factors like lay-up of the lamina,

test specimen geometry, loading equipment, biaxiality ratios, etc. Hence it is worth developing newer test methodologies, damage prediction model or theory and most importantly test data which will allow engineering to use fiber reinforced composites to their highest potentials.

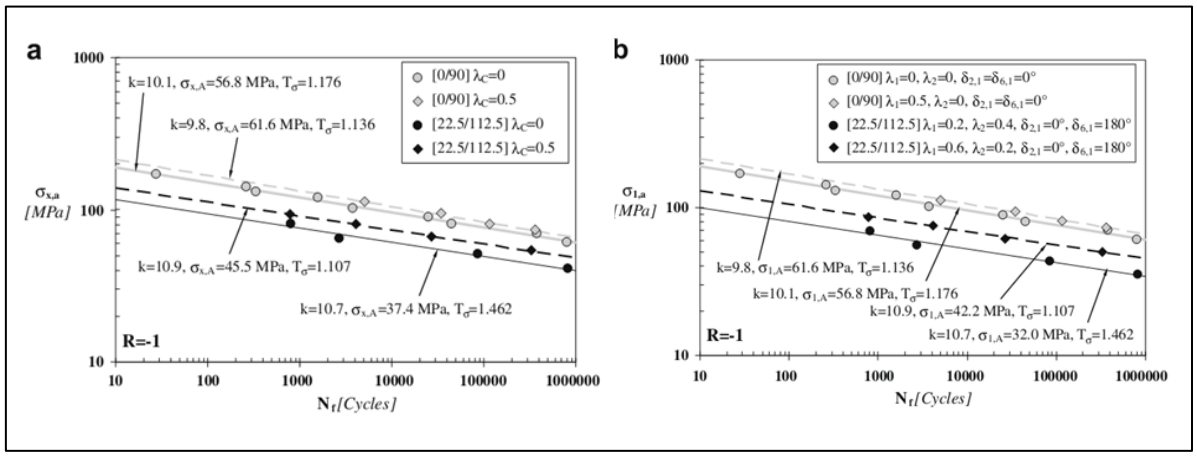

Figure 1-8: (a) Influence of off-axis angle and (b) biaxiality ratios on the fatigue strength of glass/polyester cruciform specimens subjected to combination of tension-tension [26]

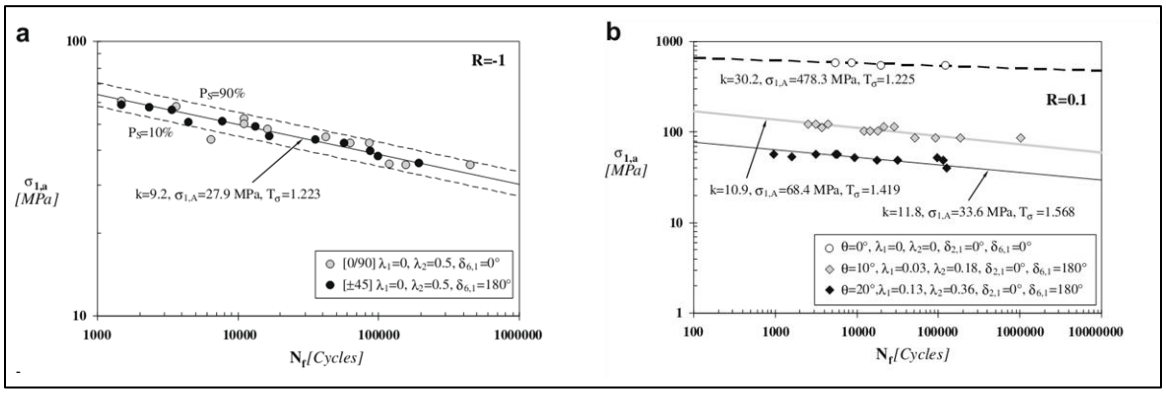

Figure 1-9: Influence of off-axis angles on the fatigue strength of (a) glass/polyester tubes subjected to in phase bending and torsion and (b) unidirectional epoxy/graphite specimens loaded in tension [26]

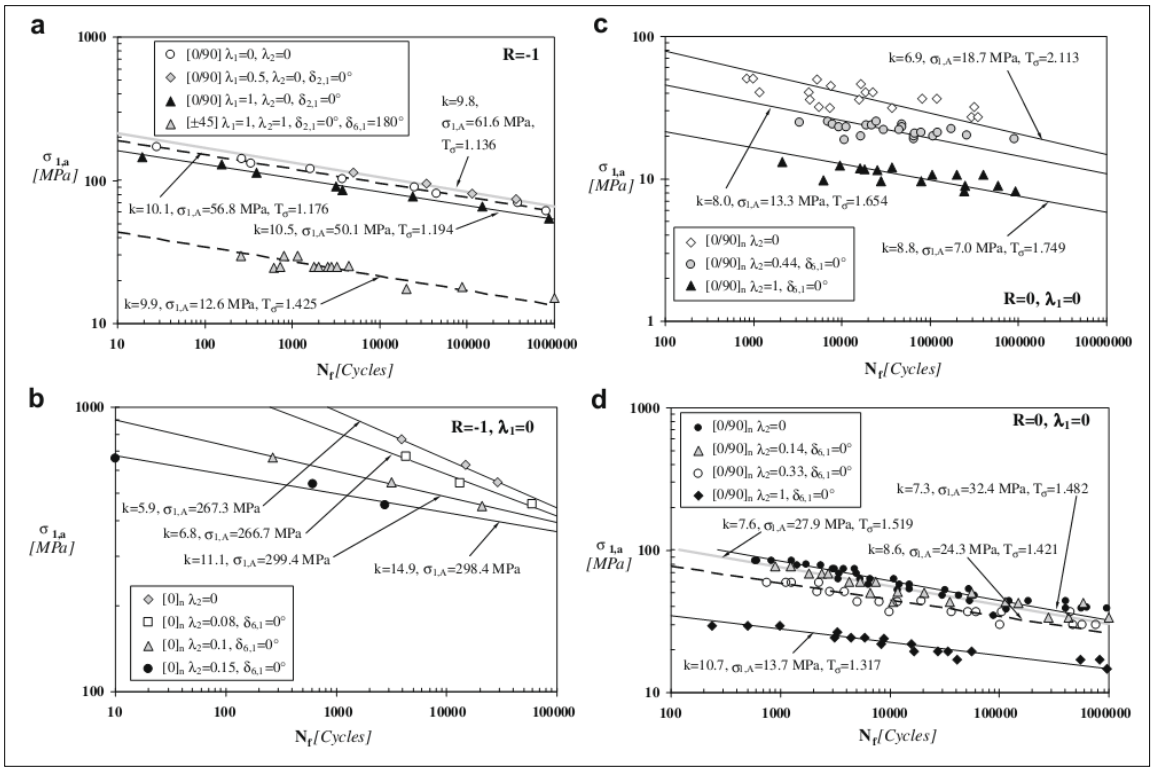

Figure 1-10: Influence of biaxiality ratio λ_{12} (shown as λ_2) on the fatigue strength of (a) glass/polyester cruciform specimens under tension-tension, (b) glass/epoxy bars under bending- torsion, (c) and (d) glass/polyester tubes under tension-torsion [26]

1.3 Fatigue Failure Theories

Several fatigue failure theories under biaxial stress conditions have been proposed in recent years. They are briefly introduced in this section.

1.3.1 Hashin and Rotem

Hashin and Rotem [27] introduced a fatigue failure criterion in early 1970's based on two principal damage modes that occur in fiber reinforced composites: fiber failure and matrix failure. For a unidirectional FRP lamina under uniaxial fatigue loading, the fiber orientation angle which divides these two modes is given by Equation 1.4.

$$\tan\theta_c = \frac{\tau^s}{\sigma_A^s}\frac{f_\tau(R,N,fr)}{f_A(R,N,fr)} \tag{1.4}$$

where, τ^s and σ^s_A are the static shear and longitudinal tensile strengths, respectively, and $f_\tau(R,N,fr)$ and $f_A(R,N,fr)$ are fatigue functions of the material along shear and axial directions. For θ less than θ_c, the failure mode is due to fiber failure, and for θ greater than θ_c, the fatigue failure is dominated by matrix failure. Since there are two types of failure modes associated with this criterion, there are two governing equations used for determining failure.

$$\sigma_A = \sigma_A^u \tag{1.5}$$

$$\left(\frac{\sigma_T}{\sigma_T^u}\right)^2 + \left(\frac{\tau}{\tau^u}\right)^2 = 1 \tag{1.6}$$

Equation 1.5 is used for predicting fatigue failure corresponding to the fiber failure mode, whereas Equation 1.6 is used for predicting fatigue failure based on matrix failure mode. In both the equations, the superscript 'u' symbolizes the fatigue failure stress and subscript 'T' indicates transverse to the fiber direction. This failure theory requires three experimentally determined S-N curves and the static strengths of the material for its application.

Also, it was shown that by using Equation 1.7, the fatigue function *f*'' can be calculated for any off-axis angle or the fatigue functions, f_τ and f_T can be calculated knowing the values of *f*'' at two different off-axis angles.

$$f''(R,N,fr) = f\tau \sqrt{\frac{1+\left(\frac{\tau^S}{\sigma_T^S}\right)^2 tan^2\theta}{1+\left(\frac{\tau^S f_\tau}{\sigma_T^S f_T}\right)^2 tan^2\theta}} \tag{1.7}$$

Hashin and Rotem [27] have evaluated their criterion for both uniaxial and biaxial data and have shown that this criterion can represent experimental data with relatively good accuracy.

1.3.2 Fawaz-Ellyin

Fawaz and Ellyin [28] proposed a biaxial fatigue failure criterion, which unlike the Hashin and Rotem's criterion requiring three S-N curves, needs only one reference S-N curve. Based on this reference or master S-N curve, this theory is able to predict the fatigue behavior of the material under any off-axis angle and biaxiality ratio.

Fawaz and Ellyin represented the reference S-N curve using a semi-log relation which is given by Equation (1.8).

$$S_r = m_r \log(N) + b_r \tag{1.8}$$

where, subscript '*r*' indicates reference, S_r is the cyclic stress, *N* is the number of cycles to failure at the applied stress, m_r and b_r are two material parameters which depend on the material properties and the loading conditions.

According to Fawaz and and Ellyin, the S-N curve for any off-axis and biaxiality ratio can be determined by Equation (1.9).

$$S(a_1, a_2, \theta, R, N) = f(a_1, a_2, \theta)[g(R)m_r \log(N) + b_r] \tag{1.9}$$

where, $a_1=\sigma_{yy}/\sigma_{xx}$, $a_2=\tau_{xy}/\sigma_{xx}$, *f* and *g* are non-dimensional functions, defined by

$$f(a_1, a_2, \theta) = \sigma_{xx}(a_1, a_2, \theta)/X_r \tag{1.10}$$

$$g(R) = \sigma_{max}(1 - R)/[\sigma_{(max)r} - \sigma_{(min)r}] \quad (1.11)$$

In Equations (1.10) and (1.11), $\sigma_{xx}(a_1, a_2, \theta)$ is the static strength along the x-direction under the loading parameters(a_1, a_2, θ), X_r is the static strength along the x-direction under reference loading conditions, and $[\sigma_{(max)r} - \sigma_{(min)r}]$ is the stress range applied to obtain the reference S-N curve.

In the same reference, Fawaz and Ellyin have applied their theory to both existing uniaxial and multi-axial experimental results and found good correlation.

1.3.3 Sims-Brogdon

Sims and Brogdon [29] developed a fatigue failure theory by extending the Tsai-Hill static failure theory. They replaced the static strengths with the corresponding fatigue functions so that the Tsai-Hill theory took the form:

$$\left(\frac{K_1}{\sigma_L}\right)^2 - \frac{K_1 K_2}{\sigma_L^2} + \left(\frac{K_2}{\sigma_T}\right)^2 + \left(\frac{K_{12}}{\sigma_S}\right)^2 = \frac{1}{\sigma_F^2} \quad (1.12)$$

where,

σ_F = laminate fatigue strength

σ_L = longitudinal fatigue strength

σ_T = transverse fatigue strength

σs = shear fatigue strength

K_1, K_2 and K_{12} are the ratios of the stresses along the principal material directions and the applied stresses.

From Equation 1.12, it is possible to determine the fatigue strength of a laminate, knowing the fatigue strengths along longitudinal, transverse and shear directions. Also, by knowing the stresses in each lamina, it is possible to determine the first-ply failure in fatigue.

Since this criterion is completely based on the Tsai-Hill theory, this criterion also does not consider the difference of material properties in tension and compression.

1.3.4 Failure Tensor Polynomial in Fatigue (FTPF)

Philippidis and Vassilopoulos [30] used the failure tensor polynomial developed by Tsai and Wu and extended it to fatigue by changing the static strengths to fatigue strength functions. This polynomial has the form:

$$F_{11}\sigma_1^2 + F_{22}\sigma_2^2 + 2F_{12}\sigma_1\sigma_2 + F_1\sigma_1 + F_2\sigma_2 + F_{66}\sigma_6^2 - 1 = 0 \quad (1.13)$$

with the components of the failure tensor polynomial are given by

$$F_{11} = \frac{1}{XX'}, F_{22} = \frac{1}{YY'}, F_{66} = \frac{1}{S^2}, F_1 = \frac{1}{X} - \frac{1}{X'}, F_2 = \frac{1}{Y} - \frac{1}{Y'}, F_{12} = -\frac{1}{2}\sqrt{F_{11}F_{22}} \quad (1.14)$$

where, *X*, *Y* and *S* are the fatigue strengths of the materials and functions of number of cycles to failure (N), stress ratio (R) and loading frequency (f). The superscript ' indicates the corresponding compressive strengths. Unlike the other failure theories, the application of this theory requires determination of five fatigue functions, which can be quite tedious and will need very extensive experimentation. Hence by assuming $X = X'$ and $Y = Y'$, the FTPF, given by Equation 1.13, takes the form:

$$\frac{\sigma_1^2}{X^2} + \frac{\sigma_2^2}{Y^2} - \frac{\sigma_1\sigma_2}{XY} + \frac{\sigma_6^2}{S^2} - 1 = 0 \quad (1.15)$$

This criterion can be used in the form of Equation 1.15 for any stress ratio, *R* and frequency, *f*, provided the basic S-N curves of the fatigue functions *X*, *Y* and *S* are known for the same *R* and *f* values.

1.4 Research Objective and Methodology

1.4.1 Research Objective

The objective of this research is to study the biaxial fatigue behavior of fiber reinforced polymer laminates under combined normal and shear loadings. Much of the previous biaxial fatigue research on flat laminates has been conducted using either off-axis specimens or cruciform specimens. As mentioned earlier, neither test can generate biaxial test condition in which shear loading can be combined with normal loading. In this research, a new biaxial fatigue test is developed using butterfly-shaped Arcan specimens to experimentally determine the faigue behavior of fiber reinforced polymer laminates under combined tensile and shear loadings. In addition, a biaxial fatigue failure prediction model is proposed.

1.4.2 Research Methodology

Biaxial fatigue behavior of fiber reinforced composites was studied, under pure tensile load, pure shear load, and combined tensile and shear loads using butterfly-shaped Arcan specimens. The butterfly shaped Arcan specimen is a modified form of Arcan specimen which was originally developed by Arcan et al. [31] to determine the shear properties of fiber reinforced composites. The versatility of the Arcan specimen is that it can be utilized for testing materials under uniaxial tensile loading, pure shear loading or a combination of in-plane normal and shear loadings. Unlike the other shear test methods, such as rail-shear test and picture-frame test, used for determining shear properties of fiber reinforced composite materials, it has a significant section with near-uniform shear stress distribution, which is small enough to induce failure. This test method was used by Arcan and Voloshin [32] to determine both axial and transverse shear moduli of Scotchply reinforced plastic type 1002. The authors mention that that prior to their experiments, transverse shear modulus was never experimentally determined to the best of their knowledge. They concluded that the tests show excellent agreement between the calculated longitudinal shear modulus and the measured one. Also, Arcan and Voloshin [33] used this specimen to generate a failure envelope for Scotchply reinforced plastic

type 1002 to demonstrate that this method could indeed be used to build failure envelopes for other materials including fiber reinforced composites.

The material used in this study is an E-glass fiber reinforced epoxy laminate with a laminate construction of $[0/90/0_{11}/90/0]$. The research is divided into four major tasks.

1) Develop butterfly-shaped Arcan specimens and test fixture using finite element analysis,
2) Conduct quasi-static test on the selected lmainate using the modified Arcan specimens to determine the static failure loads and failure modes in biaxial stress state,
3) Conduct biaxial fatigue tests using Arcan specimens to determine fatigue life at various biaxiality ratios,
4) Develop fatigue failure model under biaxial stress state.

1.5 References

[1] N. J. Pagano and J. C. Halpin, "Influence of end constraint in the testing of anisotropic bodies," *Journal of Composite Materials*, vol. 2, no. 1, pp. 18 -31, Jan. 1968.

[2] Y. Xiao, M. Kawai, and H. Hatta, "An integrated method for off-axis tension and compression testing of unidirectional composites," *Journal of Composite Materials*, vol. 45, no. 6, pp. 657-669, Oct. 2010.

[3] M. Kawai and N. Honda, "Off-axis fatigue behavior of a carbon/epoxy cross-ply laminate and predictions considering inelasticity and in situ strength of embedded plies," *International Journal of Fatigue*, vol. 30, no. 10-11, pp. 1743-1755, Oct. 2008.

[4] M. Kawai and K. Kato, "Effects of R-ratio on the off-axis fatigue behavior of unidirectional hybrid GFRP/Al laminates at room temperature," *International Journal of Fatigue*, vol. 28, no. 10, pp. 1226-1238, Oct. 2006.

[5] M. Kawai, S. Yajima, A. Hachinohe, and Y. Kawase, "High-temperature off-axis fatigue behaviour of unidirectional carbon-fibre-reinforced composites with different resin matrices," *Composites Science and Technology*, vol. 61, no. 9, pp. 1285-1302, Jul. 2001.

[6] G. Schneider, "Evaluation of lamina strength criteria by off-axis tensile coupon tests," *Fibre Science and Technology*, vol. 5, no. 1, pp. 29-35, Jan. 1972.

[7] J. H. Sinclair and C. C. Chamis, "Fracture modes in off-axis fiber composites," *Polymer Composites*, vol. 2, no. 1, pp. 45-52, Jan. 1981.

[8] P.-Y. Chang, J.-M. Yang, H. Seo, and H. T. Hahn, "Off-axis fatigue cracking behaviour in notched fibre metal laminates," *Fatigue & Fracture of Engineering Materials and Structures*, vol. 30, no. 12, pp. 1158-1171, Dec. 2007.

[9] M. Kawai and H. Suda, "Effects of non-negative mean stress on the off-axis fatigue behavior of unidirectional carbon/epoxy composites at room temperature," *Journal of Composite Materials*, vol. 38, no. 10, pp. 833-854, May 2004.

[10] A. Rotem and H. Nelson, "Fatigue behavior of graphite-epoxy laminates at elevated temperatures," in *Fatigue of Fibrous Composite Materials*, K. Lauraitis, Ed. ASTM STP723, pp. 152-173, 1981.

[11] A. P. Vassilopoulos and T. Keller, *Fatigue of Fiber-Reinforced Composites*. London: Springer, 2011.

[12] P. K. Mallick, *Fiber-Reinforced Composites: Materials, Manufacturing, and Design*, 3rd ed. Boca Raton FL: CRC Press, 2008.

[13] R. Jones, *Mechanics of composite materials*, 2nd ed. Philadelphia PA: Taylor & Francis, 1999.

[14] A. Plumtree, "A fatigue damage parameter for off-axis unidirectional fibre-reinforced composites," *International Journal of Fatigue*, vol. 21, no. 8, pp. 849-856, Sep. 1999.

[15] A. Varvani-Farahani, "A Fatigue Damage Parameter for Life Assessment of Off-axis Unidirectional GRP Composites," *Journal of Composite Materials*, vol. 40, no. 18, pp. 1659-1670, Jan. 2006.

[16] J. Radon and C. Wachnicki, "Biaxial Fatigue of Glass Fiber Reinforced Polyester Resin," in *Multiaxial Fatigue*, K. Miller and M. Brown, Eds. 100 Barr Harbor Drive, PO Box C700, West Conshohocken, PA 19428-2959: ASTM International, pp. 396-412.
[17] A. Makris, C. Ramault, D. Van Hemelrijck, D. Zarouchas, E. Lamkanfi, and W. Van Paepegem, "An investigation of the mechanical behavior of carbon epoxy cross ply cruciform specimens under biaxial loading," *Polymer Composites*, vol. 31, no. 9, pp. 1554-1561, Sep. 2010.
[18] E. W. Smith and K. J. Pascoe, "Biaxial fatigue of a glass–fibre reinforced composite. Part 1: Fatigue and fracture behaviour," in *Biaxial and Multiaxial Fatigue (EGF 3)*, M. W. Brown and K. J. Miller, Eds. London: Mechanical Engineering Publications, 1989, pp. 367-396.
[19] A. Smits, D. Van Hemelrijck, T. P. Philippidis, and A. Cardon, "Design of a cruciform specimen for biaxial testing of fibre reinforced composite laminates," *Composites Science and Technology*, vol. 66, no. 7-8, pp. 964-975, Jun. 2006.
[20] M. Found, U. Fernando, and K. Miller, "Requirements of a New Multiaxial Fatigue Testing Facility," in *Multiaxial Fatigue*, K. Miller and M. Brown, Eds. 100 Barr Harbor Drive, PO Box C700, West Conshohocken, PA 19428-2959: ASTM International, pp. 11-23.
[21] R. F. Foral and W. D. Humphrey, "Biaxial stress behavior of graphite and Kevlar 49 fiber/epoxy composites and hybrids," *AIAA Journal*, vol. 22, no. 1, pp. 111-116, 1984.
[22] P. H. Francis, D. E. Walrath, D. F. Sims, and D. N. Weed, "Biaxial Fatigue Loading of Notched Composites," *Journal of Composite Materials*, vol. 11, no. 4, pp. 488-501, Oct. 1977.
[23] S. Amijima, T. Fujii, and M. Hamaguchi, "Static and fatigue tests of a woven glass fabric composite under biaxial tension-torsion loading," *Composites*, vol. 22, no. 4, pp. 281-289, Jul. 1991.
[24] P. Francis, D. Walrath, and D. Weed, "First ply failure of G/E laminates under biaxial loadings," *Fibre Science and Technology*, vol. 12, no. 2, pp. 97-110, Mar. 1979.
[25] D. Qi and G. Cheng, "Fatigue behavior of filament-wound glass fiber reinforced epoxy composite tubes under tension/torsion biaxial loading," *Polymer Composites*, vol. 28, no. 1, pp. 116-123, Feb. 2007.
[26] M. Quaresimin, L. Susmel, and R. Talreja, "Fatigue behaviour and life assessment of composite laminates under multiaxial loadings," *International Journal of Fatigue*, vol. 32, no. 1, pp. 2 - 16, 2010.
[27] Z. Hashin and A. Rotem, "A Fatigue Failure Criterion for Fiber Reinforced Materials," *Journal of Composite Materials*, vol. 7, no. 4, pp. 448-464, Oct. 1973.
[28] Z. Fawaz and F. Ellyin, "Fatigue Failure Model for Fibre-Reinforced Materials under General Loading Conditions," *Journal of Composite Materials*, vol. 28, no. 15, pp. 1432-1451, Sep. 1994.
[29] D. Sims and V. Brogdon, "Fatigue Behavior of Composites Under Different Loading Modes," in *Fatigue of Filamentary Composite Materials*, K. Reifsnider and K. Lauraitis, Eds. 100 Barr Harbor Drive, PO Box C700, West Conshohocken, PA 19428-2959: ASTM International, pp. 185-205.

[30] T. P. Philippidis and A. P. Vassilopoulos, "Fatigue Strength Prediction under Multiaxial Stress," *Journal of Composite Materials*, vol. 33, no. 17, pp. 1578-1599, Sep. 1999.
[31] M. Arcan, Z. Hashin, and A. Voloshin, "A method to produce uniform plane-stress states with applications to fiber-reinforced materials," *Experimental Mechanics*, vol. 18, no. 4, pp. 141-146, Apr. 1978.
[32] A. Voloshin and M. Arcan, "Pure shear moduli of unidirectional fibre-reinforced materials (FRM)," *Fibre Science and Technology*, vol. 13, no. 2, pp. 125-134, Mar. 1980.
[33] A. Voloshin and M. Arcan, "Failure of unidirectional fiber-reinforced materials—New methodology and results," *Experimental Mechanics*, vol. 20, no. 8, pp. 280-284, Aug. 1980.

CHAPTER 2 : ANALYSIS AND DESIGN OF ARCAN SPECIMENS FOR BIAXIAL TESTING OF FIBER REINFORCED COMPOSITES

2.1 Introduction

Biaxial testing in this research was performed using the concept of Arcan specimen, which was developed by Arcan et al. [1] for determining material properties under pure shear and plane stress conditions. The original Arcan specimen is a plane circular disc with axisymmetric cutouts that formed two opposing notches at the center of the specimen. The area between the notches is called the significant section. The loading on the specimen can be applied either in line or at an angle with the significant section, the former producing a state of pure shear and the latter a combination of normal and shear stresses. Arcan et al. [1] utilized this specimen to determine the shear moduli of an aluminum alloy and a unidirectional glass/epoxy composite. Noting that the original specimen was difficult to machine, Arcan and his co-workers [1]–[3] developed a butterfly shaped specimen which was adhesively bonded to the front surfaces of a circular aluminum loading plates split along the significant section. Even though the specimen was off-centered from the loading plane, Arcan and Voloshin [2] found good agreement between the measured shear modulus and the theoretical value.

Hung and Leichti [4] used finite element method to analyze the stress states in butterfly-shaped Arcan specimens made of a unidirectional carbon fiber reinforced composite under shear and biaxial loadings. The specimen was assumed to be bonded to the circular steel loading plates split along the significant section and the load was applied to the steel plates using a pinned joint. Two different fiber orientations were considered: 1-2 with fibers on the top and bottom plies oriented normal to the significant section and 2-1 with fibers on the top and bottom plies oriented parallel to the significant

section. For each fiber orientation, three different notch angles, namely 90^o, 110^o and 134^o, were examined. From the standpoint of uniformity of shear stresses in the significant section under shear loading, the best notch angles were 134^o for the 1-2 fiber orientation and 90^o for the 2-1 fiber orientation. For 2-1 fiber orientation and 90^o notch angle, five different notch radii (from 0 to 7.19 mm) were considered. Based on the degree of uniformity of normal stresses along and across the significant section, a notch radius of 2.38 mm was recommended for both shear and biaxial loadings.

In another study, Hung and Leichti [5] used Moire interferometry to determine the shear strain distributions in the Arcan specimen configuration used in Ref. [4]. In this study, the notch radius was 2.4 mm and the notch angle was 90^o. It was observed that under shear loading, the shear strain distribution was nearly uniform across much of the significant section for both 1-2 and 2-1 fiber orientations; however, for the 1-2 orientation, the shear strain was higher than the nominal shear strain and showed a peak near each notch tip. For the 2-1 specimens, shear strain was never higher than the nominal strain, and instead of showing a peak, it smoothly dropped to zero at the notch tip. These results are similar to the stress distributions determined by finite element analysis in Ref. [4].

The general design of the Arcan specimen and the biaxial test configuration used in the current research is shown in Figure 2-1. The specimen has a butterfly shape with two opposing notches at its mid-length. It is mounted on a loading fixture which consists of a top half and a bottom half, each half consisting of a front clamping plate and a back clamping plate. The Arcan specimen is mounted between the front and the back clamping plates of each of the two halves of loading fixture using steel bolts and nuts. A series of circular holes near the outer circumference of the clamping plates allows loading of the specimen in tension, shear, and combined tension and shear modes (Figure 2-2). The loading fixture is connected to a loading yoke at each end using either three pins so that its rotation is constrained at the ends (fully clamped condition) or one pin so that it is able to rotate about the pin as the load is applied on the yokes (unclamped condition). The loading on the fixture can be either tensile or compressive. Since the specimen is centrally located between the front and back clamping plates, the loading is along the mid-plane of the specimen thickness.

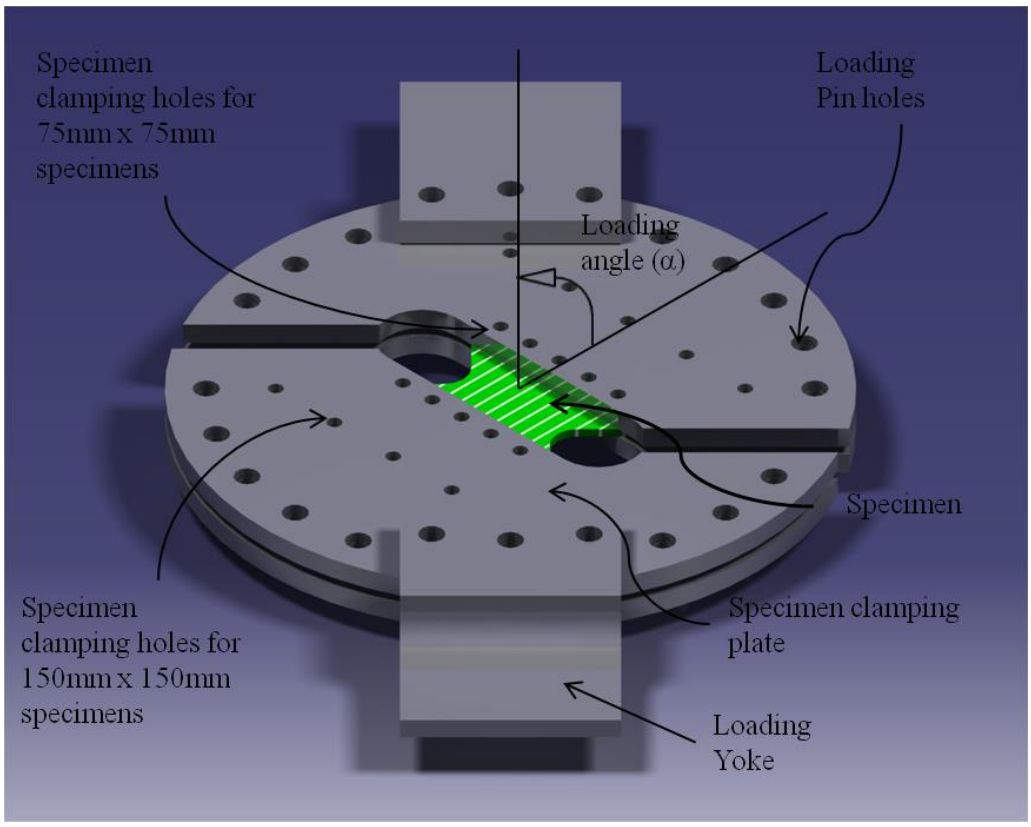

Figure 2-1: A butterfly-shaped Arcan specimen mounted in the loading fixture (α is the loading angle).

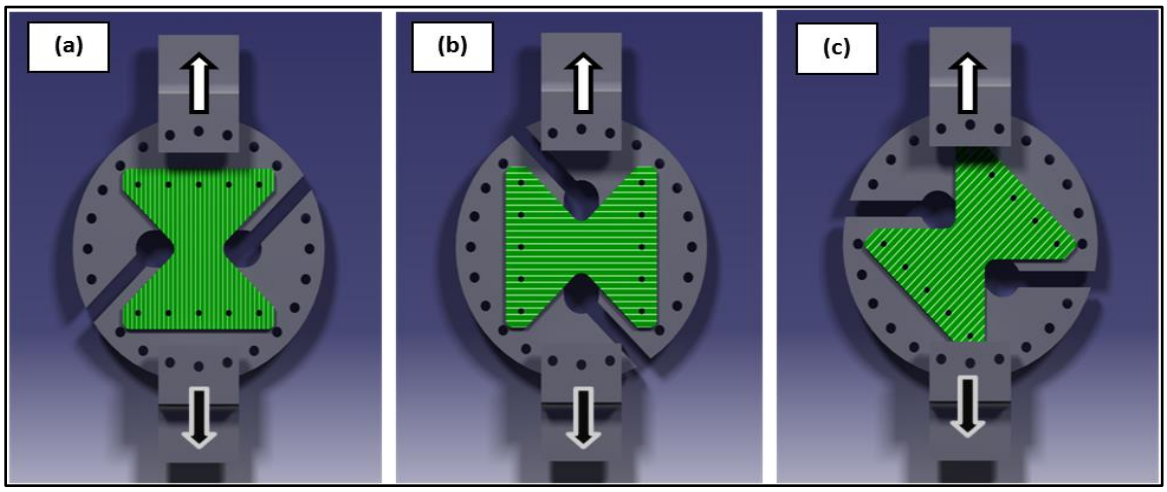

Figure 2-2: Butterfly-shaped Arcan specimens under (a) axial (α = 0°), (b) shear (α = 90°) and (c) combined loading (0° < α < 90°) (For clarity, the front plates are not shown.)

Several aspects of the design of the Arcan specimens and the loading fixture are addressed in this chapter. Among them are (1) the notch radius, (2) the notch angle, (3) the specimen size, (4) effect of clamping type, (5) effect of specimen material, and (6) effect of fixture material. The analysis was performed using finite element method primarily under shear loading; however, other loading conditions were also investigated. The notch radius of a butter-fly shaped Arcan specimen is optimized using finite element analysis with a goal to develop an optimum shape of the specimen that produces uniform stresses and strains along the significant area when subjected to a range of external biaxial loads. Using finite element analysis, the notch radius is optimized under a loading configuration that primarily produces shear stresses along the significant section. Furthermore, finite element analysis is used to determine the effects of specimen fixture stiffness, clamping conditions and notch angle on the reaction loads and stress distributions.

The effect of clamping condition was studied in this chapter since as Mohr and Doyoyo [6] have observed that a fully clamped condition introduces horizontal reaction loads at the clamped fixture ends, which will influence the mean normal and shear stresses in the significant section. However, in this analysis, Mohr and Doyoyo did not take into account the effect of the loading fixture on the horizontal reaction loads. Using a simple frame model, Greer et al. [7] have shown that the magnitude of the horizontal reaction load relative to the applied load depends on both the loading angle and the stiffness ratio of the Arcan specimen and the loading actuator. Since the horizontal reaction load is a side thrust on the loading mechanism, it may cause damage to the loading frame if it is too large. In the current research, a detailed finite element analysis is performed to examine the effect of loading fixture stiffness on the horizontal reaction loads and stresses in the significant section of the Arcan specimen used.

2.2 Specimen, Loading Fixture and Materials

2.2.1 Specimens

Two different specimen geometries were considered: (1) large Arcan specimen with dimensions 75 mm x 75 mm x 3.3 mm (thickness) and (2) small Arcan specimen with dimensions 50 mm x 75 mm x 3.3 mm (thickness). Both specimens contain opposing notches and the notch angle is 90^o (Figure 2-3). The specimens are mounted on the loading fixture using 6-mm diameter bolt holes drilled at each end of the specimen. For the large specimen there are five bolt holes and for the small specimens there are three bolt holes at each end.

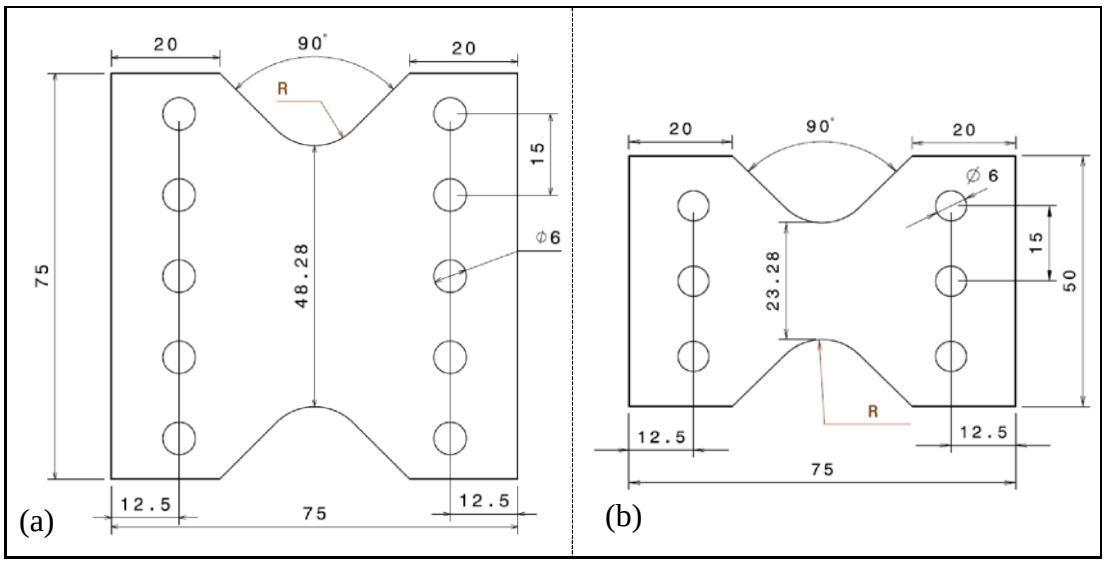

Figure 2-3: Dimensions of a) large and b) small Arcan specimen (thickness = 3.3 mm).

The widths of the large and small Arcan specimens are 75 and 50 mm, respectively. Because of the difference in width, the significant length between the two notches is also different. For example, if the notch radius at the corner of the 90° notch angle is 10 mm, the distance between the notch ends for the large specimen is 48.28 mm; thus the cross-sectional area of the specimen between the notch tips, considered the significant section, is 159.32 mm^2. For the same notch radius, the distance between the notches in the small specimen is 23.28 mm and the cross sectional area of the significant section of this small Arcan specimen is 76.82 mm^2.

2.2.2 Loading Fixture

The geometry of the loading fixture is shown in Figure 2-2. Both front and back plates of the fixture are 9 mm thick and the loading holes are 15° apart. To investigate the effect of the loading fixture, three different fixture materials were considered in the finite element models: steel with a modulus of 210 GPa, aluminum alloy with a modulus of 69 GPa and magnesium alloy with a modulus of 45 GPa. Because of the modulus differences, the steel fixture has the highest stiffness and the magnesium fixture has the lowest stiffness.

2.2.3 Specimen Materials

The principal material of the Arcan specimens used in this study is a E-glass fiber/ epoxy (GFE) laminate composed of 15 layers and has a stacking sequence described by $[0/90/0_5/\overline{0}]_S$, where 0° plies are oriented along the specimen length and 90° plies are oriented along the specimen width. The other specimen materials considered in the finite element analyses (FEA) are carbon-fiber/epoxy (CFE), boron-fiber/epoxy (BFE) and SMC R-25, which is a planar isotropic composite containing randomly oriented 25-mm long E-glass fibers in a polyester matrix. The laminate construction in both CFE and BFE specimens is the same in the GFE specimen. The elastic properties of the specimen materials are listed in Table 2-1. The purpose for considering four different specimen materials is to examine the effect of their modulus on the stress distributions and horizontal reaction loads. As can be observed in Table 2-1, boron-fiber/epoxy has the highest modulus in the fiber direction, which is followed by carbon-fiber/epoxy, E-glass fiber/epoxy and SMC-R25, in that order.

Table 2-1: Materials and properties used for Arcan specimen.

Material	**Density (g/cm^3)**	**E_{11} (GPa)**	**E_{22} (GPa)**	**Major Poisson's ratio**	**In-plane shear modulus, G_{12} (GPa)**
Boron/Epoxy (BFE)	1.99	207.00	19.00	0.21	6.40
AS-Carbon/Epoxy (CFE)	1.54	127.00	9.00	0.25	5.70
E-Glass/Epoxy (GFE)	1.80	39.00	4.80	0.30	4.80
SMC-R25	1.83	13.20	13.20[A]	0.25	5.28[B]
A - Same as E_{11}, since isotropic.					
B – Value calculated by the FE solver					

2.3 Finite Element Model

Finite element analysis (FEA) was performed using Altair HyperWorks as pre and post processor and MSC Nastran/Abaqus (FE solver) to determine the stress distributions in the significant section, horizontal reaction load in the case of clamped fixture and rotation of the fixture in the case of unclamped fixture. Both Arcan specimen and loading fixture were modelled using a combination of 3-noded and 4-noded shell elements. However, the area in the close proximity of the significant section was modeled only using 4-noded shell elements. The elements used in the loading fixture had a 9 mm thick shell section with three through-the-thickness integration points, whereas the elements used in the Arcan specimen were a 15-layer composite shell with 15 through-the-thickness integration points. Fully constrained rigid body elements (RBE2 in Nastran) were used to connect the Arcan specimen with the loading fixture at the bolt holes.

FE analysis of the large Arcan specimen was performed with both 1-2 and 2-1 specimens, first to determine the effect of notch radius on the stress distribution along the significant length and then to understand the effects of specimen material and fixture material. FE analysis of the small Arcan specimen was performed with 1-2 specimens to understand the effects of specimen material, specimen notch radius, specimen notch angle as well as the fixture material.

2.3.1 FE Model of the Large Arcan Specimen

The first FE model of the large Arcan specimen, shown in Figure 2-4, was created without the fixture and the bolt holes at the specimen ends; instead the shear loads were applied directly at the specimen ends. The notch angle was 90^{o}. The notch radius was varied from 0 to 16 mm in steps of 2 mm to determine the variation of shear stress along the significant length between the notch tips. Since the area of the significant section changes with notch radius, the applied load was varied so that it produced an average shear stress of 83 MPa for all of the significant sections. Table 2-2 lists the area of the

significant section and the applied shear load value for each notch radius. The optimum notch radius was determined on the basis of the degree of uniformity of shear stress distribution in the significant section. All subsequent FE models of large Arcan specimens included the fixture and tensile loads were applied on the loading yokes mounting holes of the fixture.

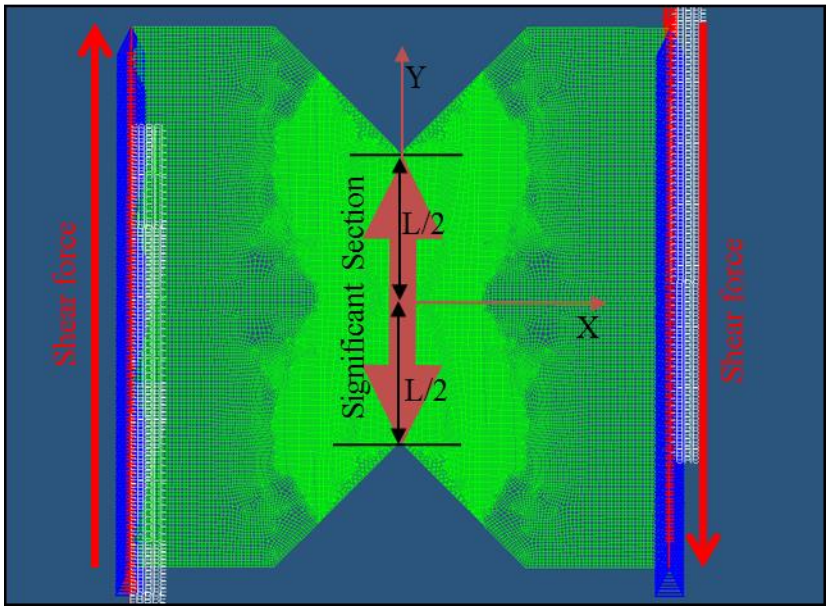

Figure 2-4: FE model used for determining the notch radius effect in shear loading applied at the specimen ends.

Table 2-2: Shear loads applied at the ends of the large Arcan specimen with 90° notch angle

Notch Radius (mm)	Area of the Significant Section (mm^2)	Shear Load at the Specimen Ends (N)	Average Shear Stress in the Significant Section (MPa)
0	132	10,956.00	83
2	137.46	11,409.18	83
4	142.94	11,864.02	83
6	148.40	12,317.20	83
8	153.87	12,771.21	83
10	159.34	13,225.22	83
12	164.81	13,679.23	83
14	170.27	14,132.41	83
16	175.74	14,586.42	83

An example of the FE model used for determining the stress distributions in the large Arcan specimen mounted on the loading fixture is shown in Figure 2-5. In this model, the specimen was clamped to the fixture at its two ends using rigid body elements. A load of 1 kN was applied in the downward y-direction at the lower end of the fixture. The upper end of the fixture was assumed to be fixed (fully constrained condition) so that $u_x = u_y = 0$ and $\theta_z = 0$. The lower end was assumed to have only a translational degree of freedom in the loading direction so that only $u_x = 0$ and $\theta_z = 0$. Similar modelling techniques were also used for the FE analyses of the small Arcan specimen.

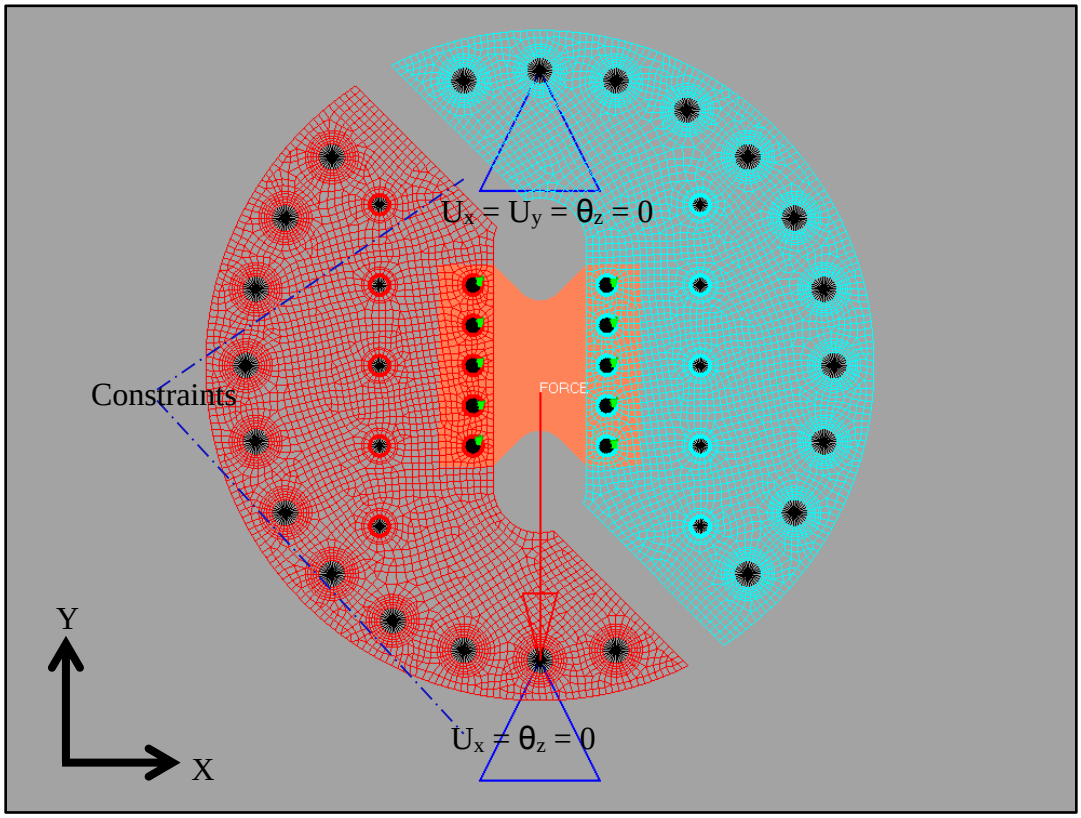

Figure 2-5: Finite element model for the large Arcan specimen and the loading fixture.

2.3.2 FE Model of the Small Arcan Specimen

Preliminary FEA was conducted to examine the variation of the stress components in a shear loaded small Arcan specimen with different values of notch angle. The notch radius was maintained constant at 10 mm and the FE model was created without the fixture and the bolt holes at the specimen ends; instead the shear loads were applied directly at the specimen ends. Four different notch configurations were considered.

1) Notch radius = 10 mm and notch angle = 90° (significant section area = 76.84 mm^2)
2) Notch radius = 10 mm and notch angle = 120° (significant section area = 108.52 mm^2)
3) Notch radius = 10 mm and notch angle = 134° (significant section area = 121.67 mm^2)
4) Notch radius = 10 mm, notch angle = 120° (significant section area = 76.84 mm^2, which is the same as in Configuration 1).

In the first three configurations, as the notch angle was increased, the significant section area also increased. In the fourth configuration, the notch radius and notch angle were the same as in Configuration 2, but the shoulder length of the specimen was reduced to 11.68 mm to maintain the same significant section area as in Configuration 1 (Figure 2-6). Thus, Configurations 1 and 4 have the same notch radius and significant section area, but they have different notch angles.

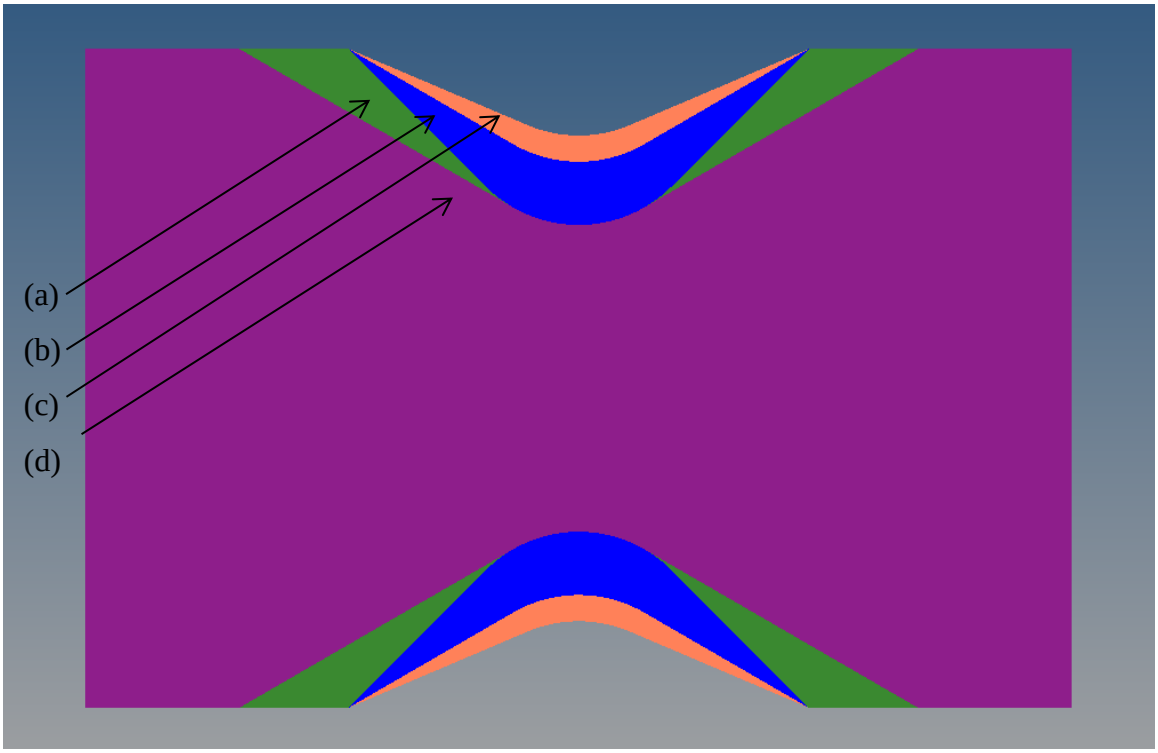

Figure 2-6: Small Arcan specimens with various notch angles, notch radius and shoulder length: (a) Notch radius = 10 mm and notch angle = 90°, (b) Notch radius = 10 mm and notch angle = 120°, (c) Notch radius = 10 mm and notch angle = 134° and (d) Notch radius = 10 mm, notch angle = 120° and cross sectional area same as in (a).

2.3.3 Effect of Fixture Stiffness

As shown in Figure 2-7, the Arcan fixture will experience a horizontal reaction force (side thrust) and a moment reaction at both ends when tested under the fully clamped boundary conditions. The horizontal reaction force is eliminated when the fixture is unclamped; however, the unclamped boundary condition causes rotation of the Arcan fixture about the loading pins. For the unclamped boundary condition, $u_x = u_y = 0$ at the top end and only $u_x = 0$ at the bottom end. This section of the study was conducted to determine the influence of the fixture boundary conditions on the reaction loads and fixture rotations.

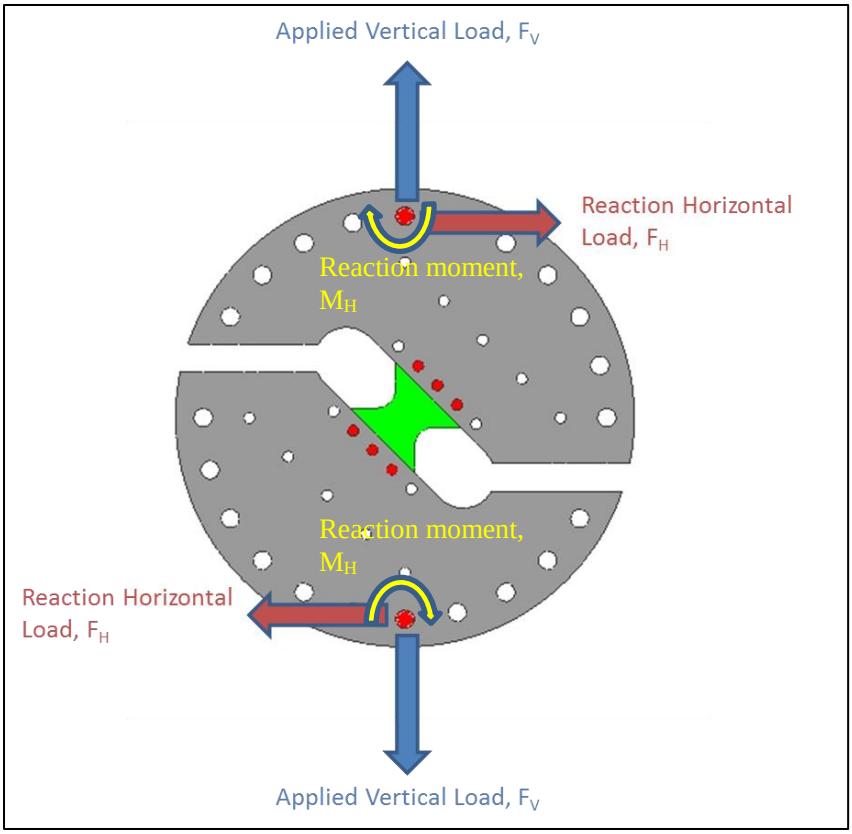

Figure 2-7: Reaction loads at the ends of a clamped ARCAN fixture

For the FEA conducted in this section, a load of 500 N was applied at each of the two lower halves of the Arcan fixture at the loading pin so that the total load was 1 kN. The boundary conditions for the clamped and unclamped configurations were created by constraining and allowing in-plane rotation of the Arcan fixture about the loading pin, respectively.

2.3.4 Effect of Fiber Orientation Angle

To understand the influence of the fiber orientation angle on the stress distribution in the significant section of the small Arcan specimen, FE analysis was conducted where the fiber orientation angle, θ was varied from 0° to 90°. The specimen material was GFE. Fiber orientation of 0° indicates that fibers on the top/bottom surfaces are aligned along the specimen length and fiber orientation of 90° indicates that fibers on the top/bottom surfaces are aligned along the specimen width. The other fiber orientation

angles indicate the angle between the specimen length direction and the fibers on the top/bottom surfaces.

2.4 Results

2.4.1 Large Arcan Specimen

a) Effect of Notch Radius in 1-2 Specimens with Shear Loads Applied at the Ends

The shear stress distribution in the significant section of the large 1-2 E-glass fiber/epoxy (GFE) Arcan specimen in response to the shear mode of loading can be seen in Figure 2-8. The shear force P was applied directly at the specimen ends. Because of symmetry, the shear stress τ_{xy} is plotted only for one-half of the significant section. The stress values are normalized with respect to the average shear stress ($\tau_{avg}=P/A_{s,}$ where P is the applied shear force at each end and A_s is the area of the significant section). It can be seen in Figure 2-8 that the notch radii below 8 mm first cause an increase in shear stress and then a decrease as the notch tip is approached. On the other hand, notch radii higher than 12 mm cause the shear stress to decrease over a larger distance ahead of the notch tip. With 8 mm and 10 mm notch radii, the shear stress also decreases as the notch tip is approached, but the shear stress remains more uniform over a larger portion of the significant section. Among these two notch radii, the specimen with 10 mm notch radius has a higher uniformity of shear stress distribution when compared with the specimen with 8 mm notch radius. The shear stress at the center of the significant section is within 3% of the average shear stress for 10 mm notch radius (Table 2-3). Hence, the optimum notch radius for the 1-2 specimens is considered to be 10 mm.

Table 2-3: Ratio of shear stress at the center of the significant section and average shear stress

Notch Radius (mm)	Ratio of Center τ_{xy} and τ_{avg}. in 1-2 Specimens	Ratio of Center τ_{xy} and τ_{avg}. in 2-1 Specimens
0	0.903	1.028
2	0.936	1.068
4	0.964	1.103
6	0.989	1.134
8	1.01	1.16
10	1.03	1.182
12	1.05	1.202
14	1.06	1.220
16	1.08	1.236

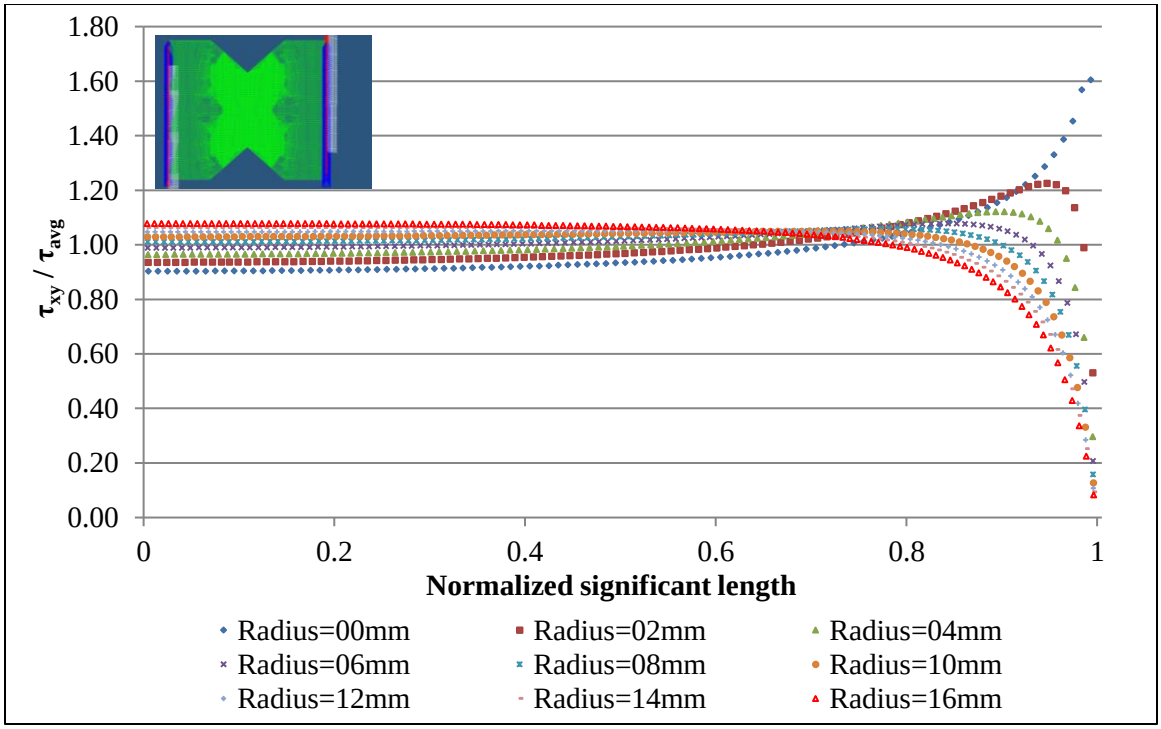

Figure 2-8: Shear stress distribution in the significant section of large 1-2 Arcan specimen with different notch tip radii. Notch angle = 90°.

b) Effect of Notch Radius in 2-1 Specimens with Shear Loads Applied at the Ends

The shear stress distribution in the significant section of the large 2-1 GFE Arcan specimen in response to the shear mode of loading can be seen in Figure 2-9. The shear force P was applied directly at the specimen ends. Because of symmetry, the shear stress τ_{xy} for the 2-1 specimens is plotted only for one-half of the significant section. It can be seen in Figure 2-9 that for all notch radii, the shear stress in the 2-1 specimens decreases as the notch tip is approached. Furthermore, unlike the 1-2 specimens, uniformity in the shear stress distribution in the 2-1 specimens decreases as the notch radii increases and a zero notch radius produces the best stress uniformity. The shear stress at the center of the significant section is closest to the average shear stress for the zero notch radius (Table 2-3). However, from a practical approach, zero notch radius is highly undesirable due to its characteristic to produce an extremely high stress concentration factor when the applied load creates normal stresses in the significant section.

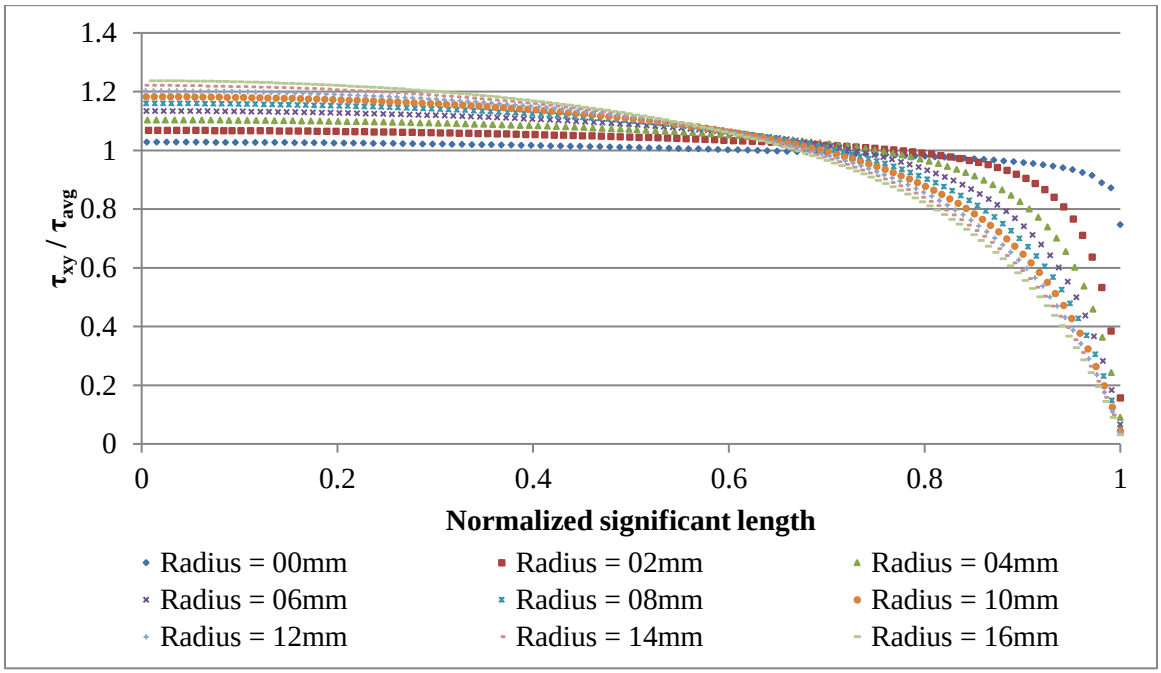

Figure 2-9: Shear stress distribution in the significant section of large 2-1 Arcan specimen with different notch tip radii. Notch Angle = 90°.

c) Stress Distributions in the Significant Section of Large 1-2 Specimens with Load Applied at the Fixture Ends

Figure 2-10, Figure 2-11 and Figure 2-12 show the stress distributions in the significant section of the large GFE Arcan specimen modelled with the fixture for axial loading (α = 0°), combined tensile and shear loadings (α = 45º) and shear loading (α = 90°). The notch radius and notch angle are 10 mm and 90º, respectively. The specimen was clamped to the fixture at both ends and a vertical load of 1 kN was applied at the bottom end of the fixture.

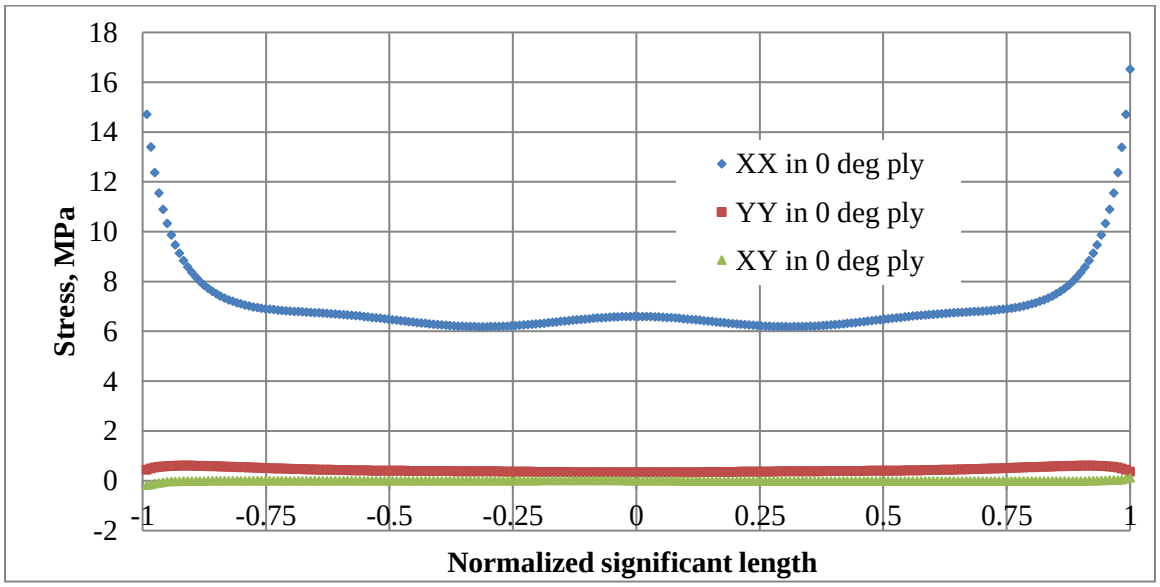

Figure 2-10: Stress distributions along the significant section of large 1-2 specimen when axially loaded (α = 0°)

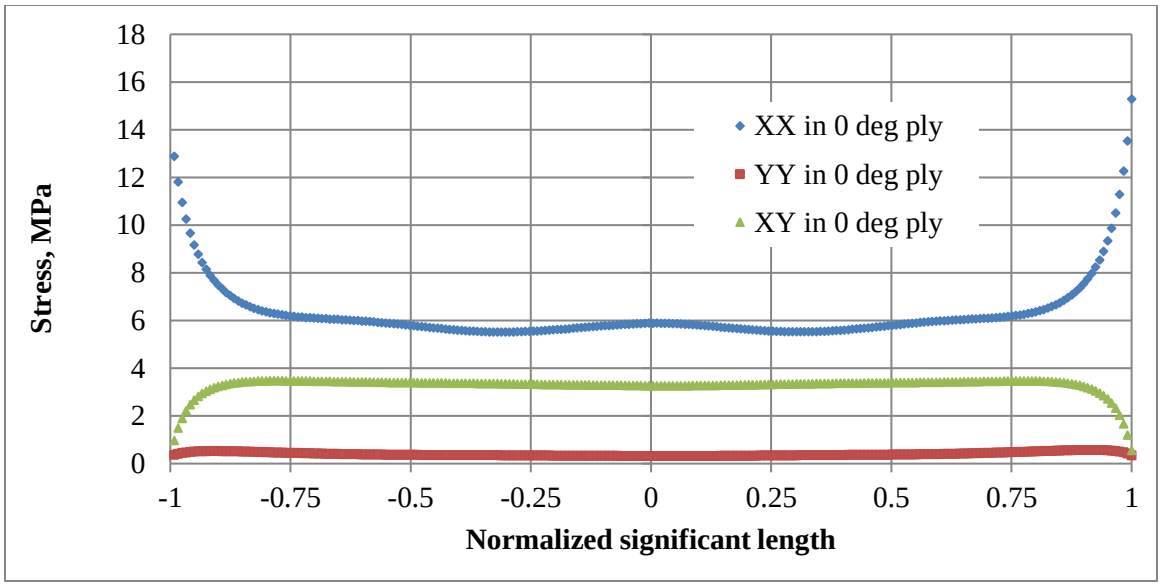

Figure 2-11: Stress distributions along the significant section of large 1-2 specimen when loaded under combined axial and shear loads ($\alpha = 45°$)

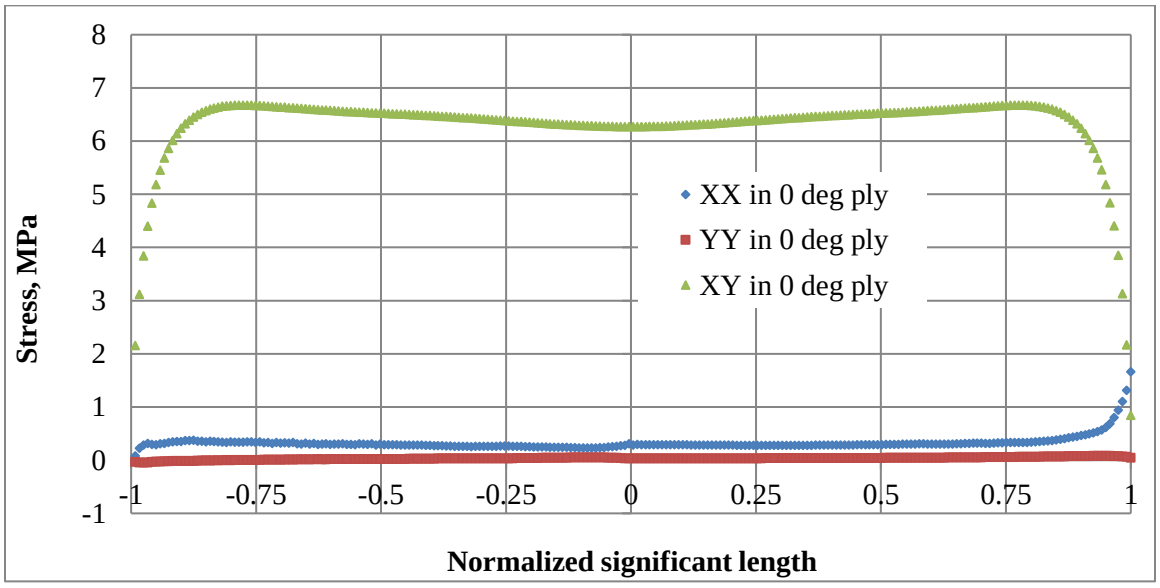

Figure 2-12: Stress distribution along the significant length of large 1-2 specimen when loaded in shear ($\alpha = 90°$).

The following observations can be made from Figure 2-10 - Figure 2-12 about the stress distributions in the significant section.

1) For axial tensile loading, i.e., $\alpha = 0°$ (Figure 2-10), σ_{xx} is the major stress component, $\tau_{xy} = 0$ and there is a small σ_{yy}. σ_{xx} is uniform over 80% of the

significant section, but increases rapidly to very high values as the notch tip is approached.

2) For combined tensile and shear loading, i.e., $\alpha = 45°$ (Figure 2-11), both σ_{xx} and τ_{xy} have significant values, and there is a small σ_{yy}. In this case, both σ_{xx} and τ_{xy} are uniform over 80% of the significant section. σ_{xx} increases and τ_{xy} decreases as the notch tip is approached.
3) For shear loading, i.e., $\alpha = 90°$ (Figure 2-12), τ_{xy} is the major stress component, $\sigma_{yy} = 0$ and there is a small σ_{xx}. τ_{xy} is uniform over 80% of the significant section, but decreases rapidly as the notch tip is approached.

Figure 2-13 shows a comparison of the shear stress distributions in the significant section of the large Arcan specimen with and without the loading fixture. In both cases, the specimen was loaded in shear. It can be seen in this figure that the two shear stress distributions match very closely, which validates the initial modeling without the fixture (Figure 2-4) to determine the optimum notch radius.

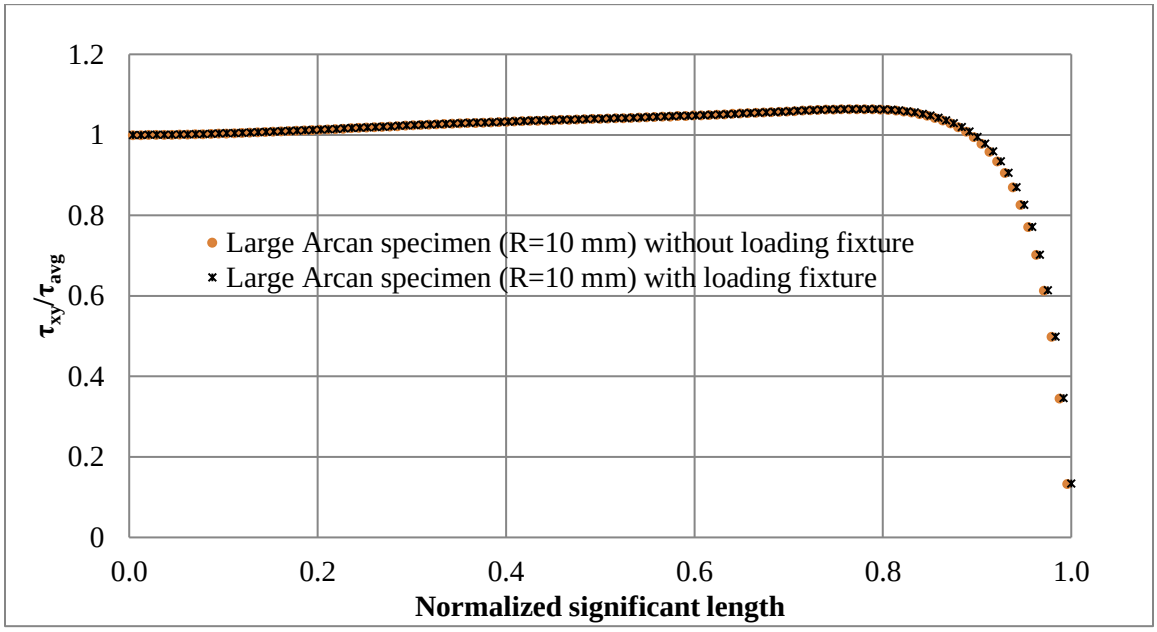

Figure 2-13: Stress distribution comparison obtained in shear loaded large 1-2 Arcan specimens ($\alpha = 90°$).

2.4.2 Small Arcan Specimen

Loads on all small 1-2 Arcan specimens were applied at the fixture ends. The downward load in all cases was 1 kN and the material was GFE. The effects of notch radius, notch angle and clamping on the stress distributions were studied. In the first two studies, the loading angle α was 90^o so that the specimen was loaded in shear. The effect of clamping was investigated in the last study.

a. Effect of Notch Radius

FE analysis on shear-loaded small GFE Arcan specimen was performed to understand the influence of the notch radius on the stress distributions in the significant section. The notch radii used for this study were 6, 8, 10 and 12 mm. The maximum shear stress predicted in specimen with these different notch radius is shown in Table 2-4. The results from these FE analyses are shown in Figure 2-14. It is seen that a notch radius of 10 mm produced the best stress uniformity compared to the other three notch radii. This observation about the stress uniformity is the same as that for the large Arcan specimen.

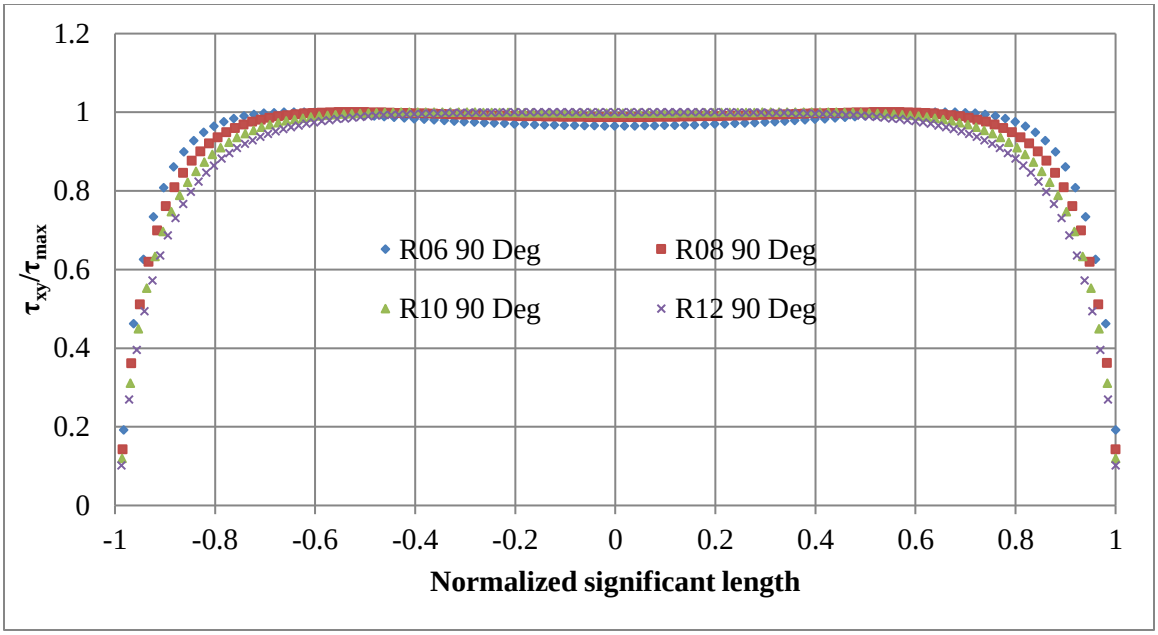

Figure 2-14: Stress distribution in shear loaded small 1-2 Arcan specimens with different notch radii.

Table 2-4: Maximum shear stress in small 1-2 Arcan specimens with different notch radii and cross sectional areas

Notch Radius, mm	**Notch Angle, Degrees**	**Cross-sectional area, mm^2**	**Shear Load, N**	**Maximum Shear Stress (τ_{max}), MPa**	**Average Shear Stress ($\tau_{avg.}$), MPa**	**% Difference**
6	90	65.87	1000	16.24	15.18	6.98
8	90	71.38	1000	15.06	14.01	7.49
10	90	76.82	1000	14.13	13.02	8.52
12	90	82.30	1000	13.38	12.15	10.12

Table 2-4 lists the maximum and average shear stresses in the significant section of the small 1-2 Arcan specimens subjected to shear loading. Both maximum shear and average shear stresses decrease with increasing notch radius, but the difference between them increases with increasing notch radius.

b. Effect of Notch Angle

The shear stress distributions in the significant section of shear-loaded small Arcan specimen with different notch angles are shown in Figure 2-15 and the maximum shear stress values are listed in Table 2-5. It can be seen that the 90° notch angle produces the best results in terms of the shear stress uniformity in the significant section. The extent of stress uniformity as well as the maximum shear stress decrease with increasing notch angle. A comparison of two 120° notch angled specimens with different significant section area (Figure 2-16) shows that as long as the notch angle and notch radius remain the same, varying significant section does not have any significant effect on the ratio of τ_{xy} and τ_{max}.

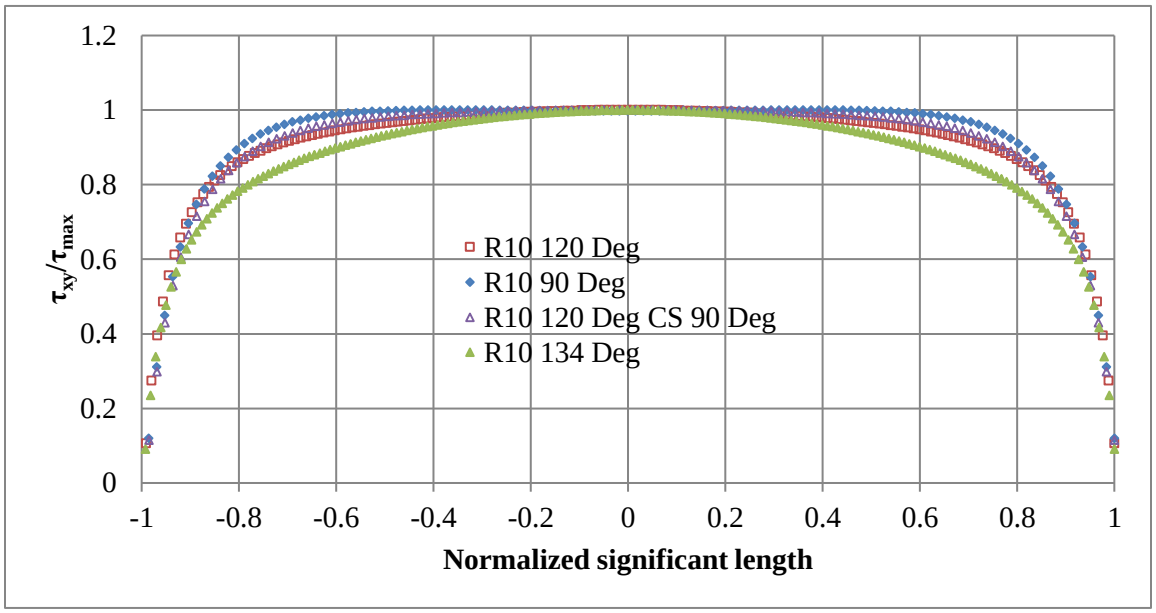

Figure 2-15: Stress distribution in shear loaded small 1-2 Arcan specimen of varying notch angles ($\alpha = 90°$).

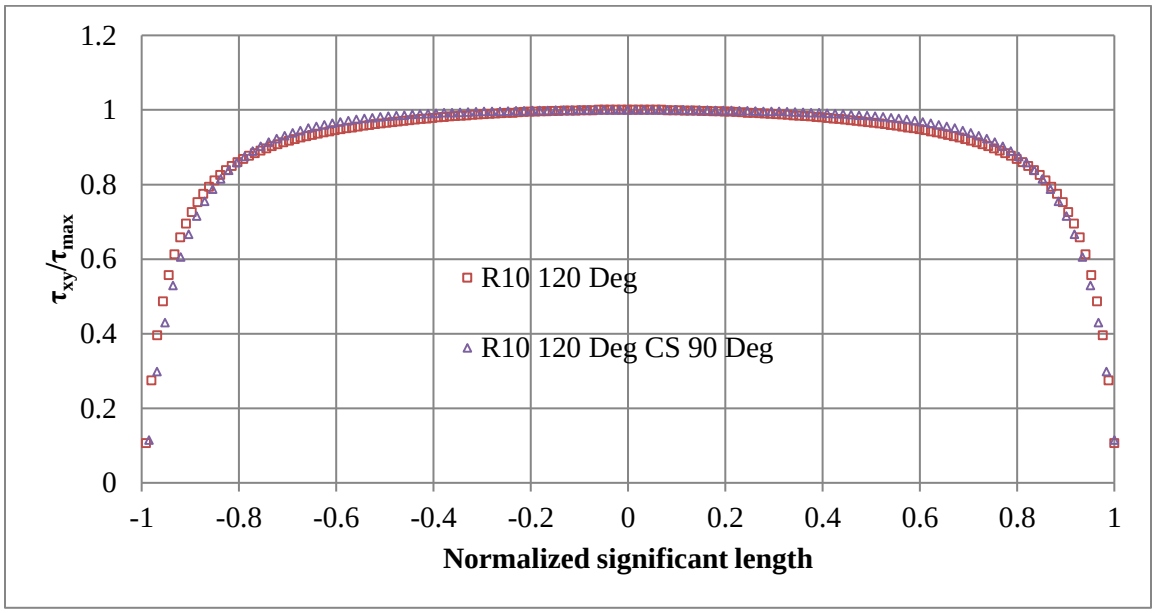

Figure 2-16: Stress distribution in 120 ° notch angle shear loaded small 1-2 Arcan specimens with 10 mm notch tip radius, but different cross sectional areas.

Table 2-5: Maximum shear stress in small 1-2 Arcan specimens with different notch angles and cross sectional areas

Notch Radius, mm	**Notch Angle, Degrees**	**Cross-sectional area, mm^2**	**Shear Load, N**	**Maximum Shear Stress (τ_{max}), MPa**
10	90	76.82	1000	14.13
10	120	108.50	1000	10.21
10	134	121.65	1000	9.46
10	120	76.82	1000	14.36

c. Effect of Specimen Size

A comparison of the shear stress distributions in the significant sections of the small and large Arcan specimens with notch radius of 10 mm and notch angle 90^o is shown in Figure 2-17. The shear stress distribution in the small Arcan specimen is uniform over 60% of the significant section. On the other hand, the shear stress distribution in the large Arcan specimen is uniform only over 10% of the significant section.

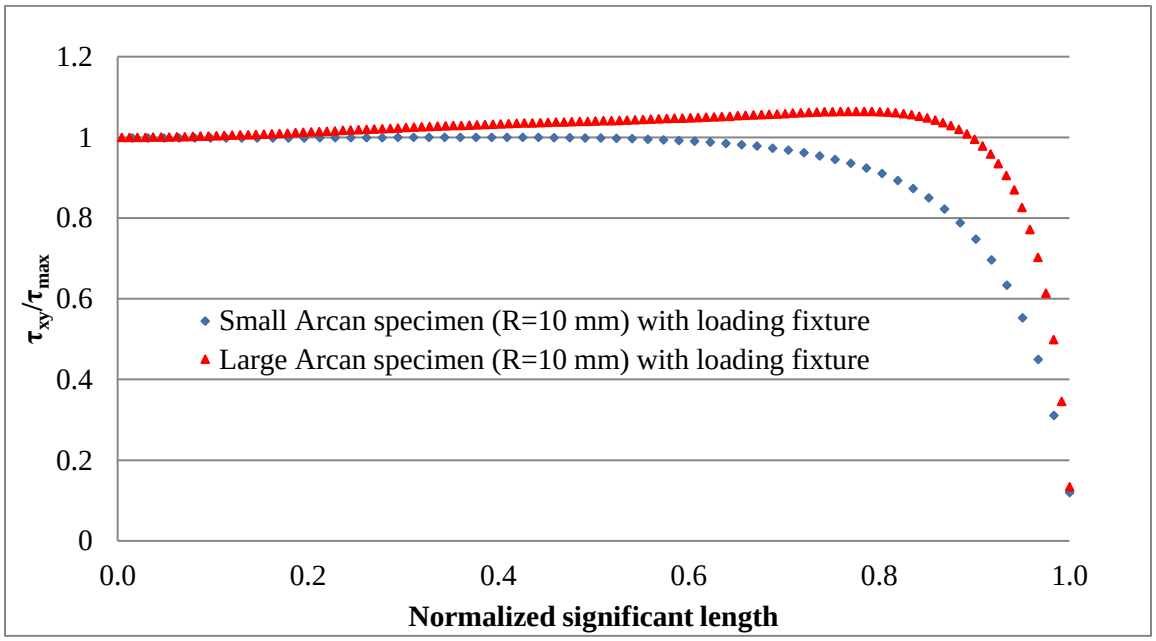

Figure 2-17: Comparison of stress distribution obtained in shear loaded small and large Arcan specimens ($\alpha = 90°$).

d. Effect of Clamping

Since the reaction forces generated in the clamped Arcan specimen will influence the stress distributions in the significant length, it is important to compare the stress distributions obtained in the significant sections of the clamped and unclamped Arcan specimens. Small GFE Arcan specimen with 10 mm notch radius and 90° notch angle was considered and the load applied in each case was 1 kN. The loading angles were 0°, 30°, 45°, 60° and 90°. Figure 2-18-Figure 2-22 show the results of this study.

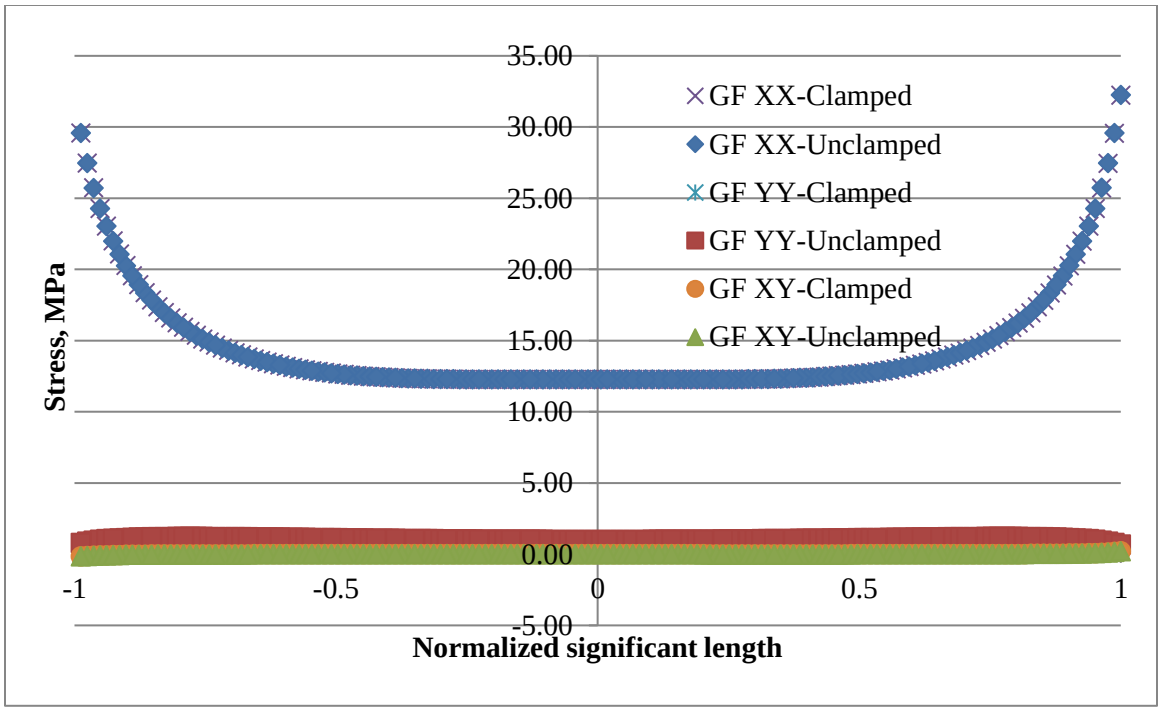

Figure 2-18: Comparison of the stress distributions obtained in small GFE Arcan specimens under clamped and unclamped conditions at 0° loading angle.

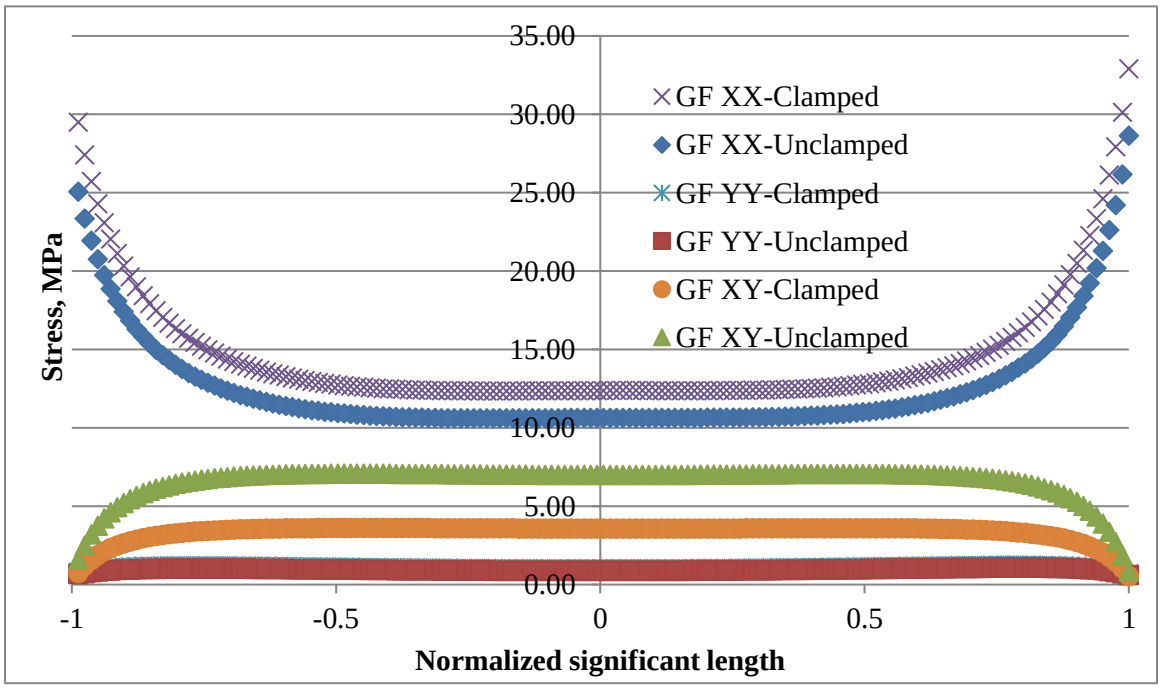

Figure 2-19: Comparison of the stress distributions obtained in small GFE Arcan specimens under clamped and unclamped conditions at 30° loading angle.

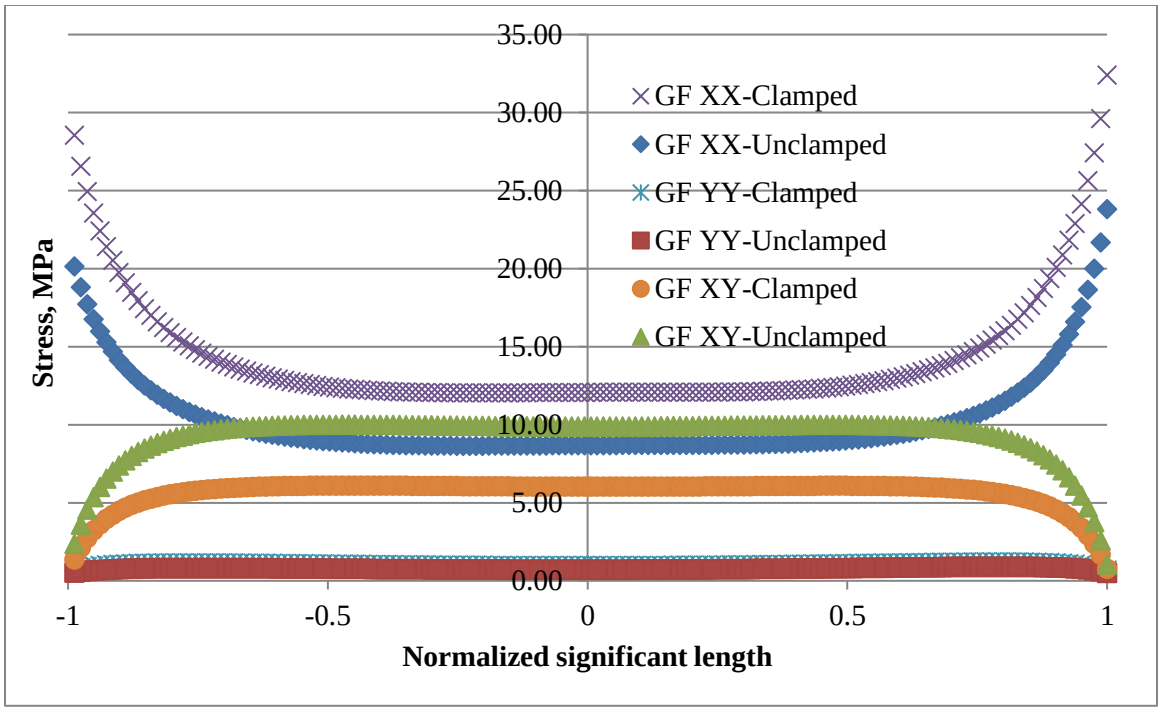

Figure 2-20: Comparison of the stress distributions obtained in small GFE Arcan specimens under clamped and unclamped conditions at 45° loading angle.

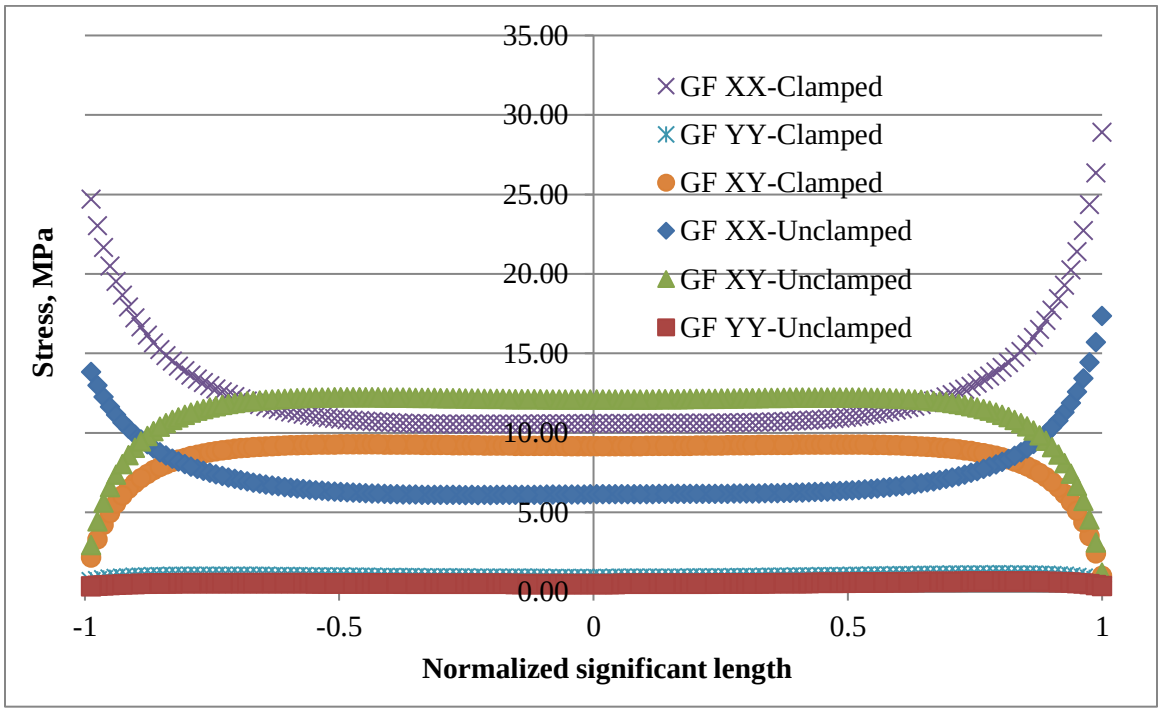

Figure 2-21: Comparison of the stress distributions obtained in small GFE Arcan specimens under clamped and unclamped conditions at 60° loading angle.

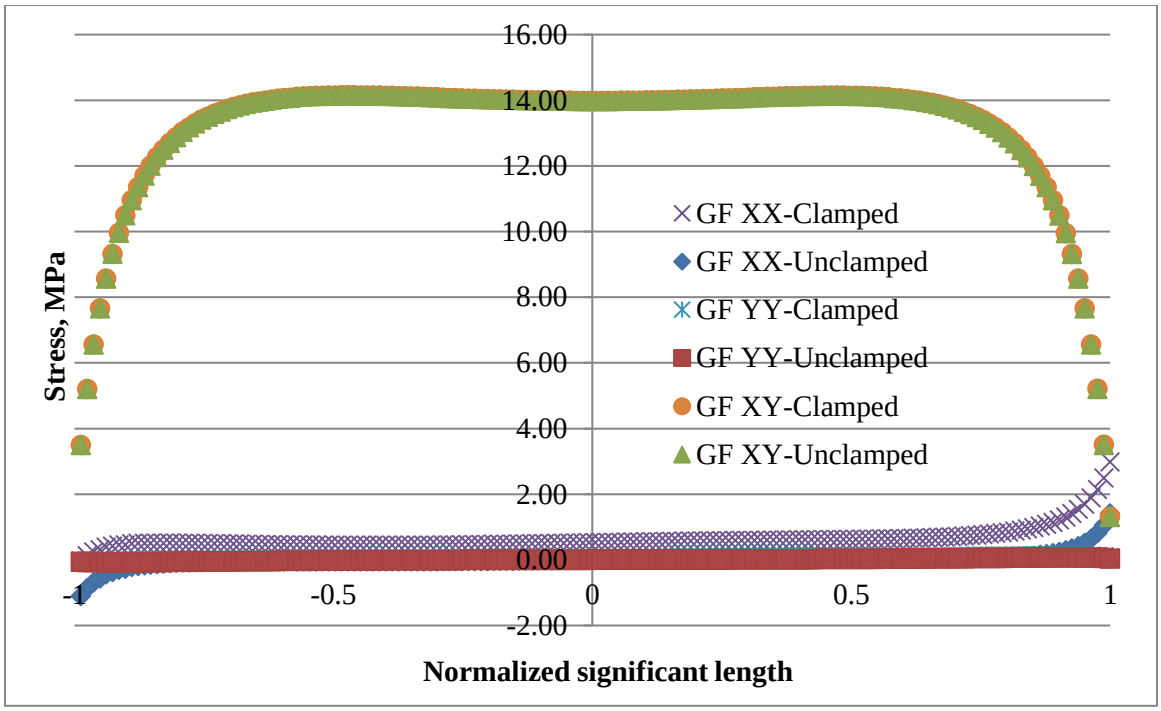

Figure 2-22: Comparison of the stress distributions obtained in small GFE Arcan specimens under clamped and unclamped conditions at 90° loading angle.

Figure 2-18 shows that clamped specimens produce the same stress distributions as the unclamped specimens for the 0^o loading angle. At 0^o loading angle, the significant section experiences uniaxial tension. At 90^o loading angle, the significant section experiences pure shear, and in this case, there is no difference in the shear stress distributions, but the normal stress component σ_{yy} is slightly higher in the clamped specimens. At loading angles other than 0° and 90°, the combined tension and shear stresses exist in the significant section. For these loading angles, the following observations are made from Figure 2-19 -Figure 2-21.

1. The axial stress component, σ_{xx} , in the clamped specimen is always higher than in the unclamped specimen.
2. The shear stress component, τ_{xy} , in the clamped specimen is always lower than in the unclamped specimen.
3. The transverse stress component, σ_{yy}, are similar in both the clamped and unclamped specimens.

e. Effect of Laminate Material

Figure 2-23 - Figure 2-25 show the stress distributions in the significant section of small 1-2 GFE, CFE and BFE Arcan specimens loaded at 0°, 45° and 90° angle. The material lay-up in all three specimens was $[0/90/0_5/\overline{0}]_S$, where 0° plies are oriented along the specimen length and 90° plies are oriented along the specimen width. The notch angle was 90° and the notch radius was 10 mm. From these figures, it is seen that the stress distribution along the significant section of the specimen depends on the laminate material. The uniformity of stress distribution decreases as the primary modulus of the laminate material increases. The BFE specimen shows the least uniformity of stress distribution along the significant section and the GFE specimen shows the highest uniformity of stress distribution.

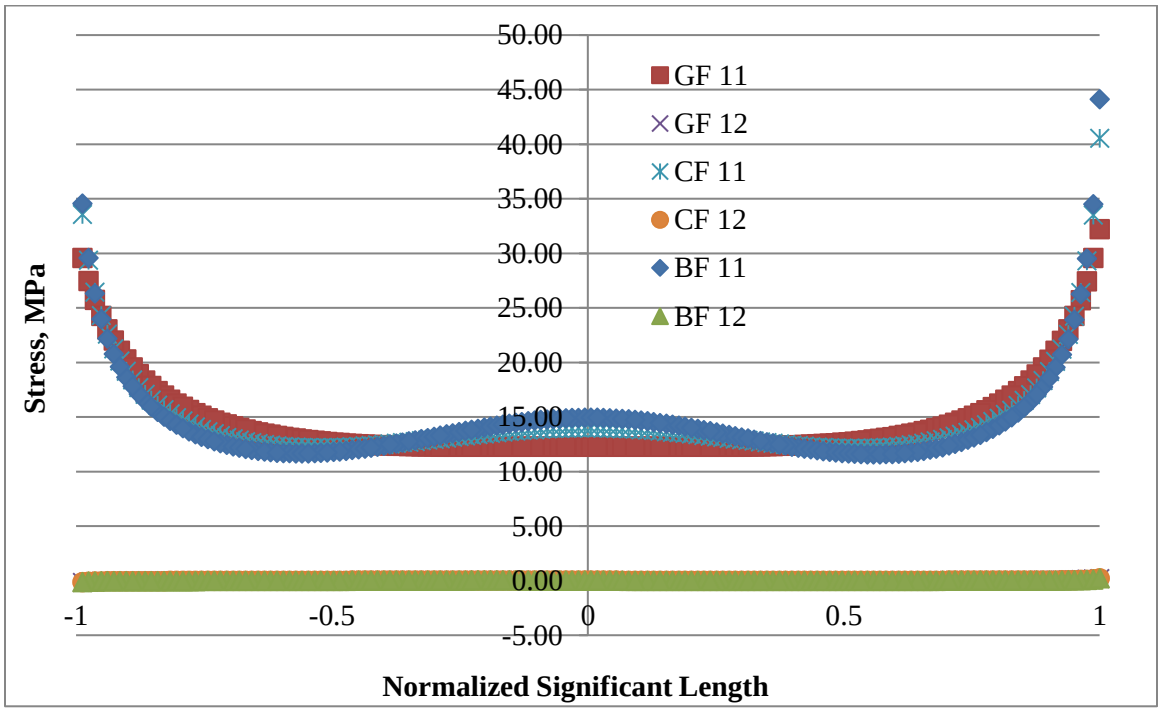

Figure 2-23: Comparison of the stress distributions obtained in small GFE, CFE and BFE 1-2 Arcan specimens with clamped boundary conditions and at 0° loading angle.

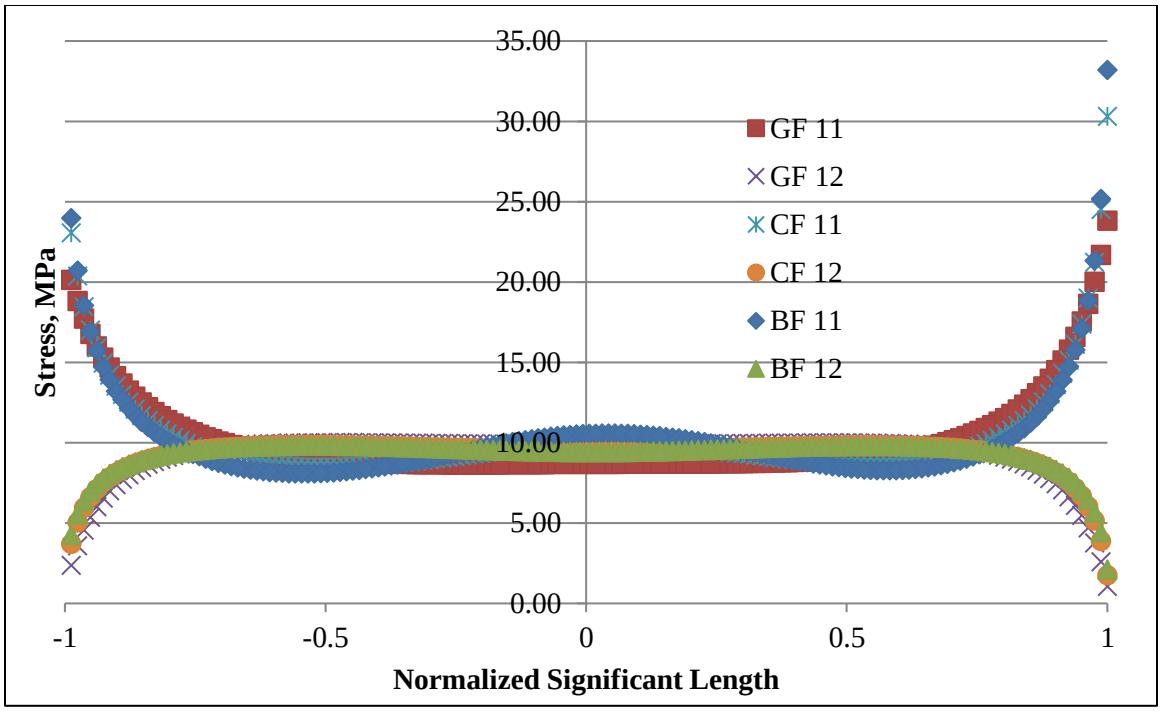

Figure 2-24: Comparison of the stress distributions obtained in small GFE, CFE and BFE 1-2 Arcan specimens with clamped boundary conditions and at 45° loading angle.

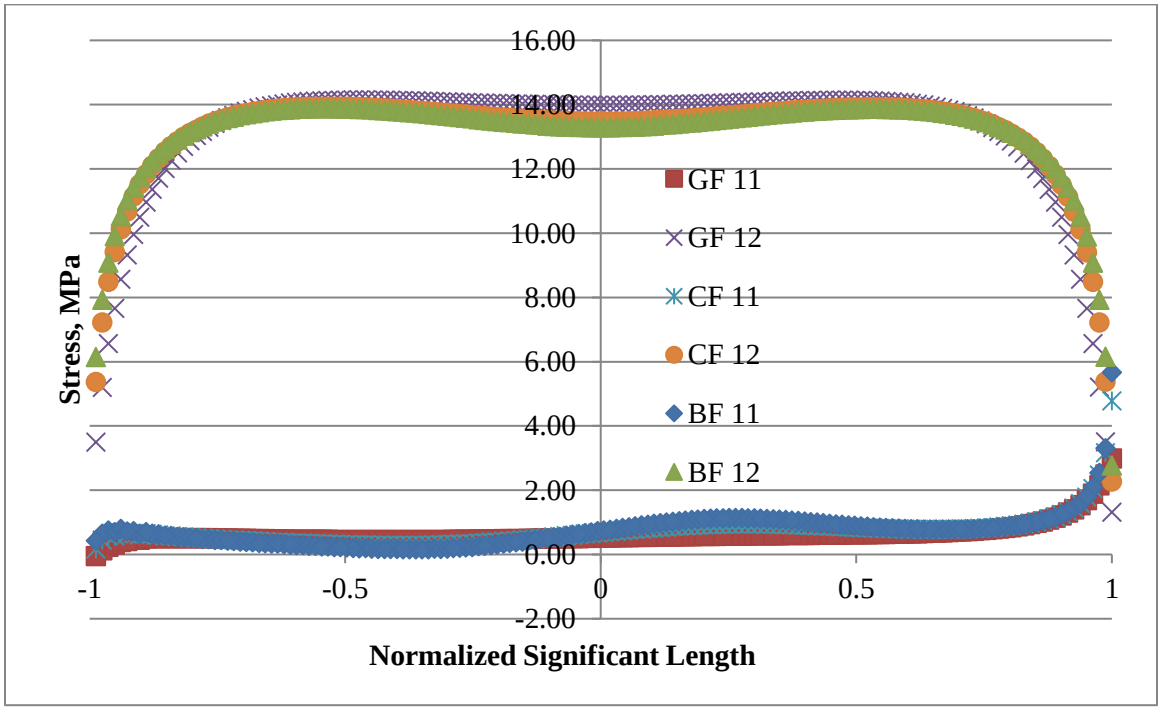

Figure 2-25: Comparison of the stress distributions obtained in small GFE, CFE and BFE 1-2 Arcan specimens with clamped boundary conditions and at 90° loading angle.

2.4.3 Horizontal Reaction Force and Rotation

a. Clamped Boundary Conditions

The ratio of the horizontal reaction force generated at the fixture ends of the clamped large 1-2 Arcan specimens and the applied load is plotted in Figure 2-26. The following observations are made from this figure.

(a) Except for 0 and 90^o loading angles, the horizontal reaction force is significantly higher with the steel fixture than with the aluminum fixture. The geometry and thickness were the same for both steel and aluminum fixtures. However, since the modulus of steel is nearly three times higher than that of aluminum, the steel fixture has a higher stiffness than the aluminum fixture. Thus, it can be concluded that the horizontal reaction force increases with increasing fixture stiffness.

(b) The horizontal reaction force depends on the modulus of the Arcan specimen material. Except for 0 and 90^o loading angles, the horizontal reaction force is the lowest for BFE and the highest for GFE. At 0^o loading angle, there is no horizontal reaction force. At 90^o loading angle, the difference in horizontal reaction forces is relatively small.

(c) The horizontal reaction force is a function of the loading angle. At 0^o loading angle, the horizontal reaction force is zero. As the loading angle is increased, the horizontal reaction force first increases, and after reaching the highest value between 45 and 60^o loading angles, it decreases with increasing loading angle.

In another series of analysis for horizontal reaction forces shown in Figure 2-27, the Arcan specimen materials considered were three isotropic materials, namely aluminum, magnesium and SMC-R25 with aluminum having the highest modulus and SMC-R25 the lowest modulus. The fixture material was steel. In examining Figure 2-27, it can be observed that the effect of specimen material on the horizontal reaction force is similar to that observed in Figure 2-26. At loading angles 15 to 75^o, the horizontal reaction force has the lowest value when the specimen material is aluminum

and the highest value when the specimen material is SMC-R25. At 90° loading angle, the effect of specimen material is reversed. The maximum horizontal reaction force with all three specimen materials is at a 45° loading angle.

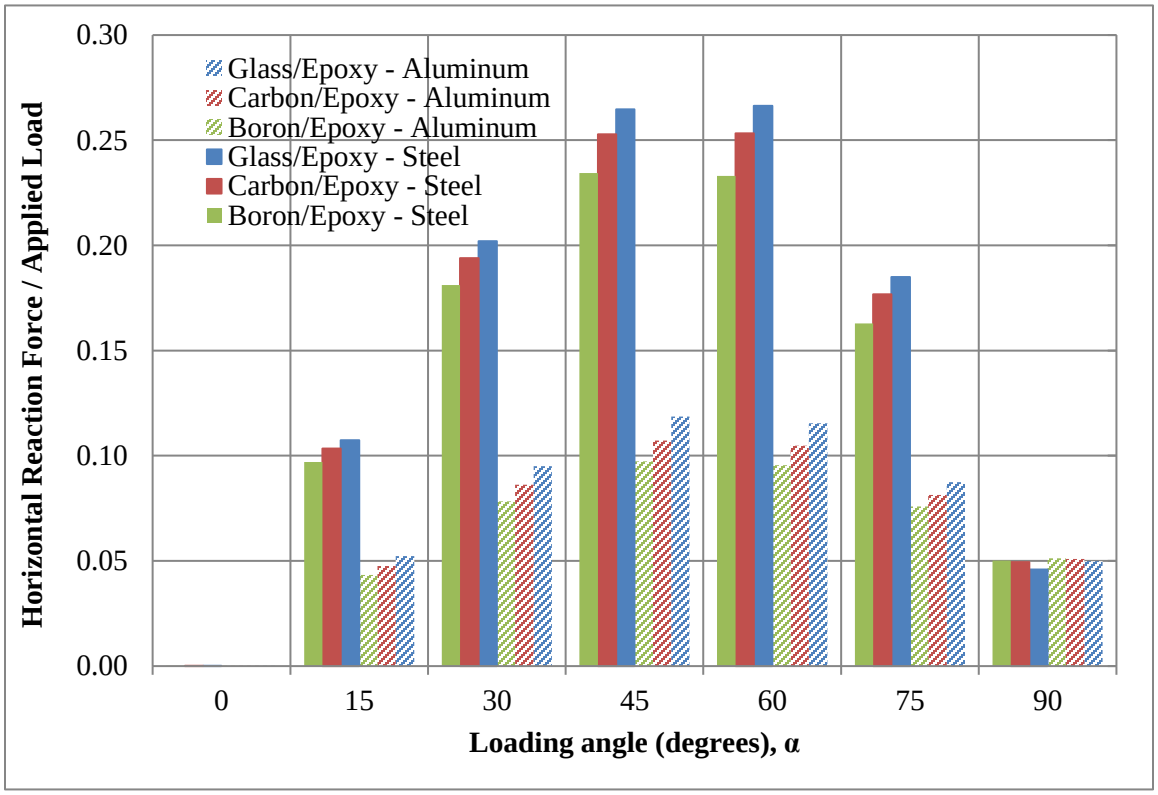

Figure 2-26: Horizontal reaction forces in large 1-2 Arcan specimen.

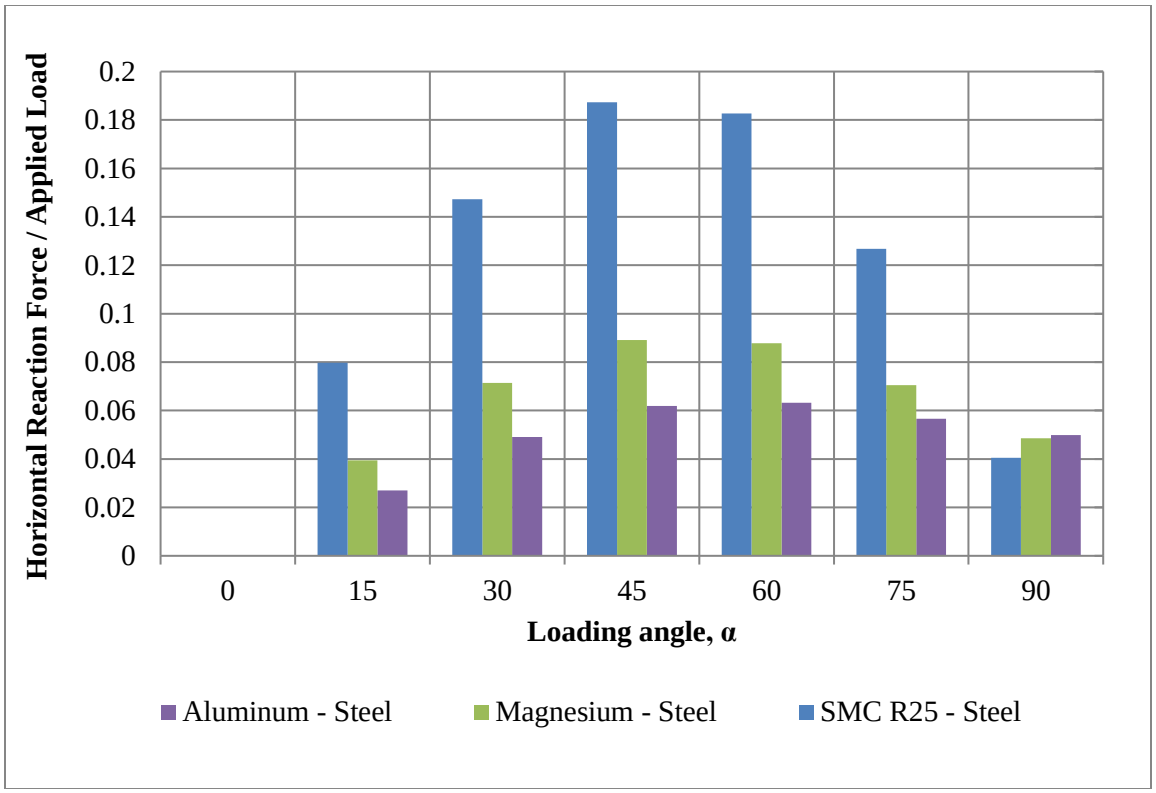

Figure 2-27: Horizontal reaction forces in large Arcan specimens of isotropic materials (the fixture material is steel).

Figure 2-28 shows the relative magnitudes of horizontal reaction forces in small Arcan specimen modelled with GFE, CFE and BFE as the Arcan specimen material. The fixture material is steel. The trend is similar to the one observed with large Arcan specimen. However, in comparing Figure 2-26 and Figure 2-28, it can be observed that the magnitude of the horizontal reaction force is higher with small Arcan specimen in comparison to the large Arcan specimen.

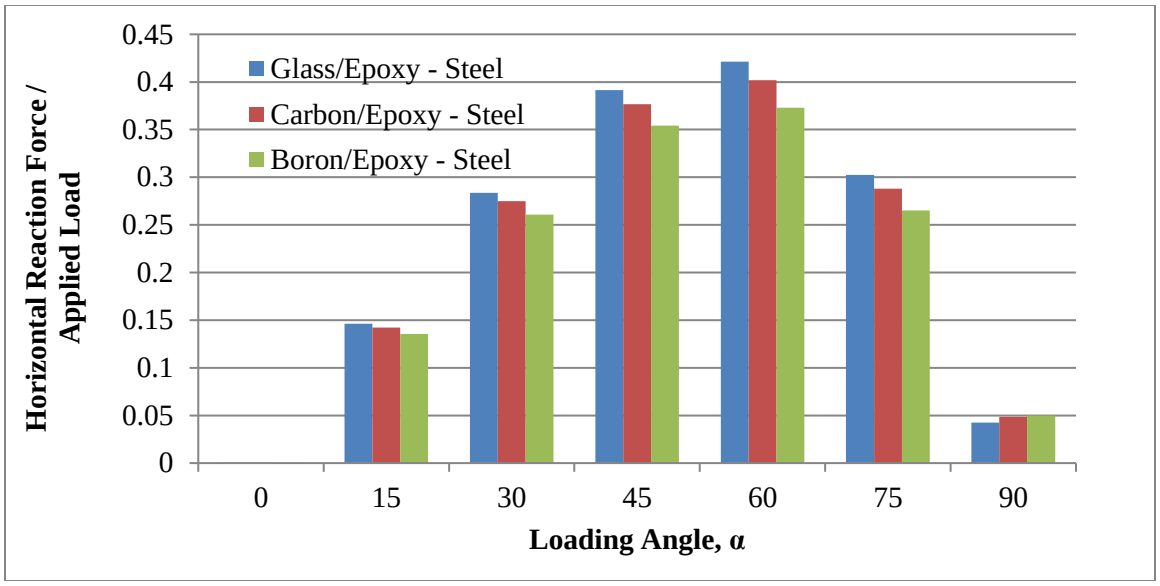

Figure 2-28: Horizontal reaction forces in small 1-2 Arcan specimen.

Figure 2-29 shows a comparison of the horizontal reaction forces in the clamped large and small Arcan specimens. As can be observed in this figure, the small Arcan specimens develop higher reaction loads in comparison to the large Arcan specimen. According to Greer et al. [6], the ratio of the horizontal reaction force and the applied load increases with the increasing ratio of the loading actuator stiffness and the specimen stiffness. In their study, the fixture stiffness was not varied and the load was applied at the end of the loading actuator. In the current study, the load was applied at the pins connecting the fixture and the specimen. Instead of the loading actuator, the fixture connecting the Arcan specimen to the loading pin was taken into consideration. The trends observed in the current study are very similar to the study conducted by Greer et al. In both studies, the effect of the loading angle is also very similar.

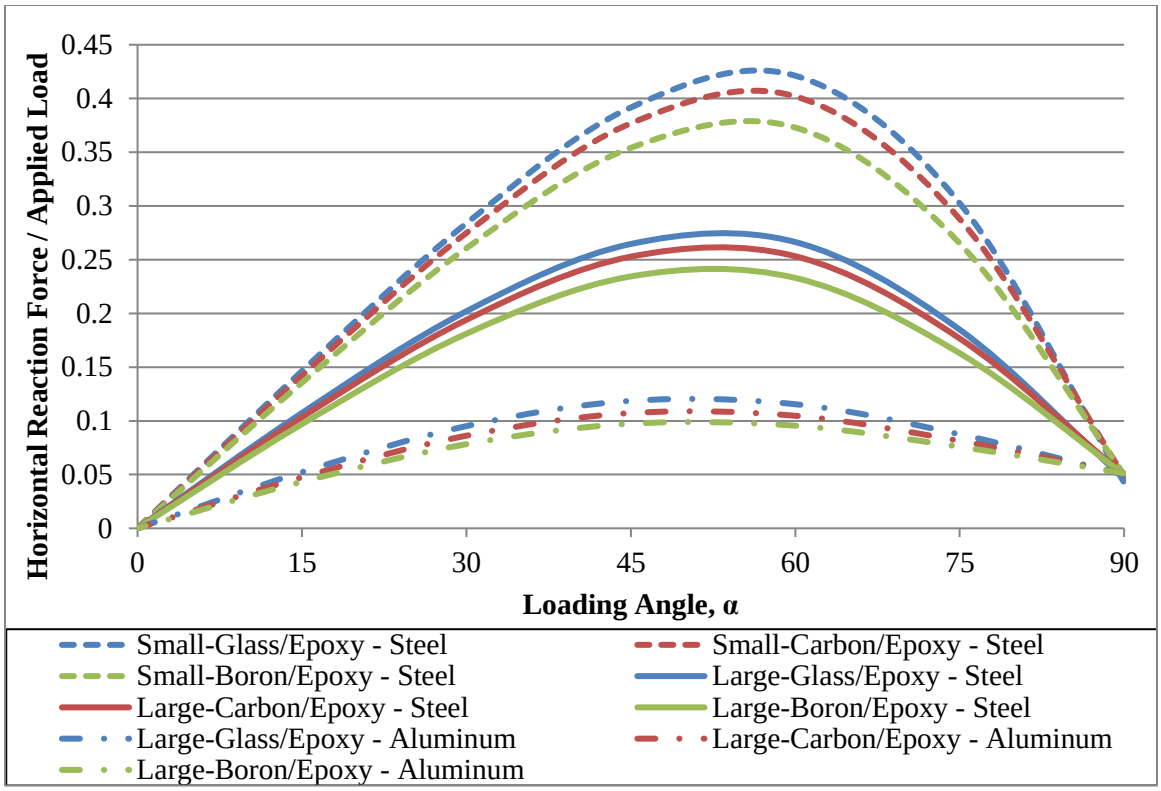

Figure 2-29: Comparison of horizontal reaction forces in small and large 1-2 Arcan specimens.

In Figure 2-26, Figure 2-28 and Figure 2-29, the specimen configuration was 1-2 and the fiber orientation angle was 0^o. Other fiber orientation angles are explored in Figure 2-30 and Figure 2-31 in which the fiber orientation angle was varied from 0 to 90^o in the small Arcan specimen. The material in the specimen is GFE and the fixture material is steel. Figure 2-30 shows that the horizontal reaction force is higher at loading angles greater than 0^o if the fiber orientation angle in the Arcan specimen is 0^o compared to when the fiber orientation angle is 90^o. For 15, 30, 45 and 60^o fiber orientations, the horizontal reaction force first decreases and then increases with increasing loading angle. After reaching a peak, it decreases again. For 75^o fiber orientation, the trend is similar to that observed with 0 and 90^o fiber orientation

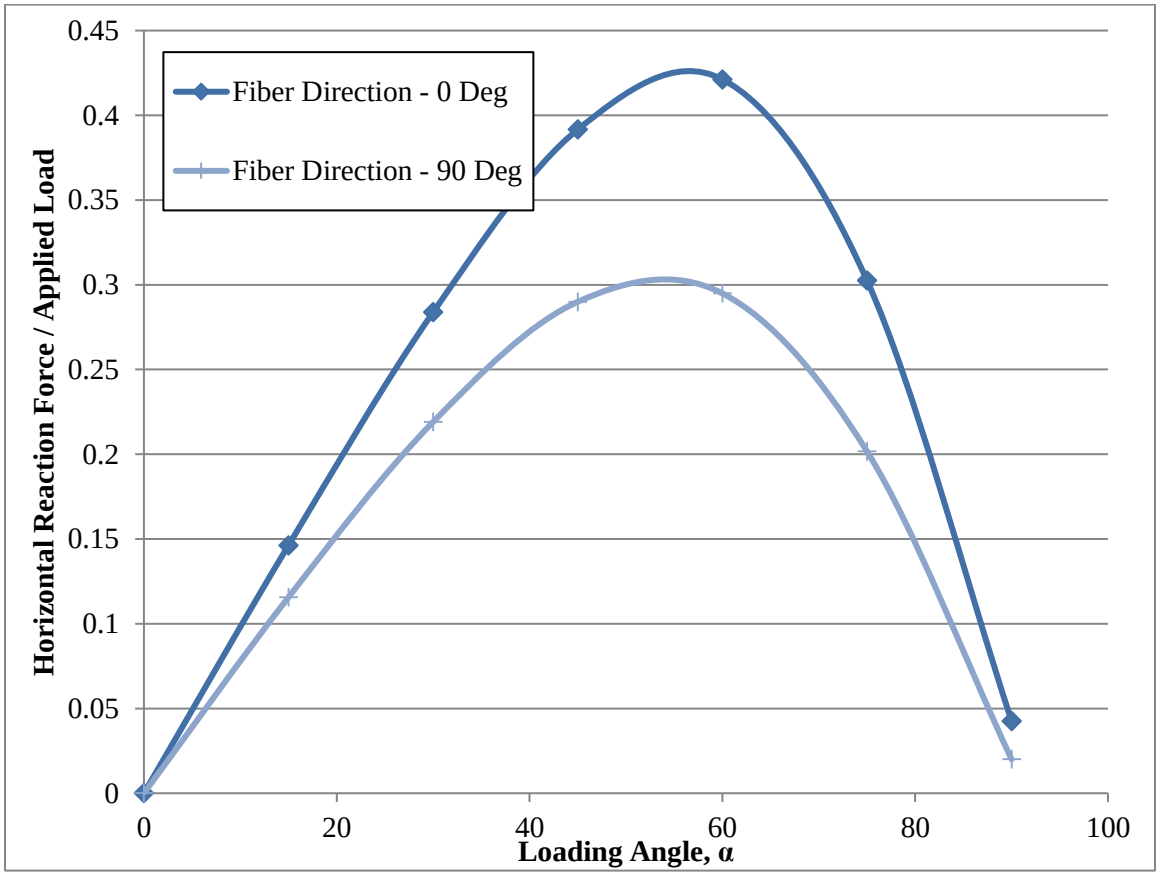

Figure 2-30: Influence of loading angle on horizontal reaction force in small 1-2 Arcan specimen with 0 and 90° fiber orientation angle.

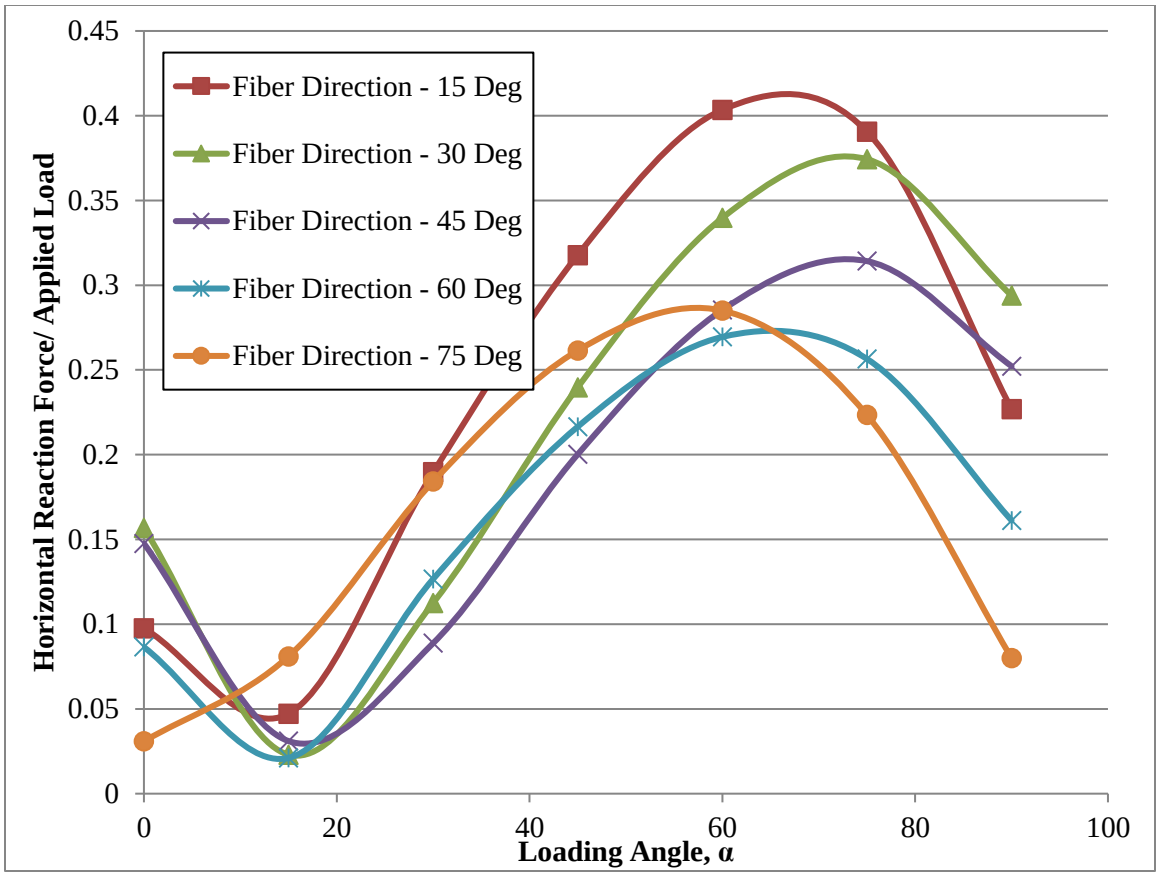

Figure 2-31: Influence of fiber orientation angle (θ) on horizontal reaction force in small 1-2 Arcan specimen

b. Unclamped Boundary Conditions

The horizontal reaction load under the fully clamped condition can be avoided by unclamping the fixture and allowing it to rotate. However, due to the rotation, the loading angle will change. Figure 2-32 shows rotation of the small Arcan fixture when loaded in the un-clamped configuration. The maximum rotation occurs when the loading angle is 45º. The other rotation values shown in Figure 2-32 are normalized with respect to the rotation at 45º loading angle. Also, except for the 90º loading angle, there is very little effect of specimen material modulus on the rotation of the fixture.

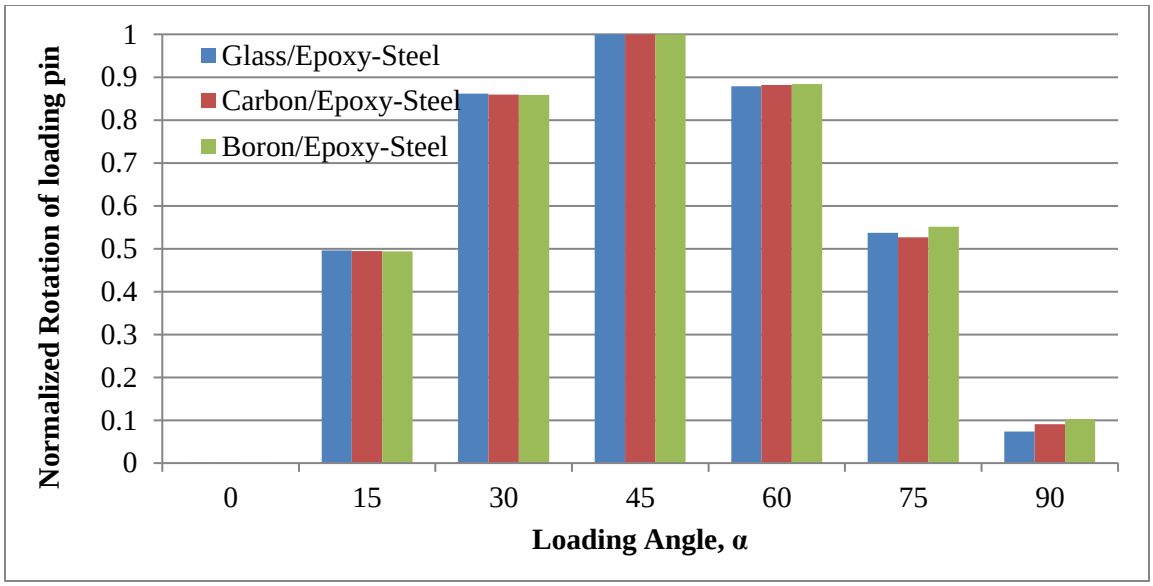

Figure 2-32: Rotation about loading pin of small un-clamped 1-2 Arcan specimen.

2.5 Conclusions

This chapter considers the design of a butterfly-shaped Arcan specimen that can be used for biaxial testing of fiber reinforced composites. Using finite element analysis, the effects of notch radius, notch angle, specimen size, specimen material, clamping condition and fixture material on the stress distribution in the significant section were examined. Since the presence of opposing notches creates stress non-uniformity in the significant section (notch plane) of the specimen, the extent of stress uniformity was considered the measure of effectiveness for the specimen design. Based on this measure, a notch radius of 10 mm and a notch angle of 90^{o} are the optimum notch dimensions for 1-2 specimens. However, a smaller radius is found to be better for 2-1 specimens. Out of the two specimen sizes considered, the smaller specimen with overall outer dimensions of 75 mm x 50 mm produces a more uniform stress distribution than the larger specimen with overall outer dimensions of 75 mm x 75 mm. The difference in stress distributions in the unclamped and clamped specimens is very small when the specimen is either in tension or shear mode of loading. For combined loading modes, the clamped specimens produce higher stresses, which can be attributed to the horizontal reaction loads generated at the loading ends of the clamped specimen. It is shown that the magnitude of the

horizontal reaction load depends on the ratio of the fixture stiffness and specimen stiffness, specimen size, loading angle as well as fiber orientation angle. Large specimen with the highest ratio of fixture stiffness to specimen stiffness produces the smallest horizontal reaction load.

2.6 References

[1] M. Arcan, Z. Hashin, and A. Voloshin, "A method to produce uniform plane-stress states with applications to fiber-reinforced materials," *Exp. Mech.*, vol. 18, no. 4, pp. 141–146, Apr. 1978.

[2] A. Voloshin and M. Arcan, "Pure shear moduli of unidirectional fibre-reinforced materials (FRM)," *Fibre Sci. Technol.*, vol. 13, no. 2, pp. 125–134, Mar. 1980.

[3] A. Voloshin and M. Arcan, "Failure of unidirectional fiber-reinforced materials—New methodology and results," *Exp. Mech.*, vol. 20, no. 8, pp. 280–284, Aug. 1980.

[4] S. C. Hung and K. M. Liechti, "Finite Element Analysis of the Arcan Specimen for Fiber Reinforced Composites under Pure Shear and Biaxial Loading," *J. Compos. Mater.*, vol. 33, no. 14, pp. 1288–1317, Jul. 1999.

[5] S. C. Hung and K. M. Liechti, "An evaluation of the arcan specimen for determining the shear moduli of fiber-reinforced composites," *Exp. Mech.*, vol. 37, no. 4, pp. 460–468, Dec. 1997.

[6] D. Mohr and M. Doyoyo, "Analysis of the Arcan Apparatus in the Clamped Configuration," *J. Compos. Mater.*, vol. 36, no. 22, pp. 2583–2594, Nov. 2002.

[7] J. M. Greer, S. E. Galyon Dorman, and M. J. Hammond, "Some comments on the Arcan mixed-mode (I/II) test specimen," *Eng. Fract. Mech.*, vol. 78, no. 9, pp. 2088–2094, Jun. 2011.

CHAPTER 3 : STRENGTH AND FAILURE CHARACTERISTICS OF A COMPOSITE LAMINATE UNDER BIAXIAL STRESSES

3.1 Introduction

Strength and failure characteristics of unidirectional composite plates under the combined effect of in-plane shear and tensile normal stresses are of great interest for effective design of structural composites. The reason for this interest is that the composite laminates, in general, are weak in shear loading and when combined with tensile normal stress, the shear strength deteriorates even further. The majority of the previously published research on strength and failure characterization utilized tubular specimens under a combination of tension/compression and torsional loadings [1], [2]. A few research has used flat off-axis specimens under tensile loading. The limitations of these test methods are described in Chapter 1. To date, there are no standard tests for determining the biaxial strength characteristics of laminated composites. In the current research, the combined biaxial stress condition was created using a butterfly-shaped Arcan specimen. This chapter describes the Arcan test specimen development and the biaxial strength test results of a $[0/90/0_9/90/0]$ composite laminate using these specimens. It also describes the failure modes observed in these tests and examines the validity of the test results in comparison to the common biaxial failure theories.

The Arcan specimen was developed and used by Arcan and his co-workers [3] for determining shear moduls of composite laminates using shear loading. They also conducted limited number of tests in biaxial test mode [4], [5]. Recently, Gning et al. [6] used Arcan specimens for through-thickness strength measurements of a unidirectional composite laminate under loading angle configuration ranging from 0° to 90° where 0°

corresponds to shear tests and 90° corresponds to tension tests . In their study, the material was a 30-mm thick E-glass/expoxy laminate containing 46 unidirectional fiber layers. The Arcan specimens were machined from the laminate in two diffferent orientations, namely 2-1 and 3-2, where 1, 2 and 3 were, respectively, the fiber direction, transverse direction and thickness direction of the laminate. The Arcan specimens were 5 mm thick and the notch root radius was 2.5 mm. For the 2-1 specimens, fibers were parallel to the notch direction and for the 3-2 specimens, the fibers were transverse to the notch direction. Gning and his co-workers reported that the 3-2 specimens showed linear load-displacement curves independent of the loading angle. The 2-1 specimen's load-displacement curves also had a linear response at loading angles greater than 15°. At 0 and 15° loading angles, the 2-1 specimens exhibited a non-linear load-displacement curve until failure. This non-linearity began at the onset of interlaminar cracks. The 2-1 specimens had a higher load carrying capacity and higher strain to failure in comparison to the 3-2 specimens. Both specimen types exhibited higher scatter in the ultimate failure load at lower loading anlges, but the scatter reduced as the loading angle increased. Regardless of the loading angle, the 2-1 specimens always failed with crack stating at notch tip and running parallel to the notch-to-notch direction. The 3-2 specimens failed due to cracks running diagonally into the clamping plates.

3.2 Experimental

3.2.1 Material

The material used in this study is a 3.3-mm thick E-glass fiber reinforced epoxy laminate composed of 13 layers and a stacking sequence described by $[0/90/0_9/90/0]$. In this laminate, 85 percent of the layers contained 0^o fiber orientation and 15 percent contained 90^o fiber orientation. The original trade name for the material was Scotchply 1002 and it was developed by 3M, Inc. It is now available by the trade name Cyply 1002 from Red Seal Electric Co. Both Scotchply and Cyply laminates were used in this research. They are identified in this chapter as SM and CM, respectively. The nominal fiber volume fraction in the laminate is 45 percent. The other mechanical properties available in the literature are listed in Table 3-1.

Table 3-1: Mechanical properties of 0° unidirectional continuous glass-fiber reinforced epoxy lamina.

Property	Symbol	Value
Density (g/cm^3)	ρ	1.8
Longitudinal Elastic Modulus (GPa)	E_{11}	39.3
Transverse Elastic Modulus (GPa)	E_{22}	9.65
Major Poisson's Ratio	ν_{12}	0.3
In-plane Shear Modulus (GPa)	G_{12}	4.8

3.2.2 Specimens

The butterfly-shaped Arcan specimens contained two opposing notches at the mid-length with 90^o notch angle and 10 mm notch root radius. The specimen thickness was 3 mm. Two different sizes of butterfly-shaped specimens were designed. One is called the large specimen which has an overall size of 75 mm x 75 mm and a significant section area between the notch tips of 159.32 mm^2. Initially, the large specimens were designed and tested in monotonic tensile mode. It was observed that many of these specimens failed in the bolt clamping areas due to the stresses in these areas exceeding the strength of the bolted joint. The specimen size was then reduced to a smaller overall size of 75 mm x 50 mm which had a significant section area of 76.82 mm^2. These specimens are referred to as small specimens. The specimen dimensions are shown in Figure 3-1.

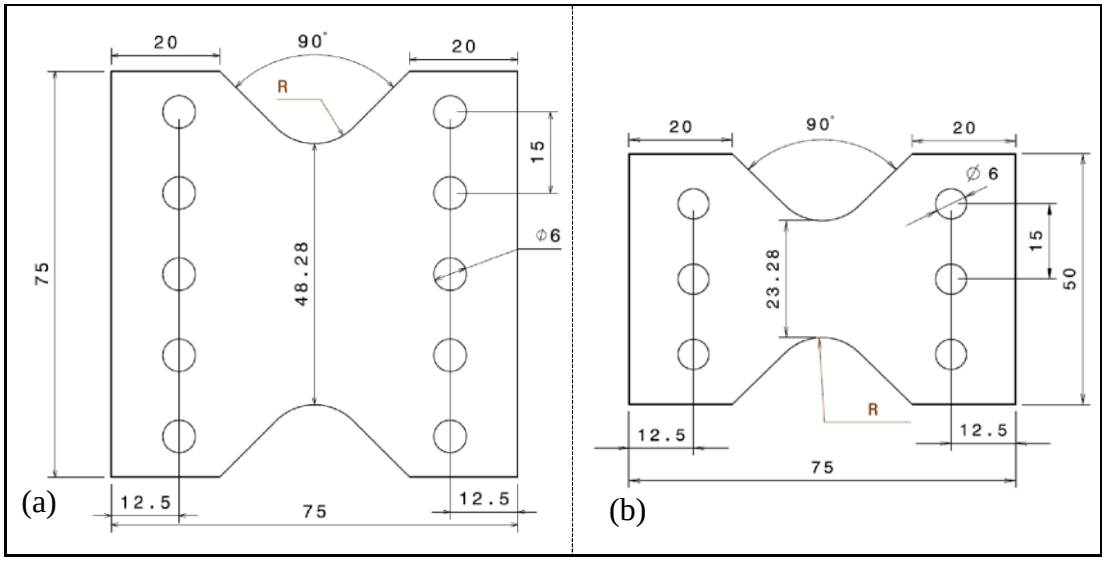

Figure 3-1: Dimensions of a) large and b) small Arcan specimen (thickness = 3.3 mm).

Both large and small Arcan specimens were fabricated using a high speed routing bit with diamond-pattern cutting edge and custom-built templates. While the primary purpose of the template was to obtain the butterfly shape, it also served as a template to drill the 6-mm diameter bolt holes in a secondary operation. Figure 3.2 shows the template used for routing the E-glass/epoxy laminate to obtain small Arcan specimens. A similar but wider template was used during the fabrication of the large Arcan specimens. Figure 3.3 shows a photograph of small Arcan specimens obtained after routing and drilling.

Figure 3-2. Template used for small Arcan specimen fabrication.

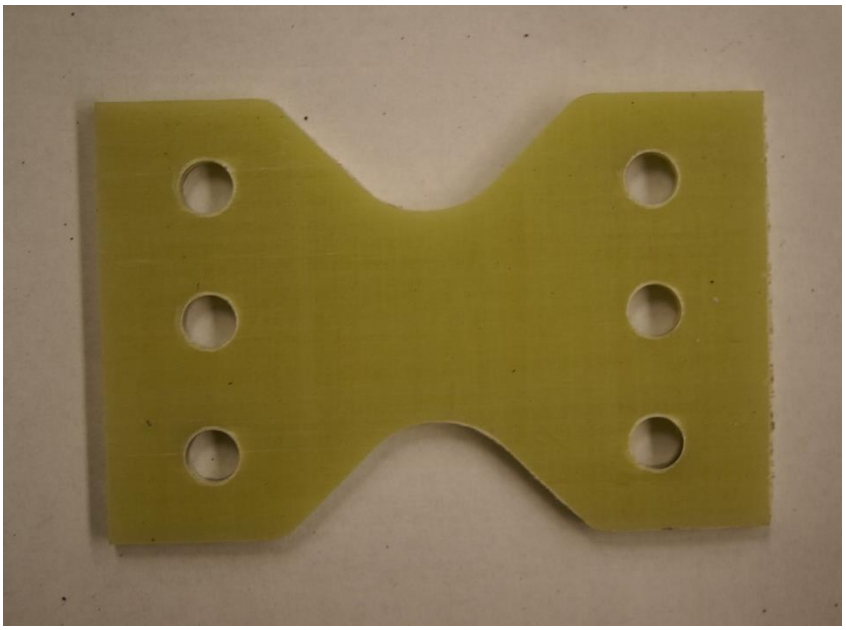

Figure 3-3. Photograph of a small butterfly shaped Arcan specimen.

Two different specimen configurations were prepared: 1) the 1-2 specimens or the longitudinal specimens in which the 0° layers were at a 0^o angle with the length direction of the specimen and 2) the 2-1 specimens or the transverse specimens in which the 0° layers are at a 90^o angle with the length direction of the specimen. Figure 3-4 shows a schematic of the 1-2 and 2-1 specimens. In this figure, the 0° layers are represented by the solid lines and the 90° layers are represented by the dotted lines. In the 1-2 specimens, 11 of the 13 layers or 85% of the layers were the 0^o layers. Similarly, in the 2-1 specimens 11 of the 13 layers or 85% of the layers were the 90^o layers. As can be seen in Figure 3.4, the 0^o layers in the 1-2 and 2-1 specimens were perpendicular and parallel to the significant section, respectively. In addition to the aforementioned specimens, 30° and 45° off-axis small Arcan specimens were also used and tested under monotonic tensile loading. In these specimens, the 0^o layers were at 30^o and 45^o angles to the length direction of the specimen.

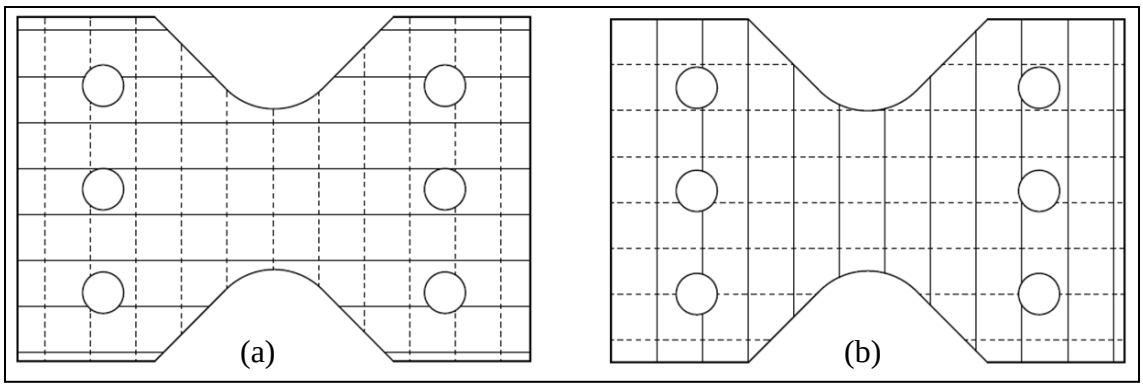

Figure 3-4: (a) 1-2 and (b) 2-1 configuration of the Arcan specimen.

3.2.2 Monotonic Test Procedure

Monotonic tests were conducted in the tensile mode using MTS 810 servo-hydraulic test system with a 100-kN loading capacity. The fixture used for testing Arcan specimens is shown in Figure 3-5. It was mounted on a round loading fixture which consisted of a top half and a bottom half, both machined from 9-mm thick steel plates. Each half of the fixture was made of a front clamping plate and a back clamping plate. The Arcan specimens were mounted between the front and back clamping plates of each

half of the loading fixture using three bolts and nuts for small specimens and 5 bolts and nuts for the large specimens. The clamping torque was 15 N-m. The loading fixture was connected to a loading yoke at each end using three bolts and nuts and the loading yokes were pin-connected to the MTS loading crossheads. A series of circular holes, 15^o apart from each other, near the outer circumference of the clamping plates allowed the loading angle α to vary between 0 and 90^o so that the specimens could be loaded in tension, combined tension and shear, and shear modes.

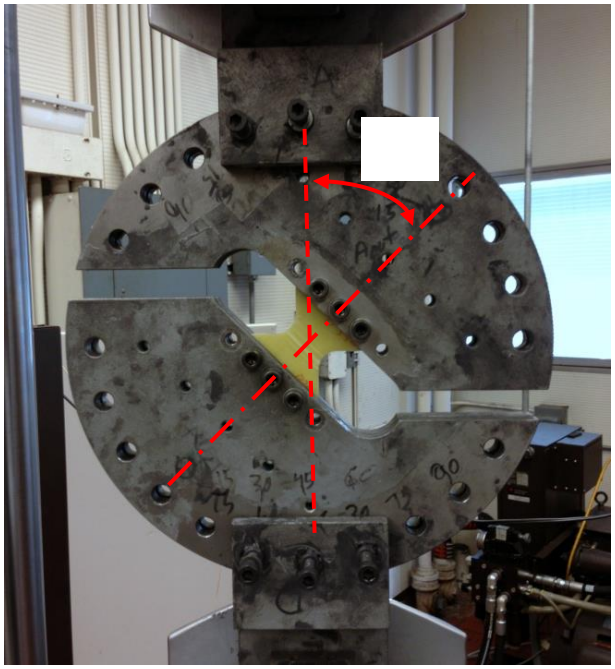

Figure 3-5. Photograph of an Arcan specimen mounted on the test fixture. The loading angle is denoted by α and is measured from the vertical axis of the loading fixture, which is also the loading direction.

As shown in Figure 3.5, the loading angle between the specimen axis and the loading axis is α. If the fiber orientation angle with respect to the specimen axis is θ, then a load applied P on the loading yokes in the loading direction creates two normal load components and a shear load component on the specimen. These load components are

$$\begin{aligned} P_{n1} &= P\cos\alpha.\cos\theta \\ P_{n2} &= P\cos\alpha.\sin\theta \\ P_s &= P\sin\alpha \end{aligned} \qquad (3.1)$$

Based on the significant section area A_o, the average stresses in the significant area are

$$\sigma_{11} = \frac{P_{n1}}{A_o} = \frac{P}{A_o}\cos\alpha.\cos\theta$$
$$\sigma_{22} = \frac{P_{n2}}{A_o} = \frac{P}{A_o}\cos\alpha.\sin\theta \qquad (3.2)$$
$$\tau_{12} = \frac{P_s}{A_o} = \frac{P}{A_o}\sin\alpha$$

For the 1-2 specimens, $\theta = 0^o$ for the 0^o layers and therefore, the average stresses in the significant area are as follows.

$$\sigma_{11} = \frac{P}{A_o}\cos\alpha$$
$$\sigma_{22} = 0 \qquad (3.3)$$
$$\tau_{12} = \frac{P}{A_o}\sin\alpha$$

For the 2-1 specimens, $\theta = 90^o$ for the 0^o layers and therefore, the average stresses in the significant area are as follows.

$$\sigma_{11} = 0$$
$$\sigma_{22} = \frac{P}{A_o}\cos\alpha$$
$$\tau_{12} = \frac{P}{A_o}\sin\alpha$$
$$(3.4)$$

As an example, a load P acting at loading angle $\alpha = 45°$ on a 1-2 specimen as shown in Figure 3-6 will create equal shear load and normal loads of magnitude of $P/\sqrt{2}$, and result in internal normal (σ_{11}) and shear (τ_{12}) stresses in the significant section of the specimen. Their values can be determined as:

$$\sigma_{11} = \frac{P.\cos(45°)}{A_o} = \frac{P}{\sqrt{2}.A_o}$$

$$\tau_{12} = \frac{P.sin(45°)}{A_o} = \frac{P}{\sqrt{2}.A_o}$$

where, A_o is the significant section area, which is 159.32 mm^2 for the large specimens and 76.82 mm^2 for the small specimens.

From Equation (3.3), it can be observed that when $\alpha = 0^o$, $\tau_{12} = 0$ and the significant section of the 1-2 specimens is under pure tension. On the other hand, when $\alpha = 90^o$, $\sigma_{11} = 0$ and the significant section of the 1-2 specimens is under pure shear. Similarly, from Equation (3.4), it can be observed that when $\alpha = 0^o$, $\tau_{12} = 0$ and the significant section of the 2-1 specimens is under pure tension, and when $\alpha = 90^o$, $\sigma_{22} = 0$ and the significant section of the 2-1 specimens is under pure shear.

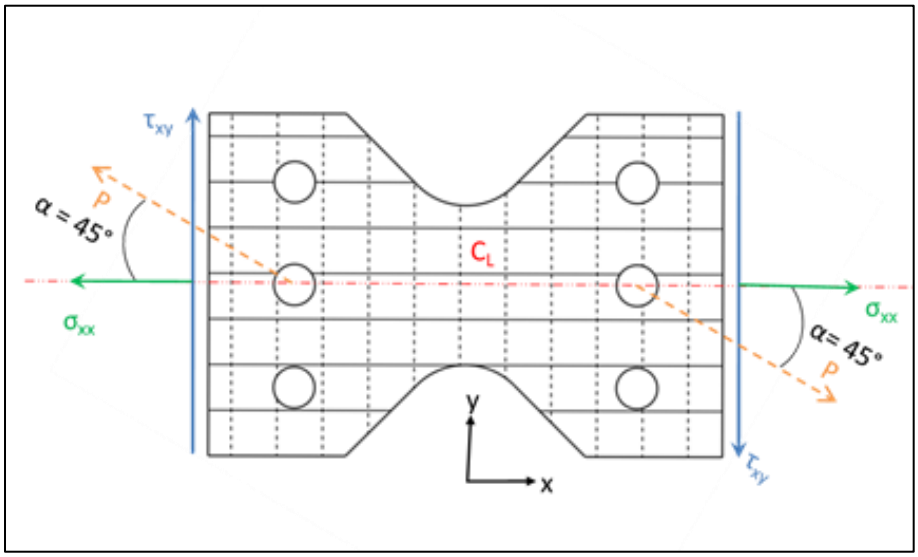

Figure 3-6: Specimen at 45° loading angle.

All monotonic tests were conducted at a testing speed of 2 mm/min. During each test, the specimen was loaded till the load dropped to 10% of the peak test load. Load and displacement signals were recorded throughout the tests at a rate of 100 Hz. While the MTS data acquisition system recorded the load and displacement signals, a high-definition video camera was used to capture and record the damage appearing on the surface of the specimen where it eventually became visible during all monotonic tests.

The video camera was connected to the computer on which the load and displacement signals from the MTS test system were being recorded. The trigger to start the video recording was turned on at the same time the test was started. Due to the translucent nature of the test material it was possible for the high definition camera to look though the thickness of the material until surface or internal deformations nulled the through-thickness visibility. A high intensity 5,000K Daylight CFL bulb was used to further elevate the level of through-thickness visibility.

3.3 Results

3.3.1 Large Arcan Specimens

The results from the monotonic tests of large Arcan specimens are given in Table 3-2 for 1-2 specimens and Table 3-3 for 2-1 specimens. Failure in the 1-2 specimens occurred around the bolt holes for loading angles $\alpha \leq 45°$. Bolt-hole failure instead of failure in the significant section for $\alpha \leq 45^o$ was due to very high tensile normal stress component σ_{11} acting normal to the plane of the bolt hole and the specimens were much more prone to fail at the bolt holes rather than at the significant section. Bolt hole failure resulted from net-tension failure, shear-out failure or a combination of both net-tension and shear-out. Figure 3-7 shows failure of a 1-2 specimen tested at 45° loading angle, in which bolt hole failures included both shear-out failure as well as net-tension. For $60° \leq \alpha \leq 90°$, failure occurred in the significant section as shown in Figure 3-8. The 0^o-layers in these specimens show shear buckling as well as matrix/interface failure between the fibers.

Table 3-2: Monotonic test results of large 1-2 specimens.

Specimen Number	Testing Mode	Loading angle, α (Deg.)	Number of bolt holes at each end	Peak load, kN	Failure location
SM2--1-2	Tension	0	5	40.50	Bolt holes
SM1--1-2	Tension	0	3	21.44	Bolt holes edge tear
SM14--1-2	Combined	15	5	31.48	Corner bolts
SM15--1-2	Combined	15	5	27.94	Corner bolts
SM9--1-2	Combined	30	5	24.49	Bolt holes edge tear
SM10--1-2	Combined	30	5	27.24	Corner bolts
SM7--1-2	Combined	45	5	21.26	Corner bolts
SM6--1-2	Combined	45	5	20.38	3 bolts from each edge
SM8--1-2	Combined	45	3	17.56	Corner bolts
SM11--1-2	***Combined***	***60***	***5***	***18.03***	***Significant section***
SM12--1-2	***Combined***	***60***	***5***	***19.37***	***Significant section***
SM16--1-2	***Combined***	***75***	***5***	***15.48***	***Significant section***
SM17--1-2	***Combined***	***75***	***5***	***14.90***	***Significant section***
SM3--1-2	***Shear***	***90***	***5***	***13.22***	***Significant section***
SM4--1-2	***Shear***	***90***	***3***	***13.00***	***Significant section***
SM5--1-2	***Shear***	***90***	***5***	***12.62***	***Significant section***

Table 3-3: Monotonic test results of large 2-1 specimens.

Specimen Number	Testing Mode	Loading angle, α (Deg.)	Number of bolt-holes at each end	Peak load, kN	Failure location
SM2--2-1	Tension	0	5	12.42	Bolt holes
SM6--2-1	***Tension***	***0***	***3***	***14.29***	***Significant section***
SM11--2-1	Combined	15	3	9.93	Bolt holes
SM9--2-1	Combined	30	5	11.29	Bolt holes
SM7--2-1	Combined	***45***	***5***	***9.50***	***Significant section***
SM8--2-1	Combined	***45***	***3***	***10.41***	***Significant section***
SM10--2-1	Combined	***60***	***5***	***9.66***	***Significant section***
SM12--2-1	Combined	***75***	***3***	***9.70***	***Significant section***
SM3--2-1	***Shear***	***90***	***3***	***9.58***	***Significant section***
SM4--2-1	***Shear***	***90***	***3***	***9.51***	***Significant section***
SM5--2-1	***Shear***	***90***	***3***	***9.83***	***Significant section***

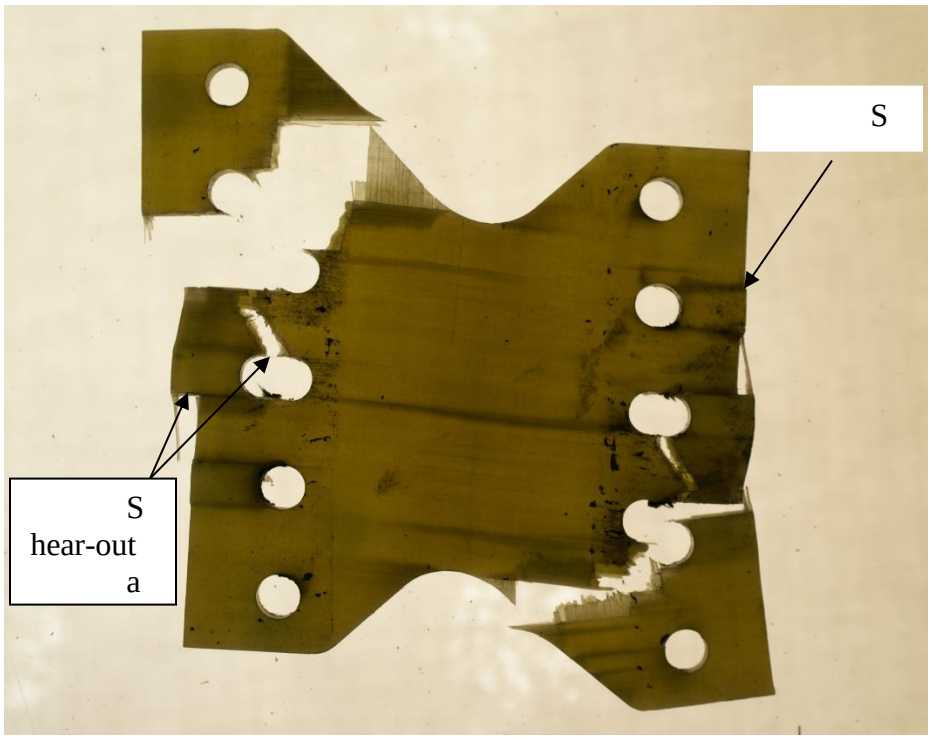

Figure 3-7: Bolt-hole failures in specimen SM6--1-2, tested at 45° loading angle.

The 2-1 specimens had a different failure mode in comparison to the 1-2 specimens. All 2-1 specimens failed in the significant section for $\alpha \geq 45^{o}$. Out of the two specimens tested at loading angle $\alpha = 0^{o}$, one failed in the significant section. The photograph of this specimen shown in Figure 3-9 indicates tensile failure of the 90^{o} layers in the significant section; however, there is also evidence of delamination between the 90 and 0^{o} layers on both sides of the tensile crack in the 90^{o} layers. Final failure of the specimen took place with the tensile failure of the fibers in sub-surface 0^{o} layers. Figure 3-10 and Figure 3-11 show photographs of 2-1 specimens loaded at 90^{o} and 45^{o} loading angles, respectively. The failure surfaces of 2-1 specimens subjected to 60° and 75° loading angle are similar to the ones shown on Figure 3-11. In all of these cases, failure was initiated by shear, but subsurface delamination and fiber failure can also be seen.

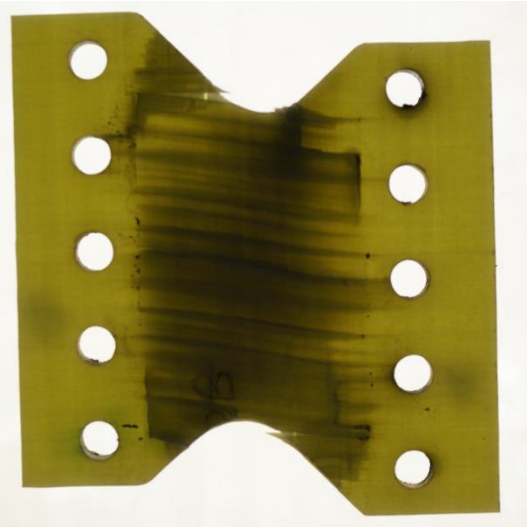

Figure 3-8: Failure surface of a 1-2 specimen subjected to combined tensile and shear loads ($\alpha \geq 60^o$).

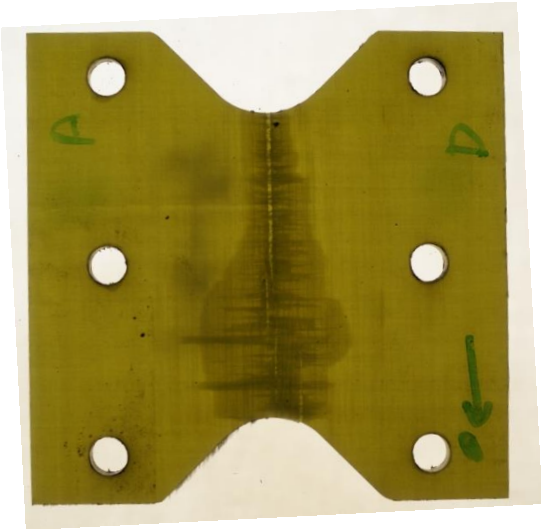

Figure 3-9: Failure surface of a 2-1 specimen subjected to tensile load ($\alpha = 0^o$).

Figure 3-10: Failure surface of a 2-1 specimen subjected to shear load ($\alpha = 90^o$).

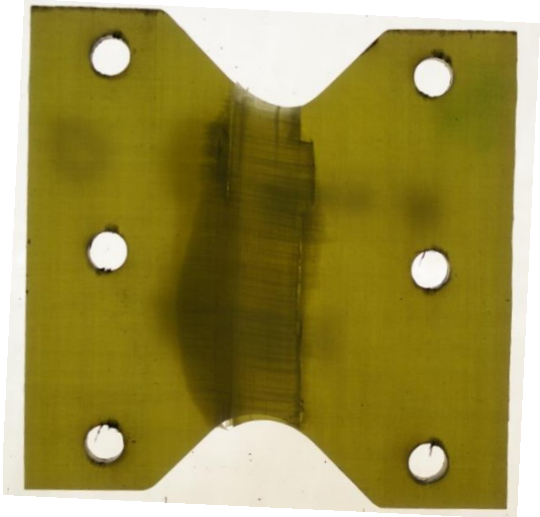

Figure 3-11: Failure surface of a 2-1 specimen subjected to combined tensile and shear loads ($\alpha = 45$, 60 and 75^o).

Figure 3-12, Figure 3-13 and Figure 3-14 show the load-displacement responses obtained in monotonic testing of the 1-2 and 2-1 Arcan specimens. It can be seen in these figures that all the load-displacement responses are linear at low loads, but becomes non-linear as the load increased. The initial stiffness of the 1-2 and 2-1 specimens is very

similar at 45° loading angle and shear loads. The knee at which linear response changes to non-linear response corresponds to damage development in the material. The 1-2 specimens were able to sustain increasing load above the knee, whereas the 2-1 specimens failed slightly above the load at knee. The load carrying capacity of the 1-2 specimens is higher than the 2-1 specimens for all loading angles. The knee in the 1-2 specimens is thought to occur due to complete/partial failure of the 90º-layers.

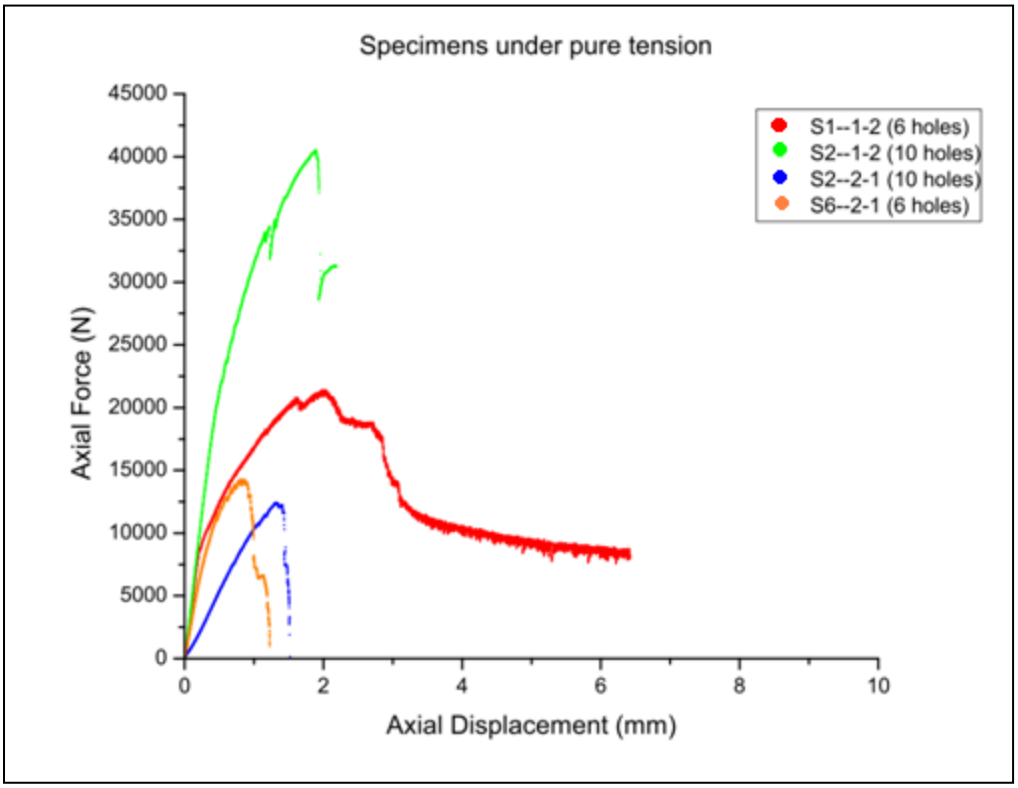

Figure 3-12: Load vs. displacement curves for large Arcan specimens under tensile load (loading angle $\alpha = 0^{o}$).

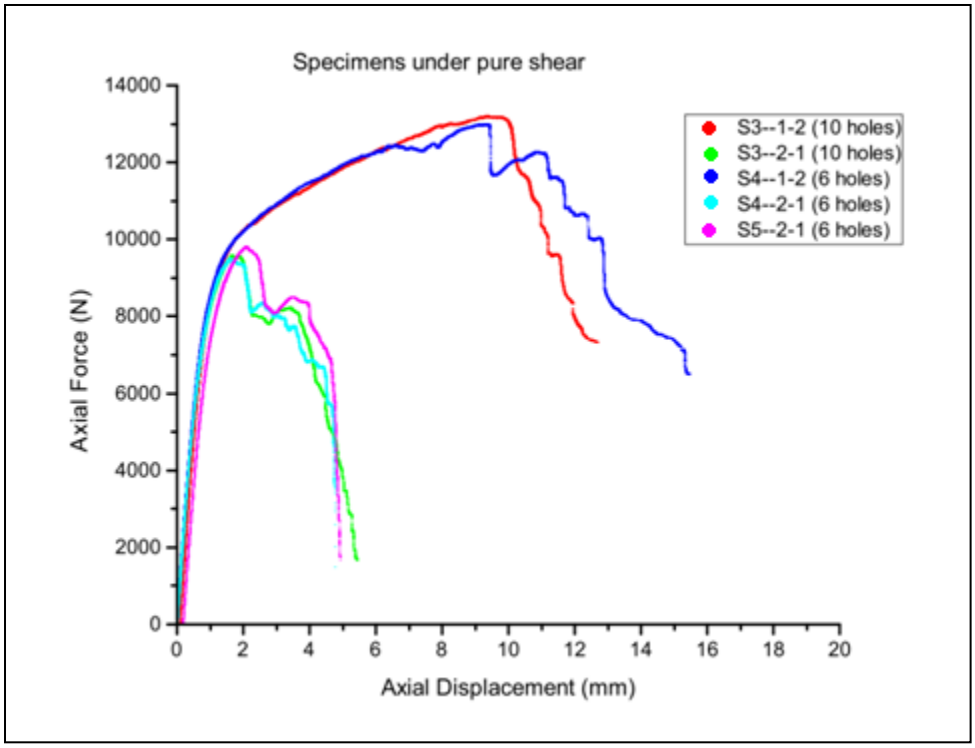

Figure 3-13: Load vs. displacement curves for large Arcan specimens under shear load (Loading angle $\alpha = 90^{o}$).

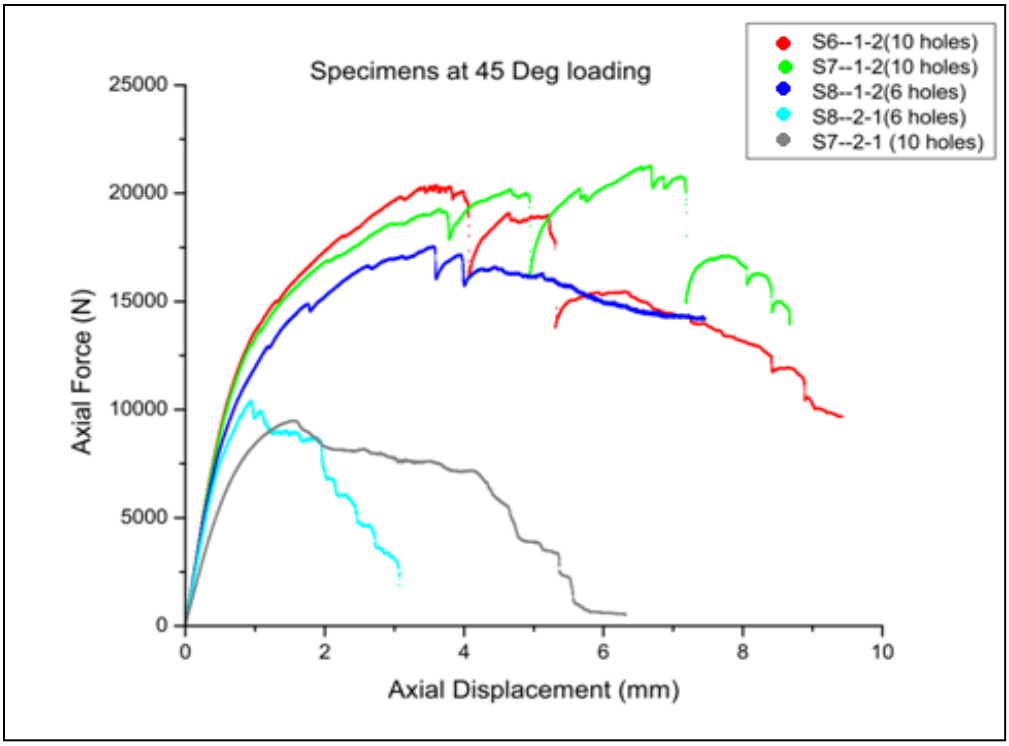

Figure 3-14: Load vs. displacement curves for large Arcan specimens at 45° loading angle.

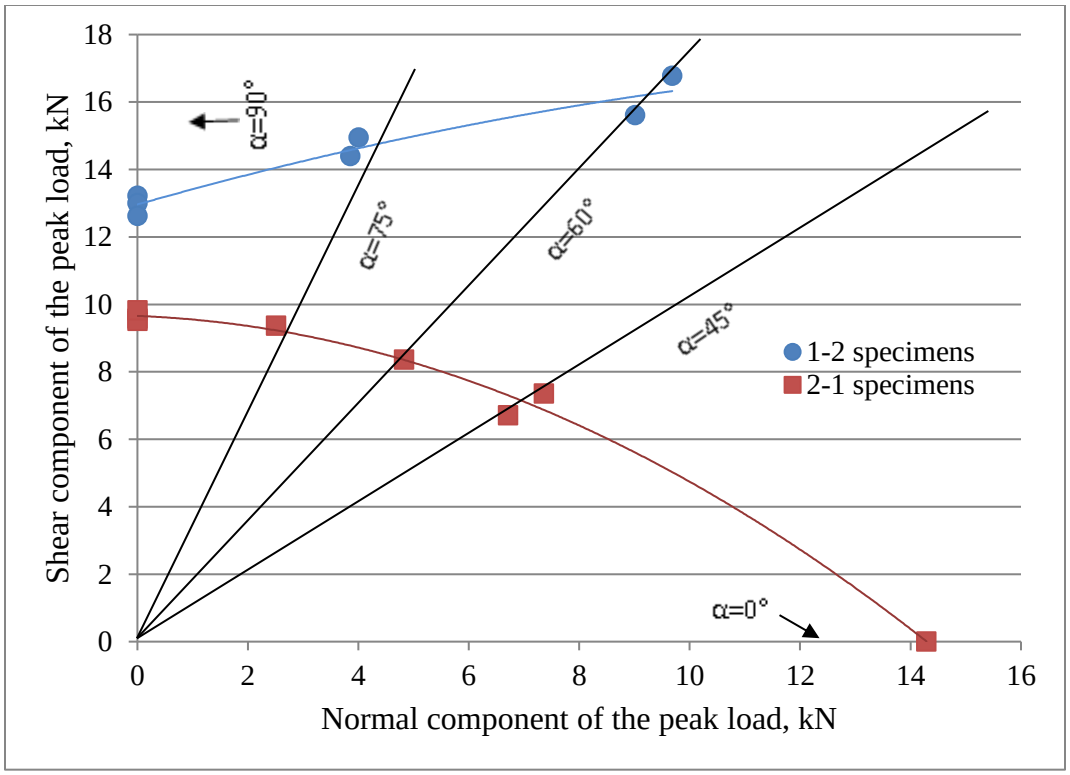

Figure 3-15: Components of the peak load for the specimens that failed in the significant section.

Figure 3-15 shows a plot of shear component of the peak load vs. the normal component of the peak load for the specimens that failed in the significant section. The failure loads of the 1-2 and 2-1 specimens under shear (i.e., at $\alpha = 90^{o}$) are not equal. For the 2-1 specimens, the normal component increased while the shear component decreased with decreasing loading angle. For the few 1-2 specimens that failed in the significant section, both normal and shear components of the peak load increased with decreasing loading angle. Thus, it appears that the failure envelopes for the 1-2 specimens and the 2-1 specimens are significantly different.

3.3.2 Small Arcan Specimens

Since most large Arcan specimens at loading angles $\alpha \leq 45^{o}$ failed in the bolt hole area and not in the significant section, small Arcan specimens were designed with smaller significant section area to induce failure in the significant section. Table 3-4 shows the specimen configurations and loading angles at which the monotonic tests were conducted

using the small Arcan specimen design. The results from the monotonic tests for small Arcan specimen are shown in Table 3-5 for 1-2 specimens and Table 3-6 for 2-1 specimens. Unlike some of the large Arcan specimens, none of the small specimens failed at the bolt holes.

Table 3-4: Specimen configurations and loading angles used with small Arcan specimens.

Loading Angle (°)	Specimen Configuration	
	1-2	2-1
0	No	Yes
15	Yes	Yes
30	Yes	Yes
45	Yes	Yes
60	Yes	Yes
90	Yes	Yes

Table 3-5: Monotonic test results of small 1-2 specimens.

Specimen Number	**Loading angle, α (Deg.)**	**Knee load, kN**	**Peak load, kN**	**Normal stress at knee load, MPa**	**Shear stress at knee load, MPa**	**Normal stress at peak load, MPa**	**Shear stress at peak load, MPa**
SM6--1-2	15	14.08	22.86	177.04	47.44	287.44	77.02
SM5--1-2	15	12.06	22.57	151.64	40.63	283.79	76.04
SM4--1-2	30	7.58	18.08	85.45	49.34	203.82	117.68
SM3--1-2	30	6.56	16.86	73.95	42.70	190.07	109.74
CM-04	30	9.15	15.34	103.15	59.55	172.93	99.84
CM-03	30	8.81	15.34	99.32	57.34	172.93	99.84
SM2--1-2	45	5.42	14.03	49.89	49.89	129.14	129.14
SM1--1-2	45	5.12	11.98	47.13	47.13	110.27	110.27
CM-08	45	5.81	12.90	53.48	53.48	118.74	118.74
CM-07	45	5.26	11.76	48.42	48.42	108.25	108.25
SM8--1-2	60	4.35	10.88	28.31	49.04	70.81	122.65
SM7--1-2	60	4.55	10.45	29.61	51.29	68.02	117.81
SM10--1-2	90	3.84	6.82	0.00	49.99	0.00	88.78
SM9--1-2	90	3.71	6.94	0.00	48.29	0.00	90.34
CM-11	90	4.14	6.84	0.00	53.89	0.00	89.04
CM-10	90	4.17	6.80	0.00	54.28	0.00	88.52
CM-09	90	3.93	6.27	0.00	51.16	0.00	81.62

Table 3-6: Monotonic test results of small 2-1 specimens.

Specimen Number	Loading angle, α (Deg.)	Knee load, kN	Peak load, kN	Normal stress at knee load, MPa	Shear stress at knee load, MPa	Normal stress at peak load, MPa	Shear stress at peak load, MPa
SM2--2-1	0	3.74	8.66	48.69	0.00	112.73	0.00
SM1--2-1	0	3.74	8.13	48.69	0.00	105.83	0.00
SM4--2-1	15	3.23	7.64	40.61	10.88	96.06	25.74
SM3--2-1	15	3.56	7.63	44.76	11.99	95.94	25.71
SM10--2-1	30	2.70	6.40	30.44	17.57	72.15	41.66
CM-02	30	2.80	6.24	31.57	18.22	70.35	40.61
CM-01	30	2.79	5.77	31.45	18.16	65.05	37.56
SM6--2-1	45	2.78	5.44	25.59	25.59	50.07	50.07
SM5--2-1	45	2.49	5.09	22.92	22.92	46.85	46.85
CM-05	45	2.19	5.12	20.16	20.16	47.13	47.13
SM8--2-1	60	2.43	4.64	15.82	27.39	30.20	52.31
SM7--2-1	60	2.44	4.39	15.88	27.51	28.57	49.49
SM12--2-1	90	2.34	4.68	0.00	30.46	0.00	60.92
SM11--2-1	90	2.34	4.47	0.00	30.46	0.00	58.19
CM-13	90	2.05	4.25	0.00	26.69	0.00	55.32
CM-12	90	2.13	4.35	0.00	27.73	0.00	56.63

Figure 3-16 and Figure 3-17 show the load-displacement curves of small 1-2 and 2-1 Arcan specimens, respectively. It is seen that the monotonic behavior of both specimen configurations is highly dependent on the loading angle. Furthermore, the load carrying capacity of the material decreases with increasing loading angle whereas the displacement-at-failure increases. Unlike the 2-1 specimens, the 1-2 specimens at $\alpha \geq 45°$ show a 'knee' load beyond which the response changes. Figure 3-18 shows a comparison of the 1-2 and 2-1 specimens at $\alpha = 90°$, i.e., under shear load. It is seen that the behavior of the two specimen configurations is the same until the knee load of the 1-2 specimen. The 2-1 specimens fail at loads corresponding to the knee load of the 1-2 specimens.

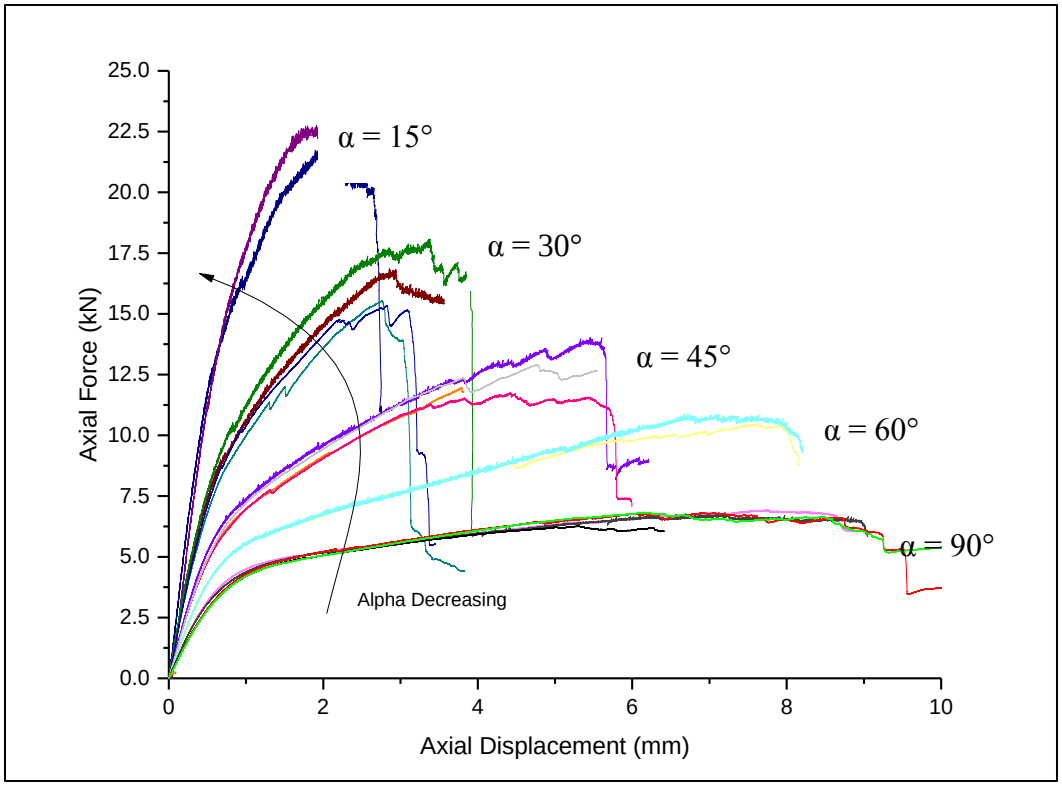

Figure 3-16: Load vs. displacement curves of small 1-2 Arcan specimens in monotonic tensile loading.

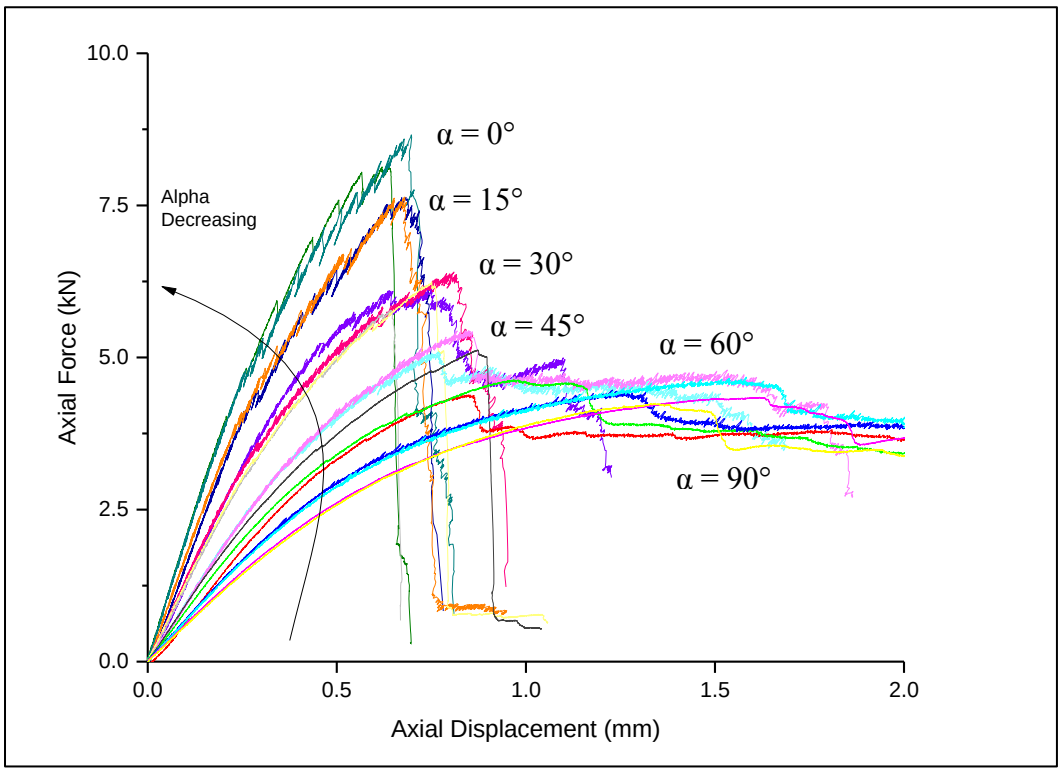

Figure 3-17: Load vs. displacement curves of small 2-1 Arcan specimens in monotonic tensile loading.

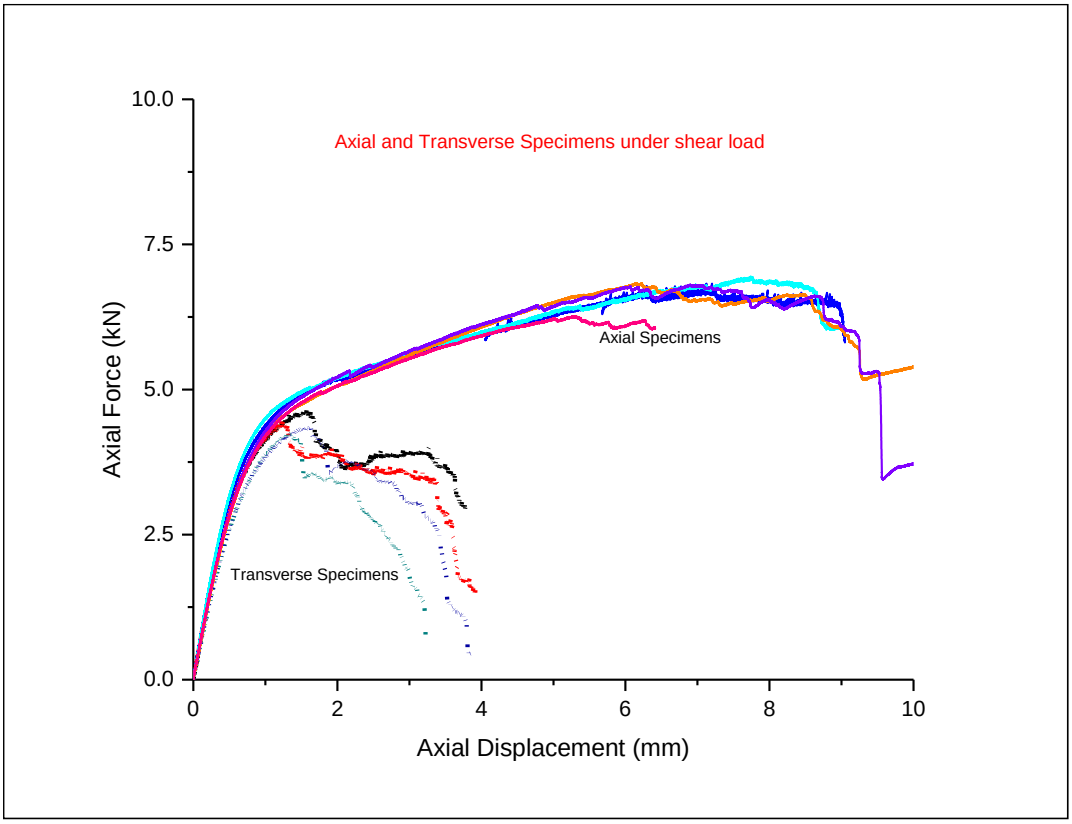

Figure 3-18: Tensile behavior of small 1-2 and 2-1 specimen at 90° loading angle.

Figure 3-19 shows a plot of the shear component vs. the normal component of the knee load for small Arcan specimens. Figure 3-20 shows a similar plot but using the peak load instead of the knee load. As expected, it is seen that the normal component of both knee and peak loads increases with decreasing loading angle whereas the shear component decreases.

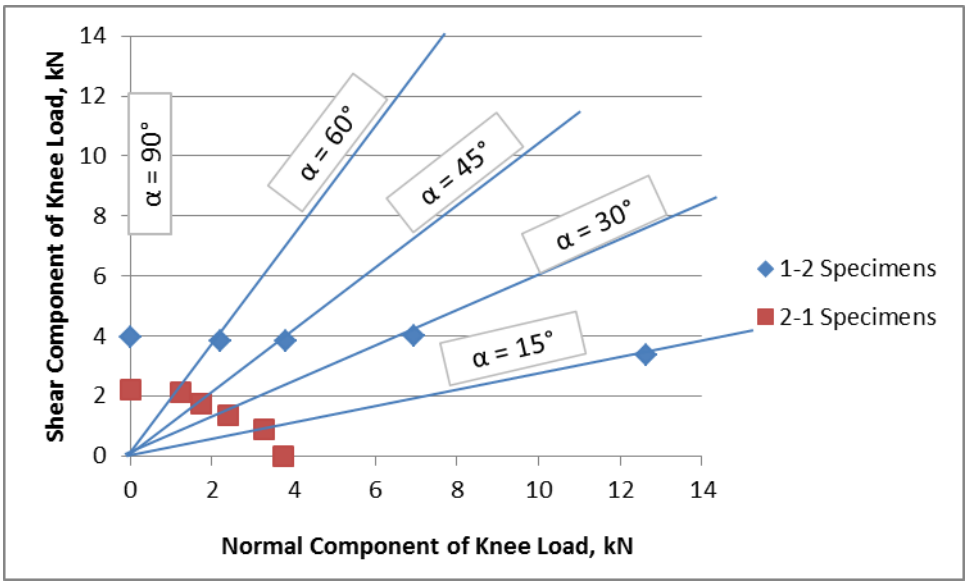

Figure 3-19: Components of the knee load for the small Arcan specimens

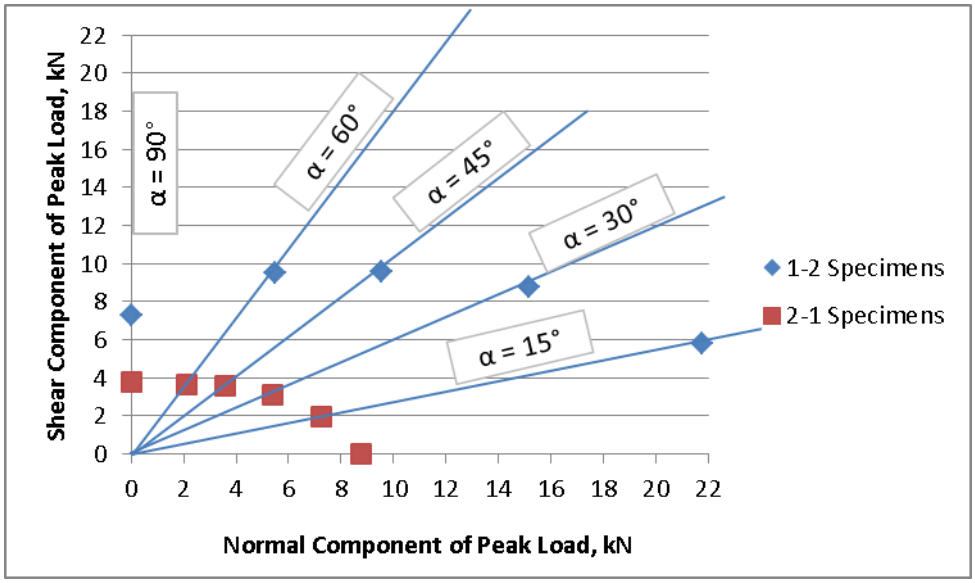

Figure 3-20: Components of the peak load for the small Arcan specimens

3.3.3 Off-Axis Small Arcan Specimens

The off-axis specimens with 30° and 45° fiber orientation angles were tested in monotonic loading with 0° loading angle. Even though the external load acts at 0° loading angle, it creates axial (σ_{11}), transverse (σ_{22}) and shear (τ_{12}) in the off-axis specimens. The magnitudes of these three stresses are equal for a 45° off-axis specimen.

The monotonic test results from these specimens are shown in Table 3-7. Figure 3-21 and Figure 3-22 show the load-displacement curves of the 30° and 45° off-axis small Arcan specimens, respectively. Figure 3-23 shows a comparison of their load-displacement curves. It is seen that the initial stiffness of both 30° and 45° specimens is similar though both peak load and displacement-at-failure are higher for the 30° specimens.

Table 3-7: Monotonic test results of large 1-2 specimens.

Specimen	Off-axis angle (°)	Peak Load, kN	Average Peak Load, kN
NSM-T-30-1-0DEG	30	10.70	10.56
NSM-T-30-2-0DEG	30	10.03	
NSM-T-30-3-0DEG	30	10.94	
SM-T45-1-0deg	45	9.10	8.99
SM-T45-2-0deg	45	9.11	
SM-T45-3-0deg	45	8.77	
SM-T45-4-0deg	45	8.99	

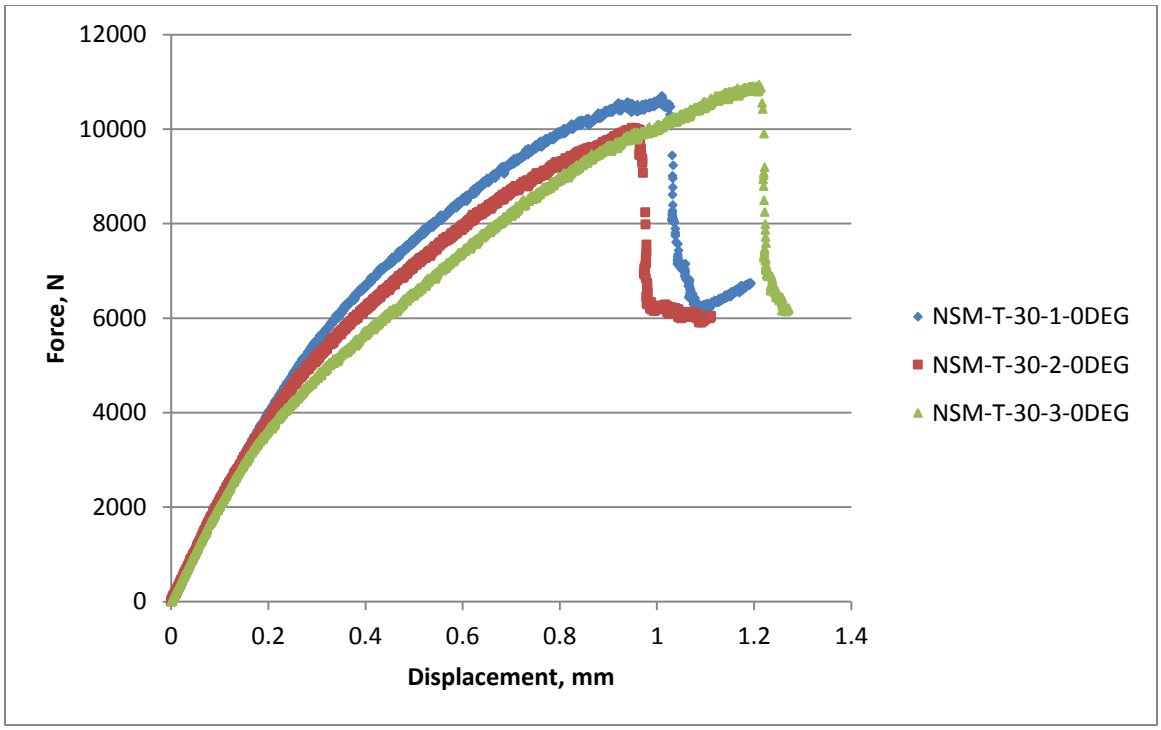

Figure 3-21: Tensile behavior of 30° off-axis small specimens under tensile load.

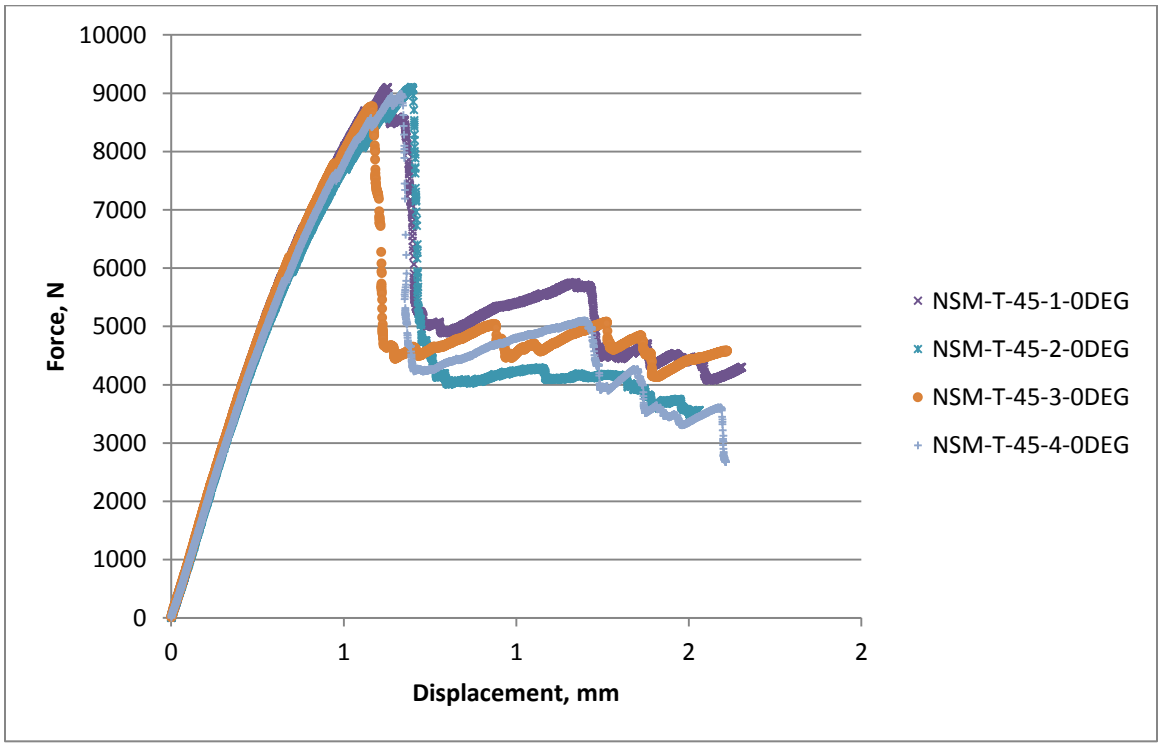

Figure 3-22: Tensile behavior of 45° off-axis small specimens under tensile load.

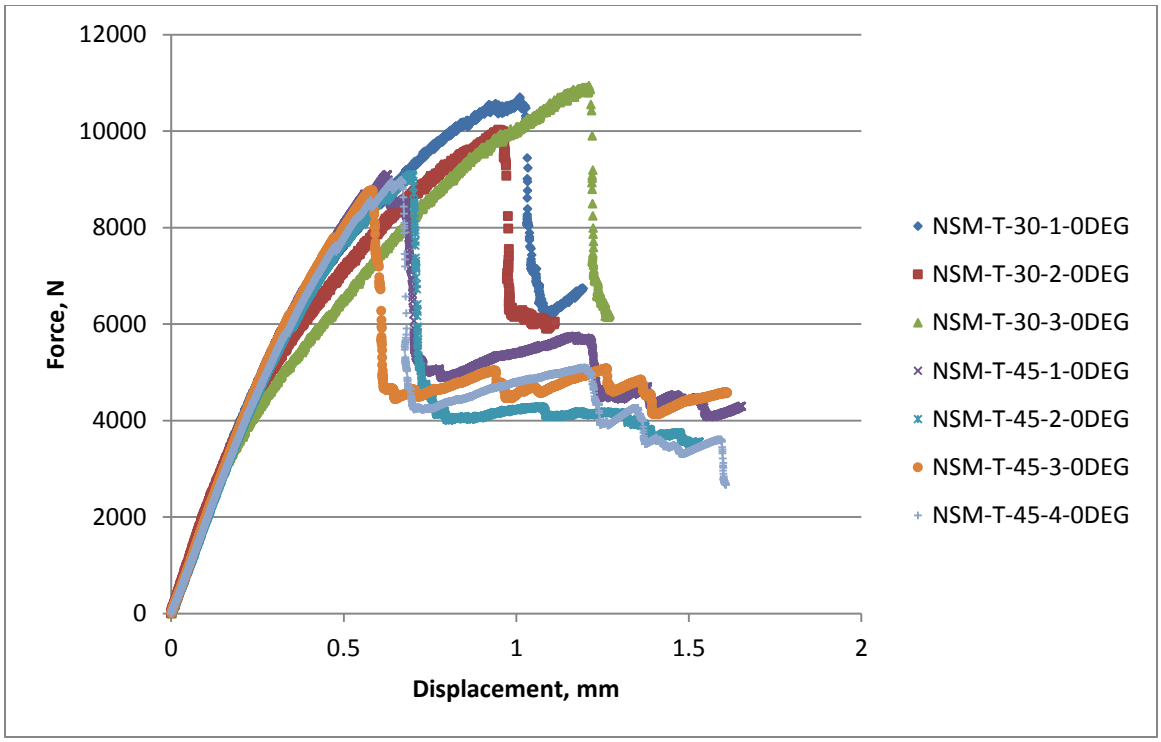

Figure 3-23: Tensile behavior of 30° and 45° off-axis small specimens under tensile load.

3.3.4 Damage Development in Monotonic Loading

Figure 3-24 through Figure 3-28 show sequence of damage development on the front surface of small 1-2 specimens as recorded by the video camera during monotonic tensile loading. The loading angles are 15°, 30°, 45°, 60° and 90°. For these specimens, the load-displacement curve was linear until failure was initiated at the ends of the notch radius on the opposite corners of specimen. These cracks were parallel to the fibers in the 0^o layers and started to appear at the knee load. As the load was increased further, the specimens started to show evidence of shear buckling. The 0^o fibers were deformed into S-shapes due to the shear component of the applied load. The dark areas adjacent to the S-shaped fibers indicate inter-fiber matrix cracking in the 0^o layers and delamination between the 0 and 90^o layers. The degree of shear buckling increased as the shear component of the load increased with increased loading angle. During this period of loading, the load-displacement curve became non-linear. The appearance of small load drops corresponded to generation of additional cracks in the triangular areas on the

opposite corners of the specimen and after the peak load was reached, these triangular areas started to separate from the specimen.

Damage progression in 2-1 specimens is shown in Figure 3-29 through Figure 3-34. The predominant damage in 2-1 specimens was matrix cracking in the 90^o layers. Damage became visible on the surface of each specimen as the load-displacement curve began to deviate from its original linear response. At 0, 15 and 30^o loading angles, the tensile failure in the matrix was due to higher normal stress component. At higher loading angles, shear failure occurred more due to higher shear stress component. At 45, 60 and 90^o loading angles shear buckling of the 0^o fibers in the subsurface 0^o layers was also visible (Figure 3-36).

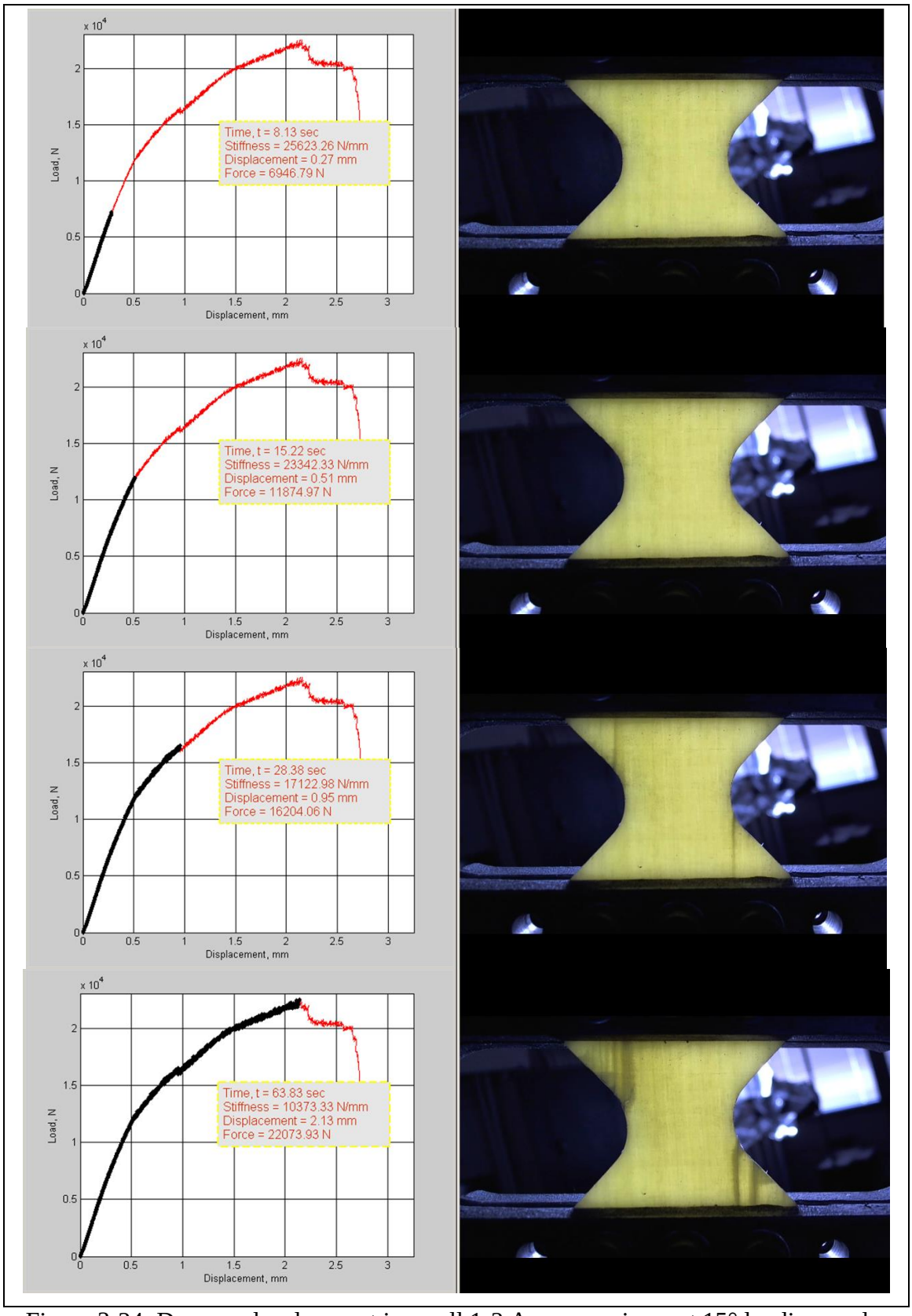

Figure 3-24: Damage development in small 1-2 Arcan specimen at 15° loading angle.

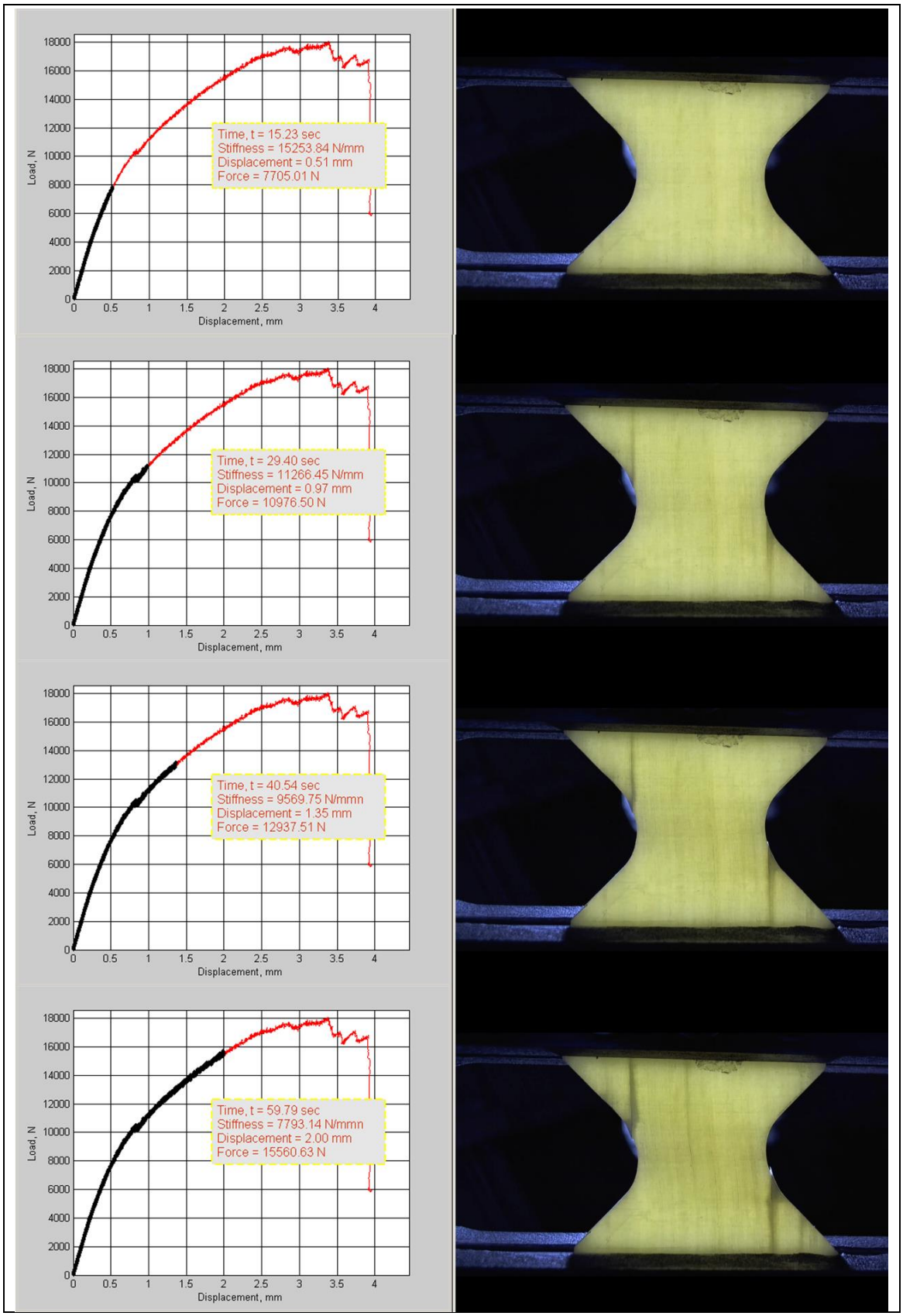
Load, N
Displacement, mm
Time, t = 15.23 sec
Stiffness = 15253.84 N/mm
Displacement = 0.51 mm
Force = 7705.01 N
Time, t = 29.40 sec
Stiffness = 11266.45 N/mm
Displacement = 0.97 mm
Force = 10976.50 N
Time, t = 40.54 sec
Stiffness = 9569.75 N/mmn
Displacement = 1.35 mm
Force = 12937.51 N
Time, t = 59.79 sec
Stiffness = 7793.14 N/mmn
Displacement = 2.00 mm
Force = 15560.63 N

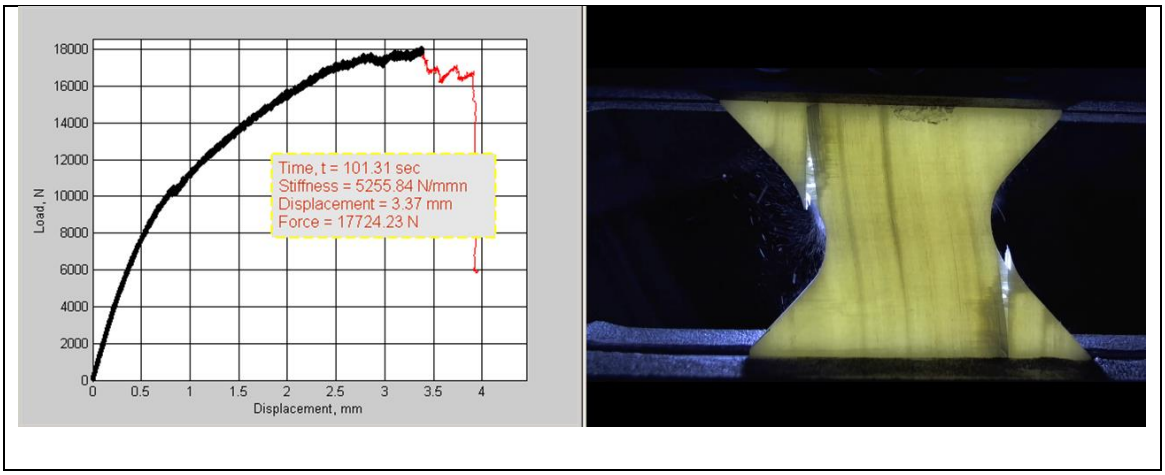

Figure 3-25: Damage development in small 1-2 Arcan specimen at 30° loading angle.

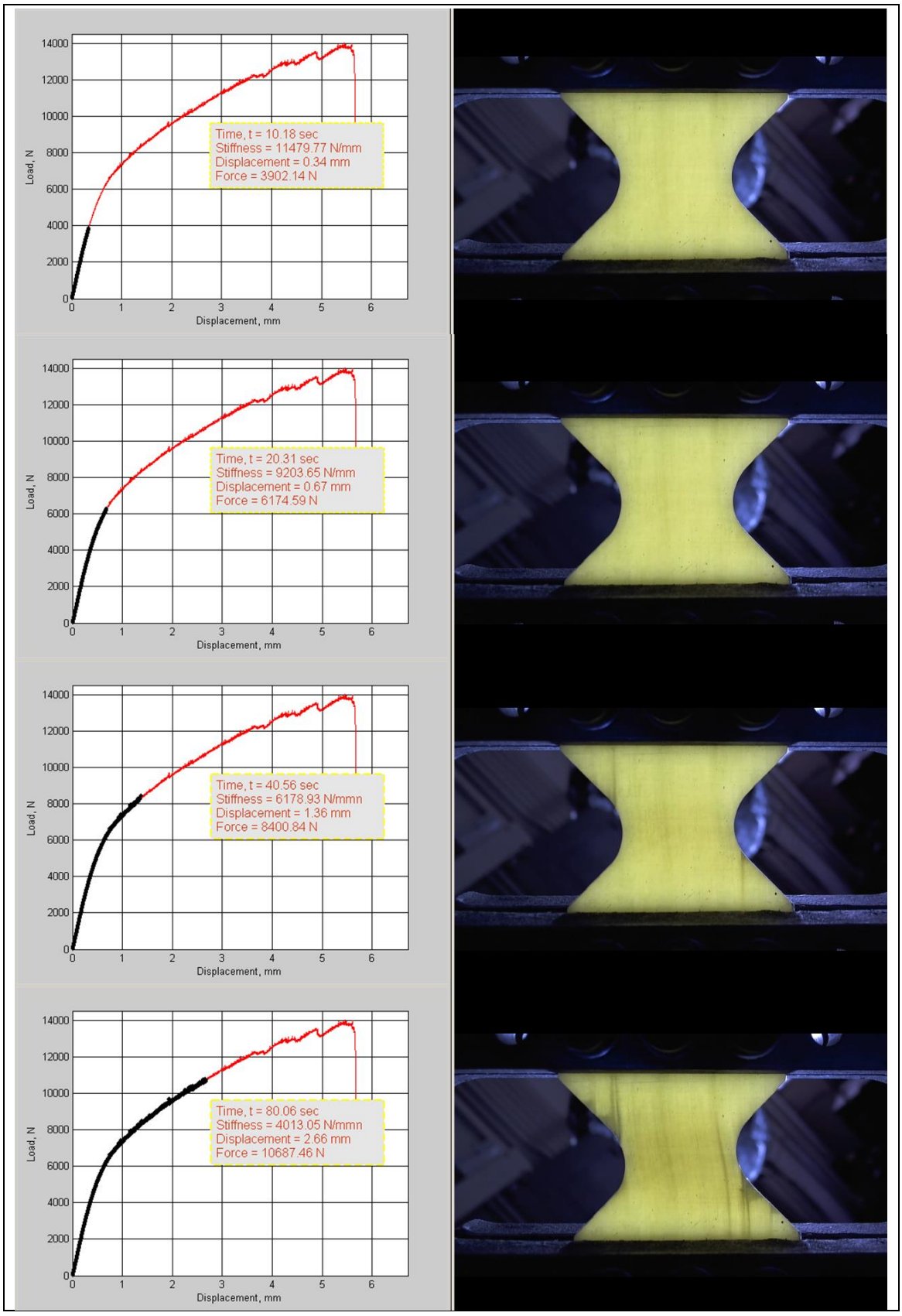
Load, N
Displacement, mm
Time, t = 10.18 sec
Stiffness = 11479.77 N/mm
Displacement = 0.34 mm
Force = 3902.14 N
Time, t = 20.31 sec
Stiffness = 9203.65 N/mm
Displacement = 0.67 mm
Force = 6174.59 N
Time, t = 40.56 sec
Stiffness = 6178.93 N/mmn
Displacement = 1.36 mm
Force = 8400.84 N
Time, t = 80.06 sec
Stiffness = 4013.05 N/mmn
Displacement = 2.66 mm
Force = 10687.46 N

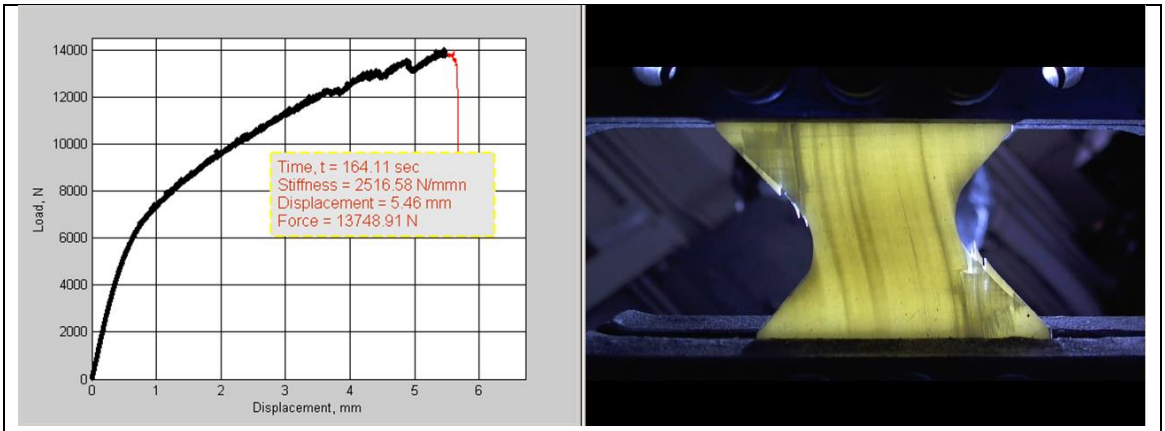

Figure 3-26: Damage development in small 1-2 Arcan specimen at 45° loading angle.

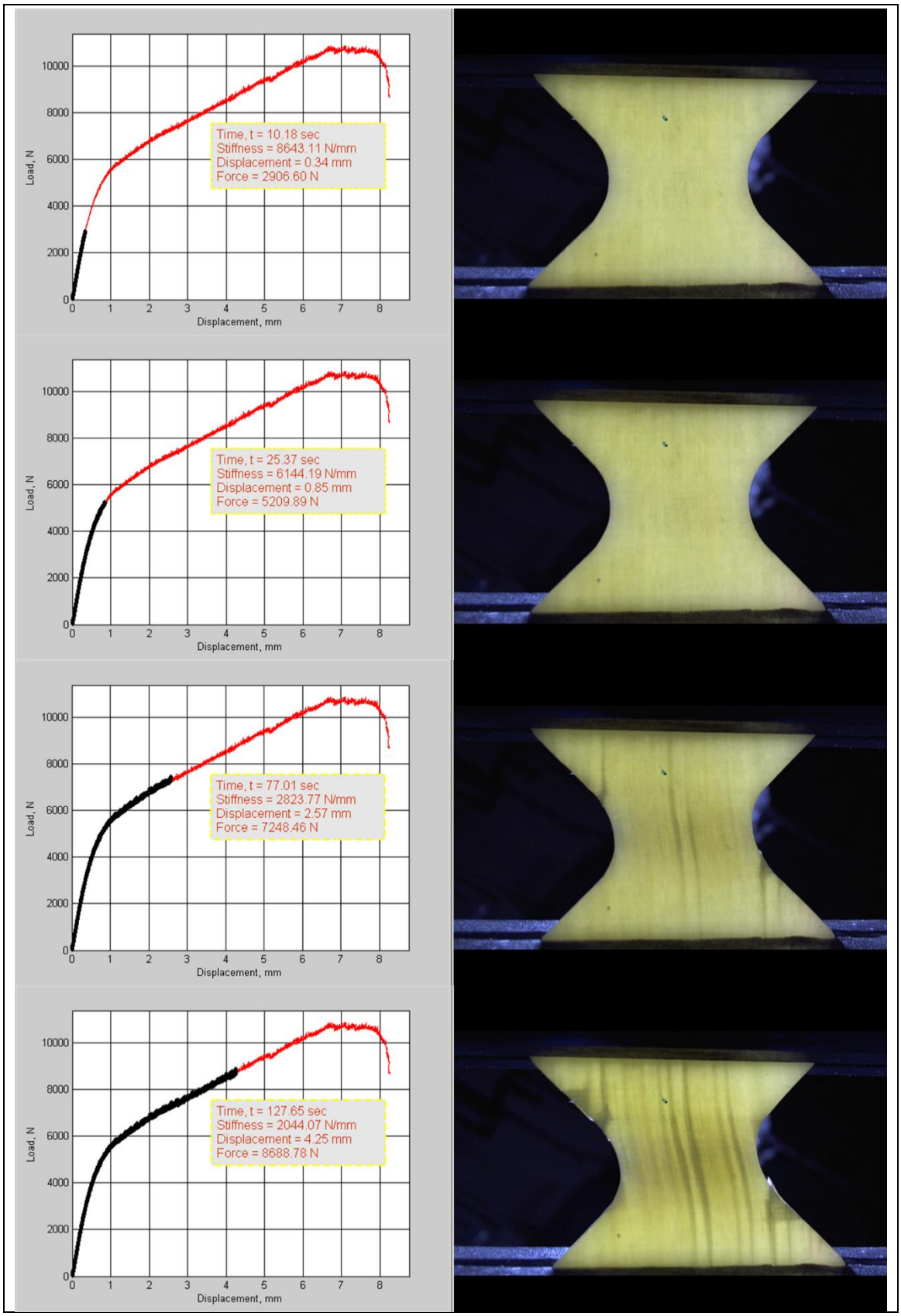
Load, N
Displacement, mm
Time, t = 10.18 sec
Stiffness = 8643.11 N/mm
Displacement = 0.34 mm
Force = 2906.60 N
Time, t = 25.37 sec
Stiffness = 6144.19 N/mm
Displacement = 0.85 mm
Force = 5209.89 N
Time, t = 77.01 sec
Stiffness = 2823.77 N/mm
Displacement = 2.57 mm
Force = 7248.46 N
Time, t = 127.65 sec
Stiffness = 2044.07 N/mm
Displacement = 4.25 mm
Force = 8688.78 N

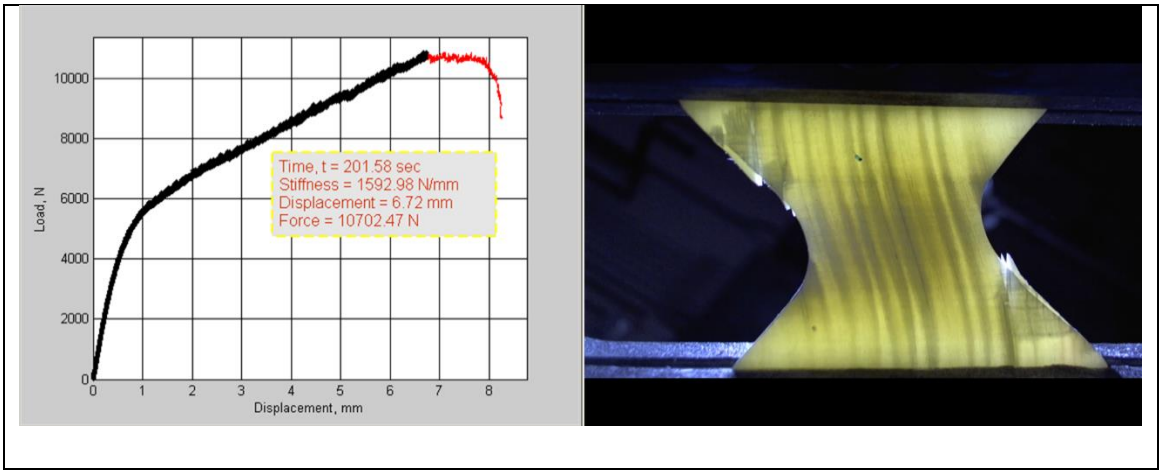

Figure 3-27: Damage development in small 1-2 Arcan specimen at 60° loading angle.

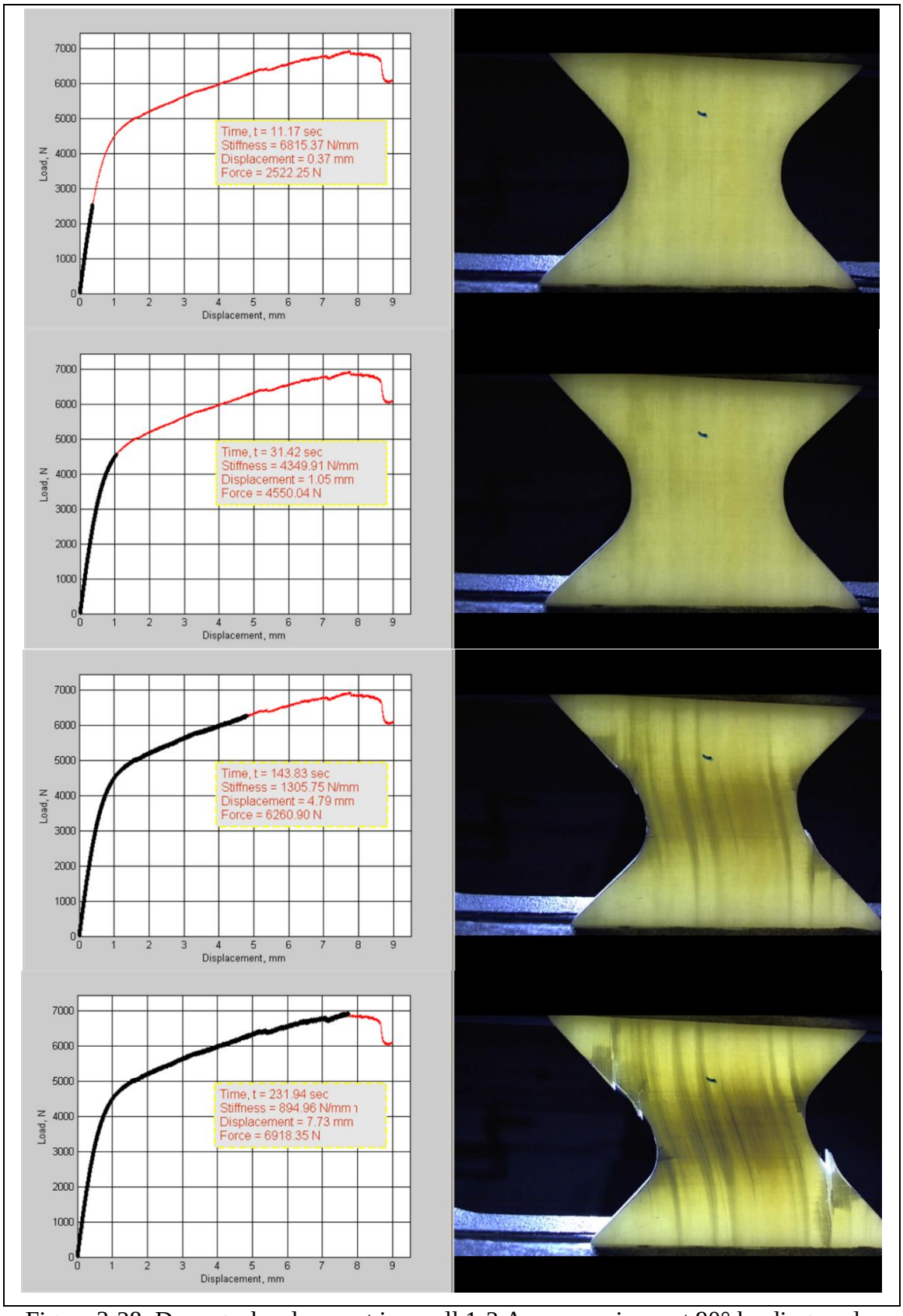

Figure 3-28: Damage development in small 1-2 Arcan specimen at 90° loading angle.

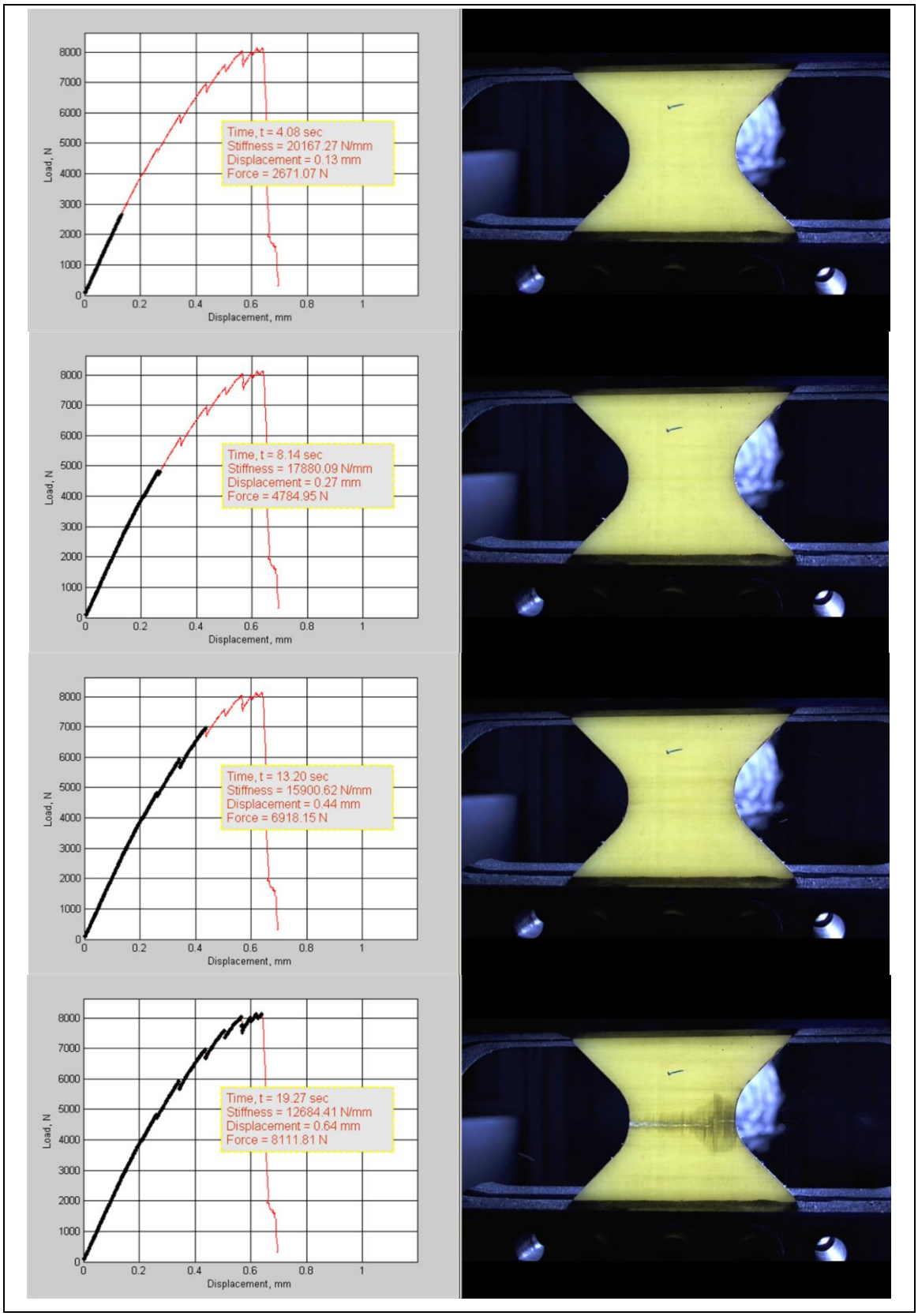

Figure 3-29: Damage development in small 2-1 Arcan specimen at 0° loading angle.

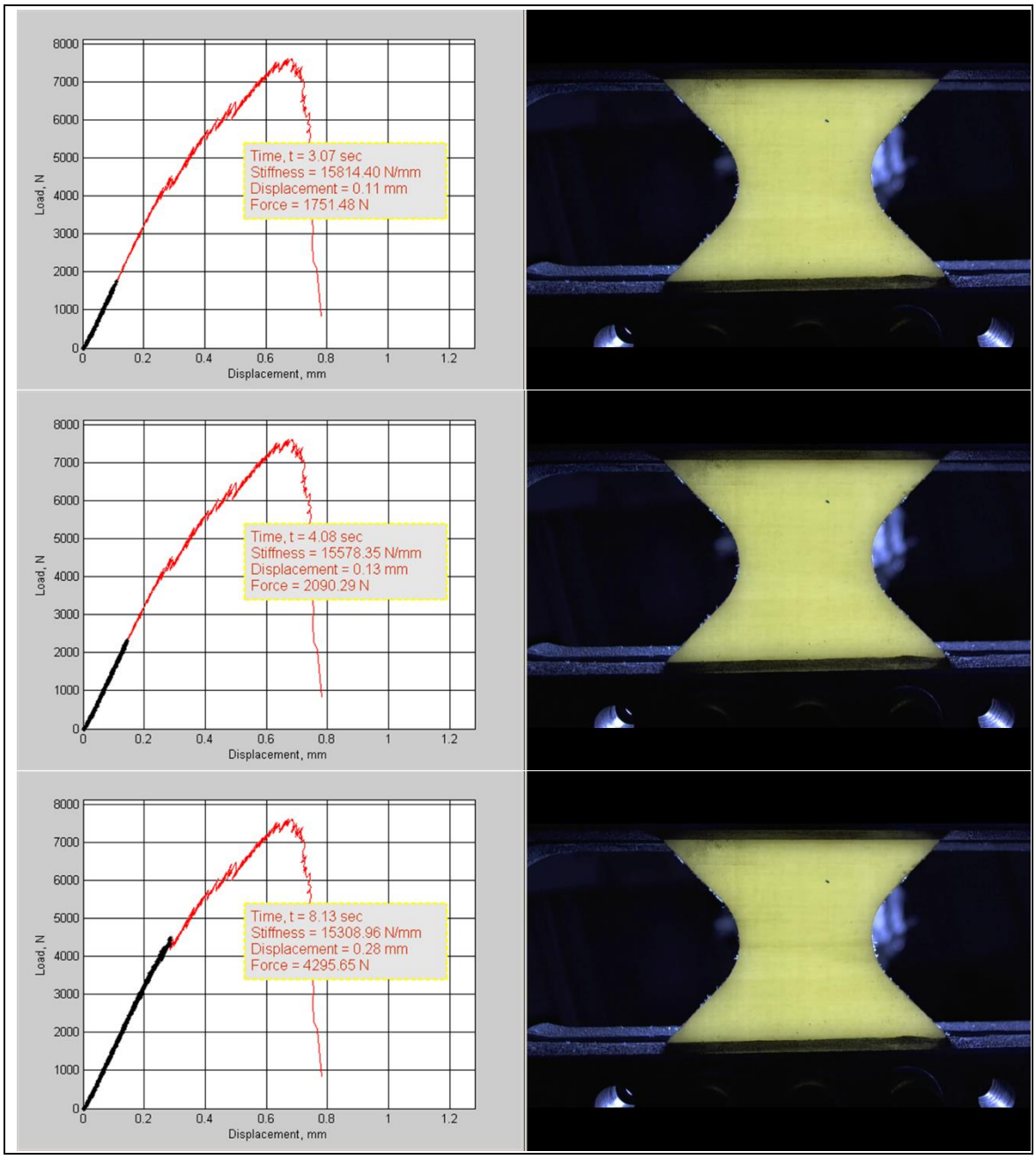
Load, N
Displacement, mm
Time, t = 3.07 sec
Stiffness = 15814.40 N/mm
Displacement = 0.11 mm
Force = 1751.48 N
Time, t = 4.08 sec
Stiffness = 15578.35 N/mm
Displacement = 0.13 mm
Force = 2090.29 N
Time, t = 8.13 sec
Stiffness = 15308.96 N/mm
Displacement = 0.28 mm
Force = 4295.65 N

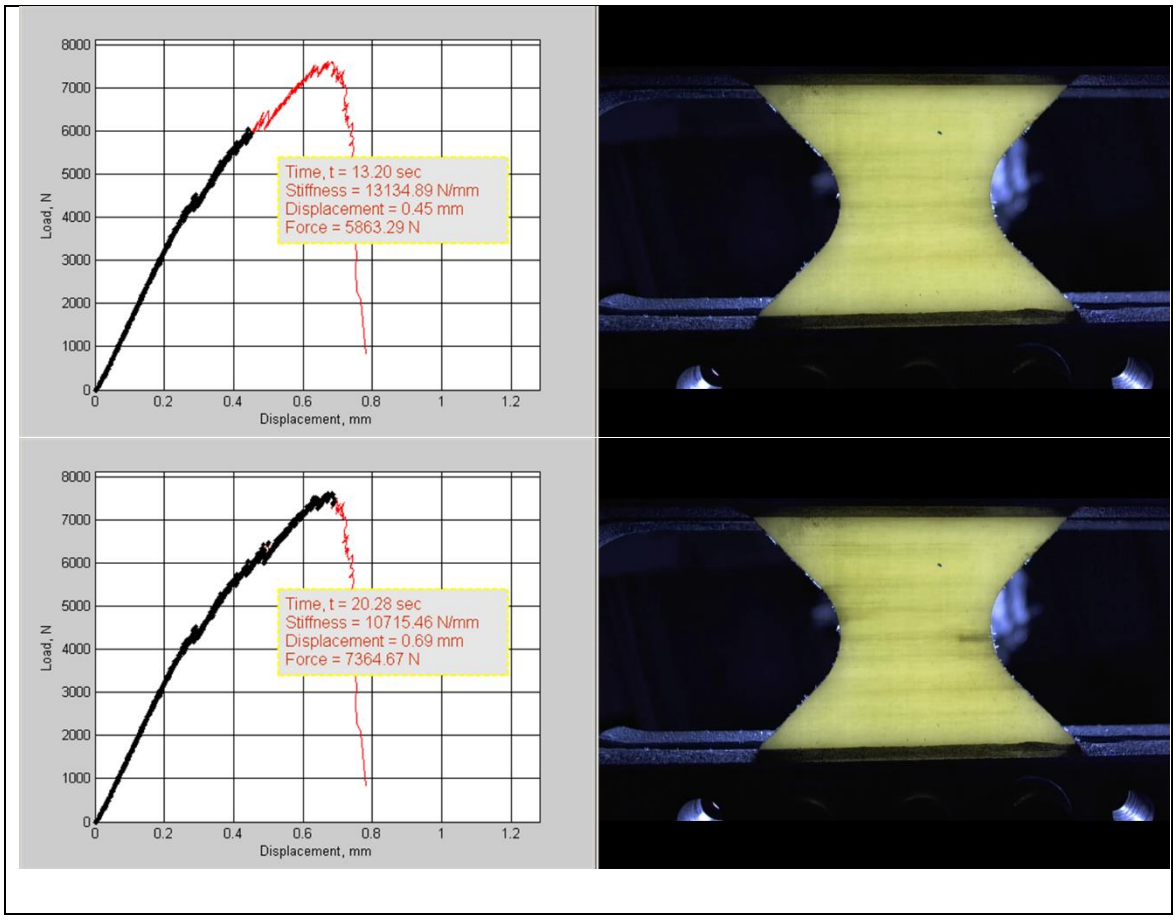

Figure 3-30: Damage development in small 2-1 Arcan specimen at 15° loading angle.

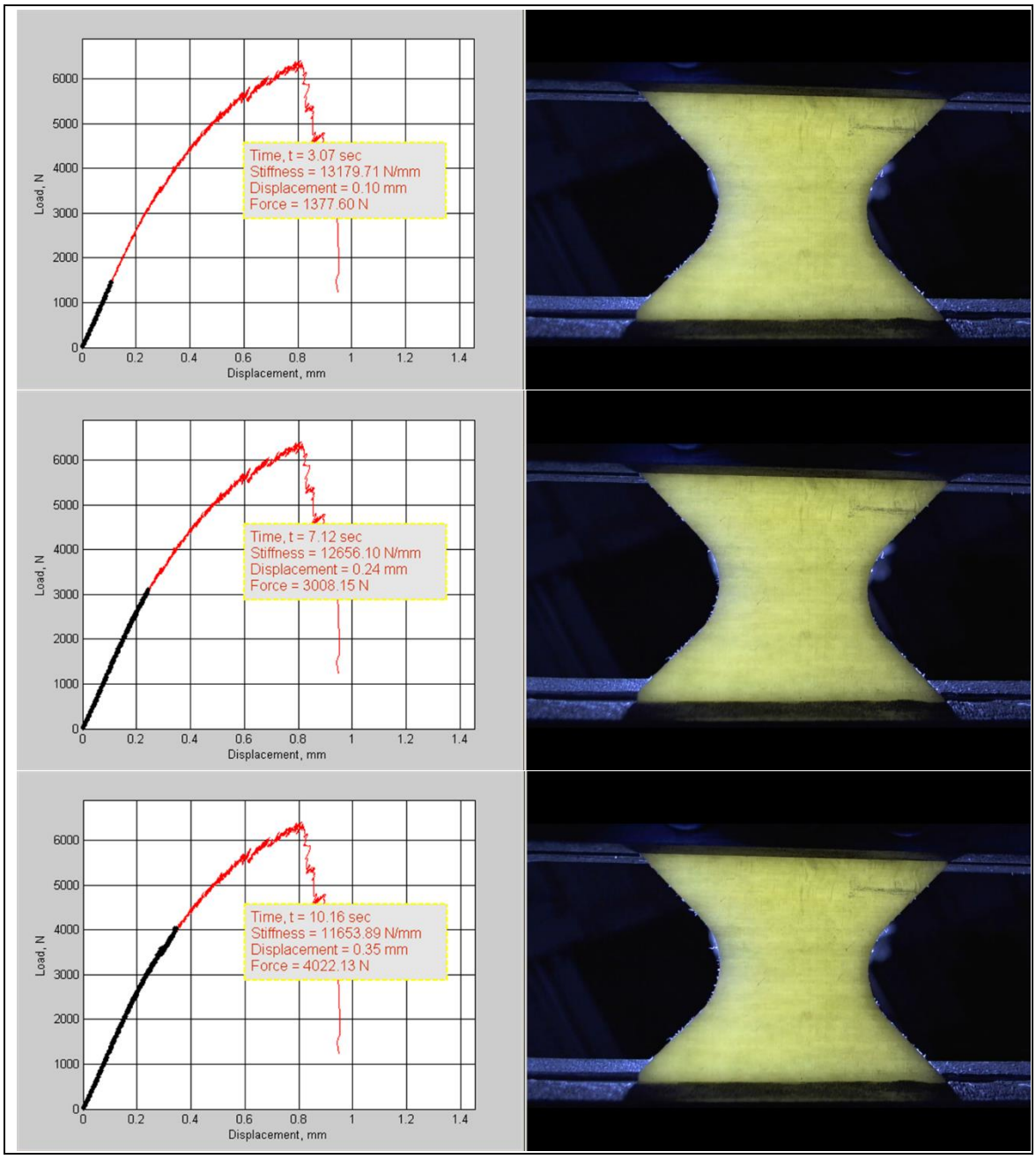
Load, N
Displacement, mm
Time, t = 3.07 sec
Stiffness = 13179.71 N/mm
Displacement = 0.10 mm
Force = 1377.60 N
Time, t = 7.12 sec
Stiffness = 12656.10 N/mm
Displacement = 0.24 mm
Force = 3008.15 N
Time, t = 10.16 sec
Stiffness = 11653.89 N/mm
Displacement = 0.35 mm
Force = 4022.13 N

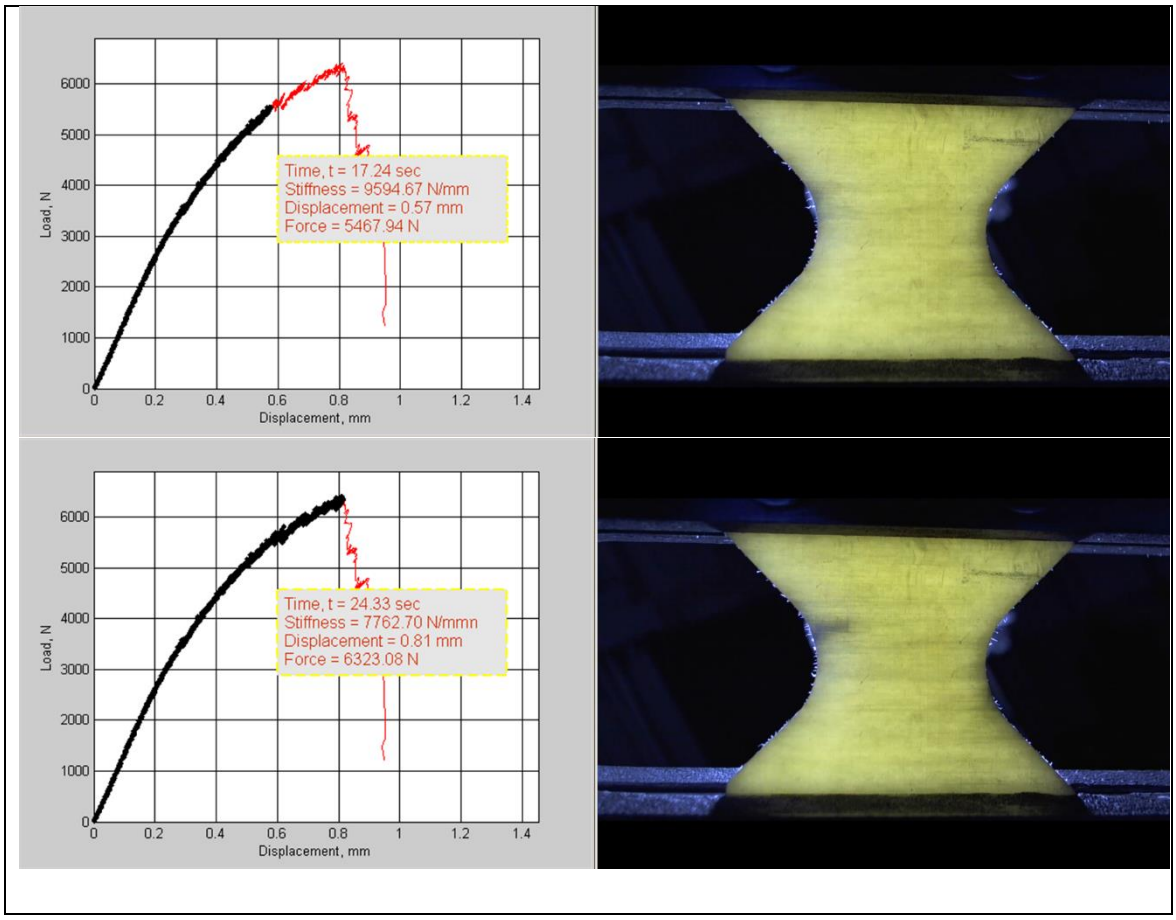

Figure 3-31: Damage development in small 2-1 Arcan specimen at 30° loading angle.

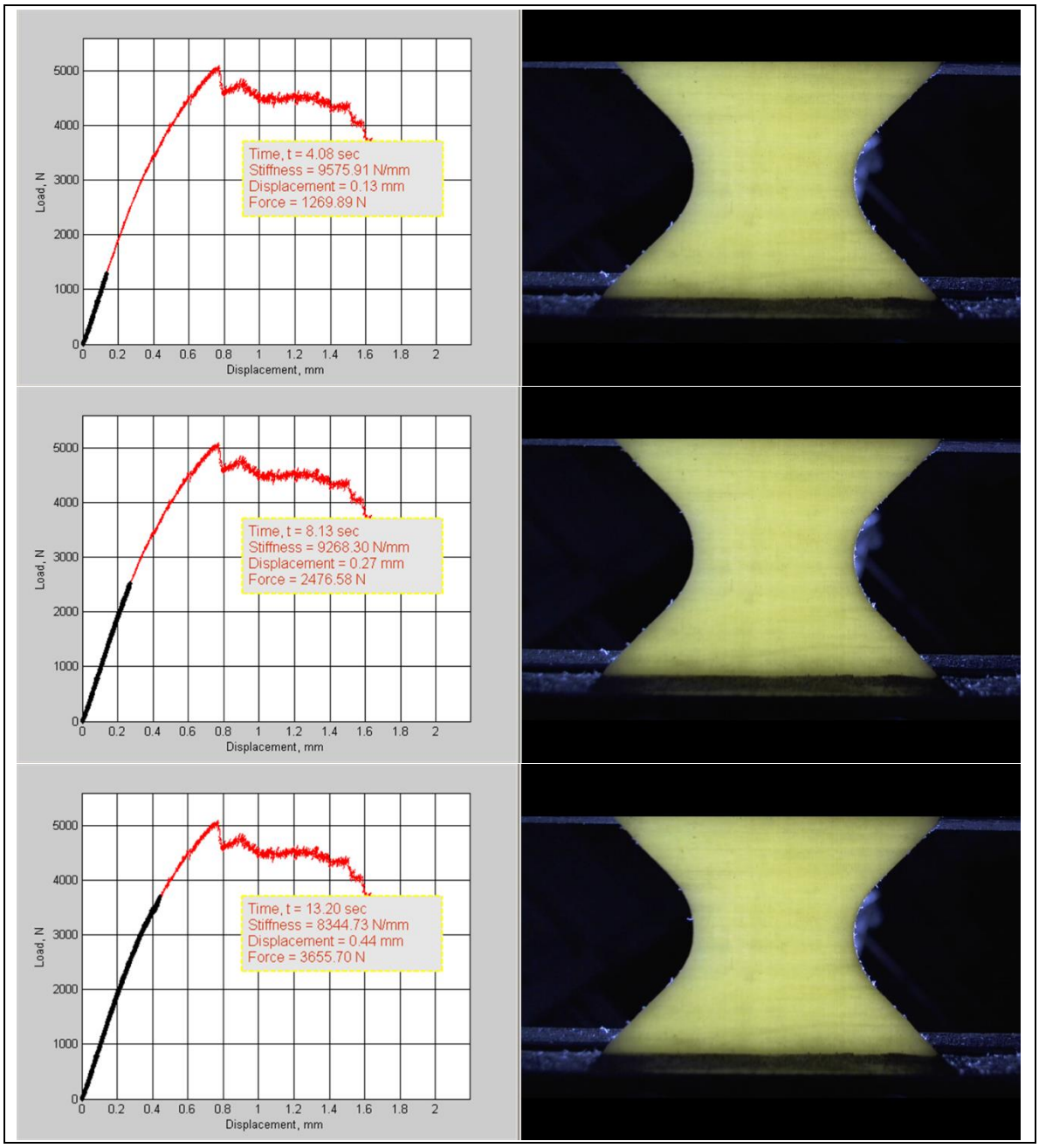
Load, N
Displacement, mm
Time, t = 4.08 sec
Stiffness = 9575.91 N/mm
Displacement = 0.13 mm
Force = 1269.89 N
Time, t = 8.13 sec
Stiffness = 9268.30 N/mm
Displacement = 0.27 mm
Force = 2476.58 N
Time, t = 13.20 sec
Stiffness = 8344.73 N/mm
Displacement = 0.44 mm
Force = 3655.70 N

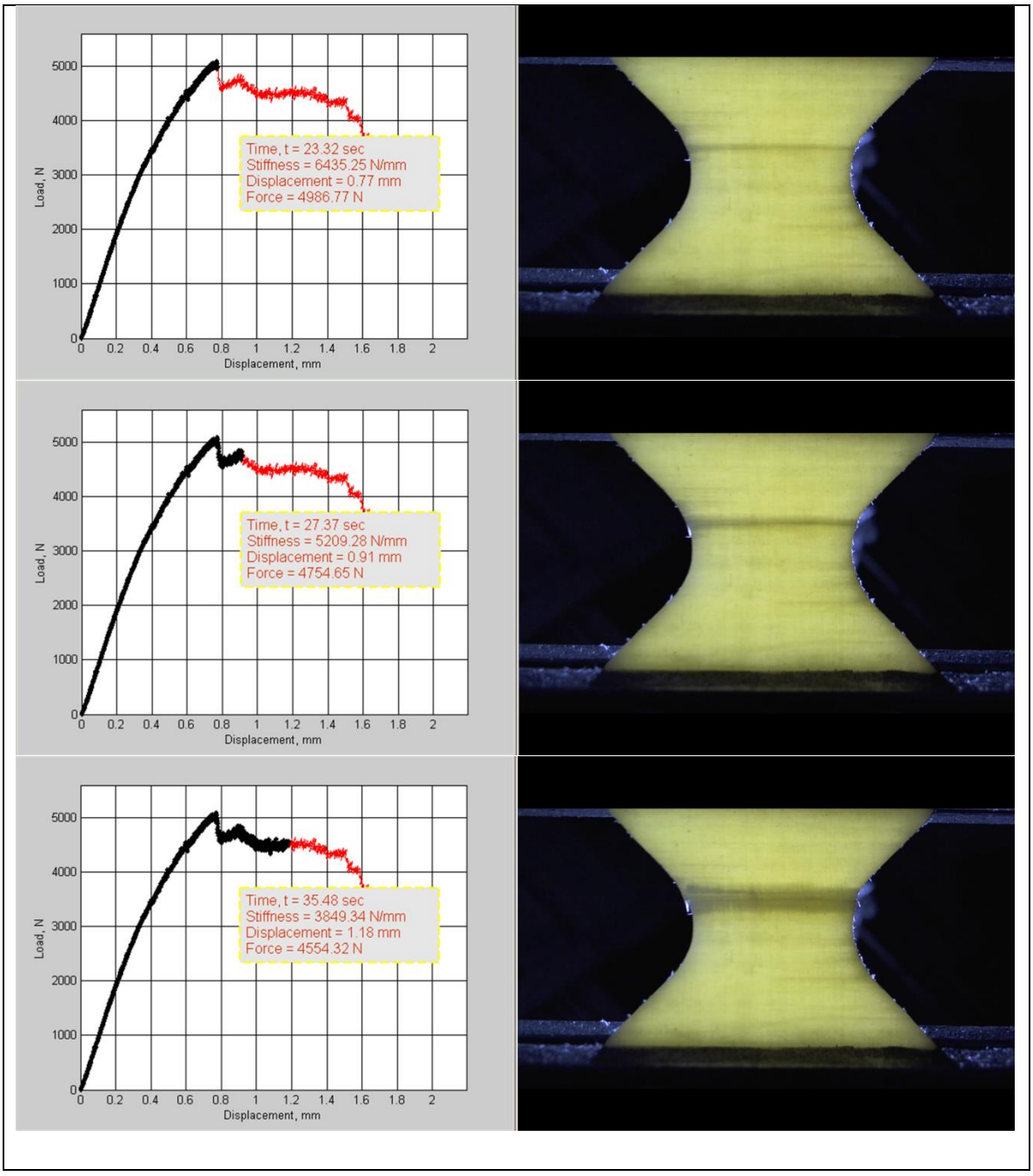

Figure 3-32: Damage development in small 2-1 Arcan specimen at 45° loading angle.

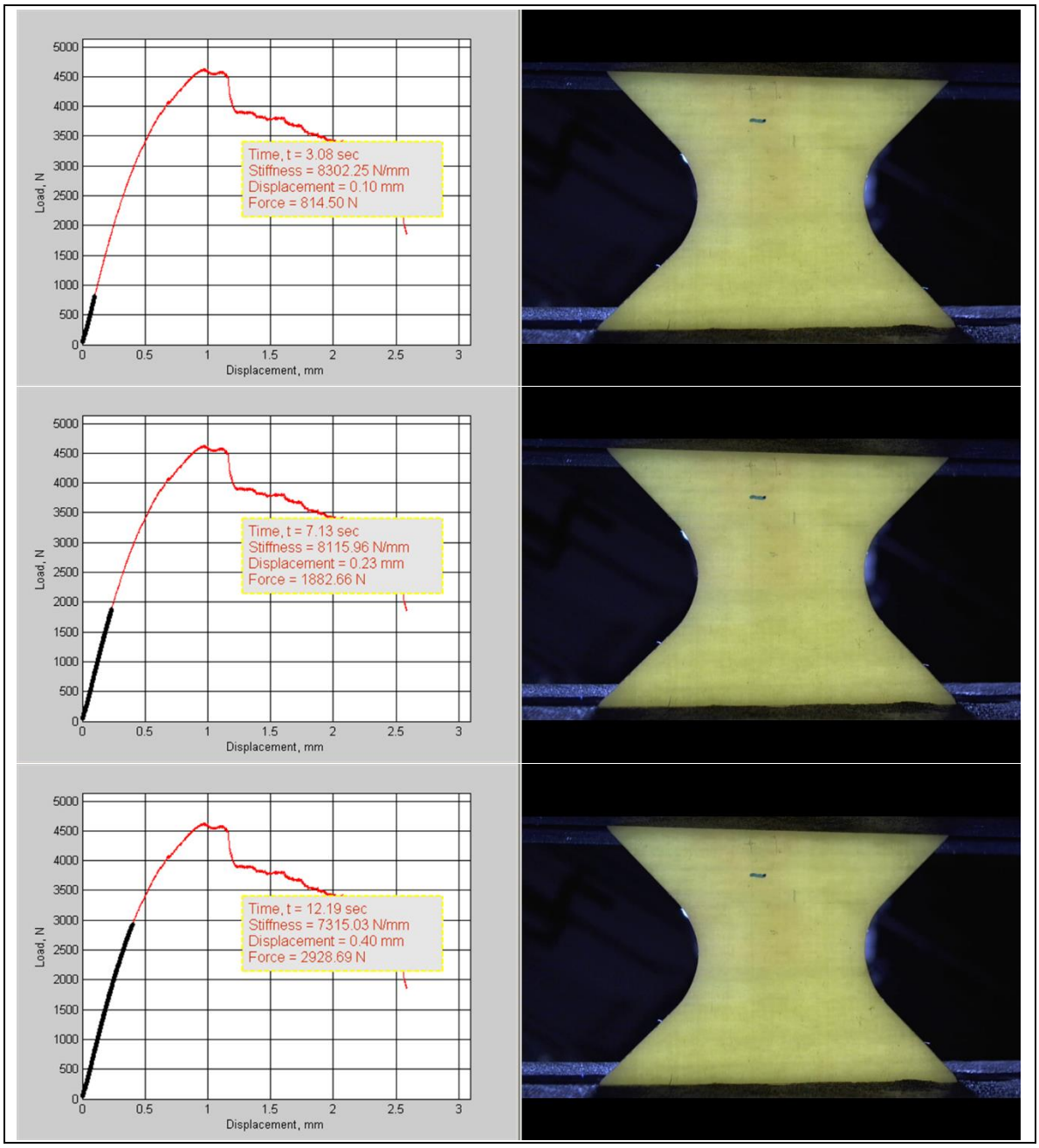
Load, N
Displacement, mm
Time, t = 3.08 sec
Stiffness = 8302.25 N/mm
Displacement = 0.10 mm
Force = 814.50 N
Time, t = 7.13 sec
Stiffness = 8115.96 N/mm
Displacement = 0.23 mm
Force = 1882.66 N
Time, t = 12.19 sec
Stiffness = 7315.03 N/mm
Displacement = 0.40 mm
Force = 2928.69 N

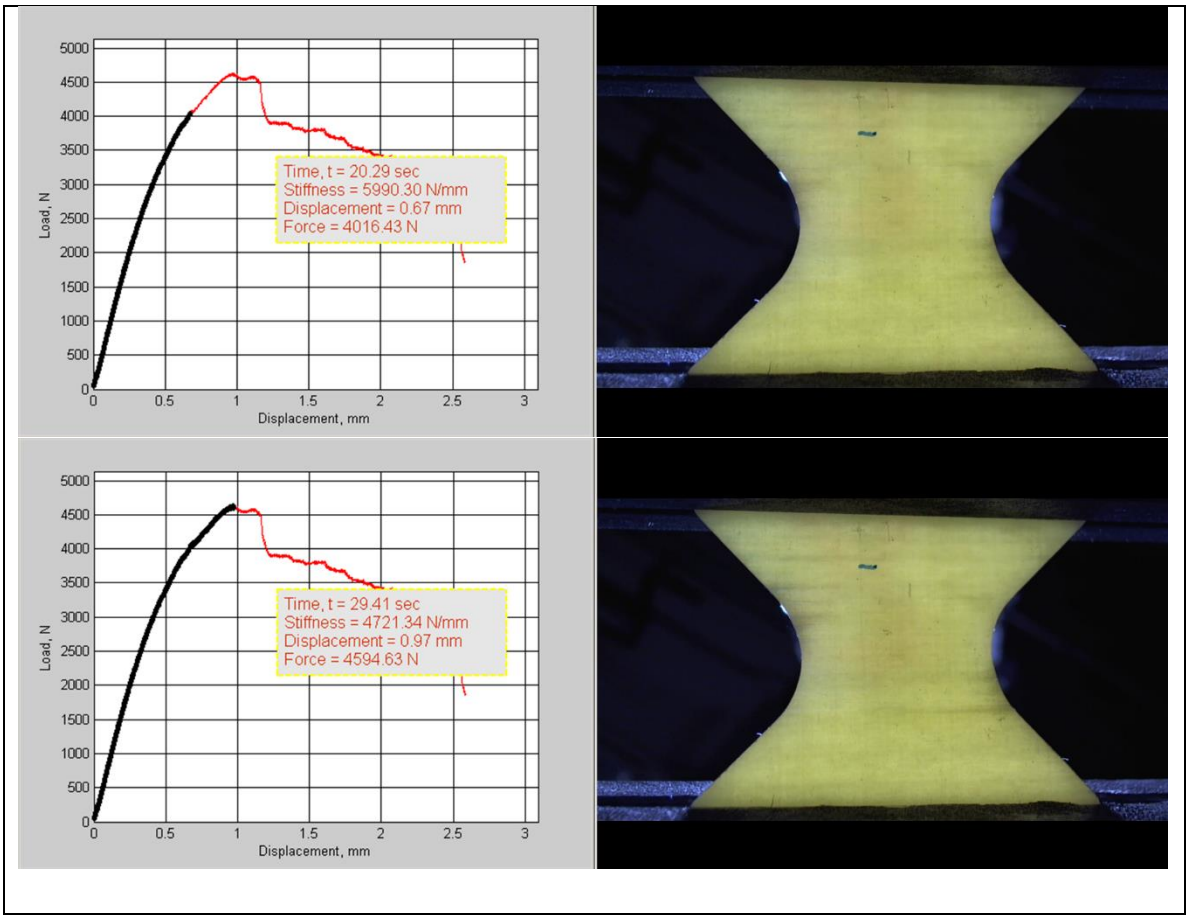

Figure 3-33: Damage development in small 2-1 Arcan specimen at 60° loading angle.

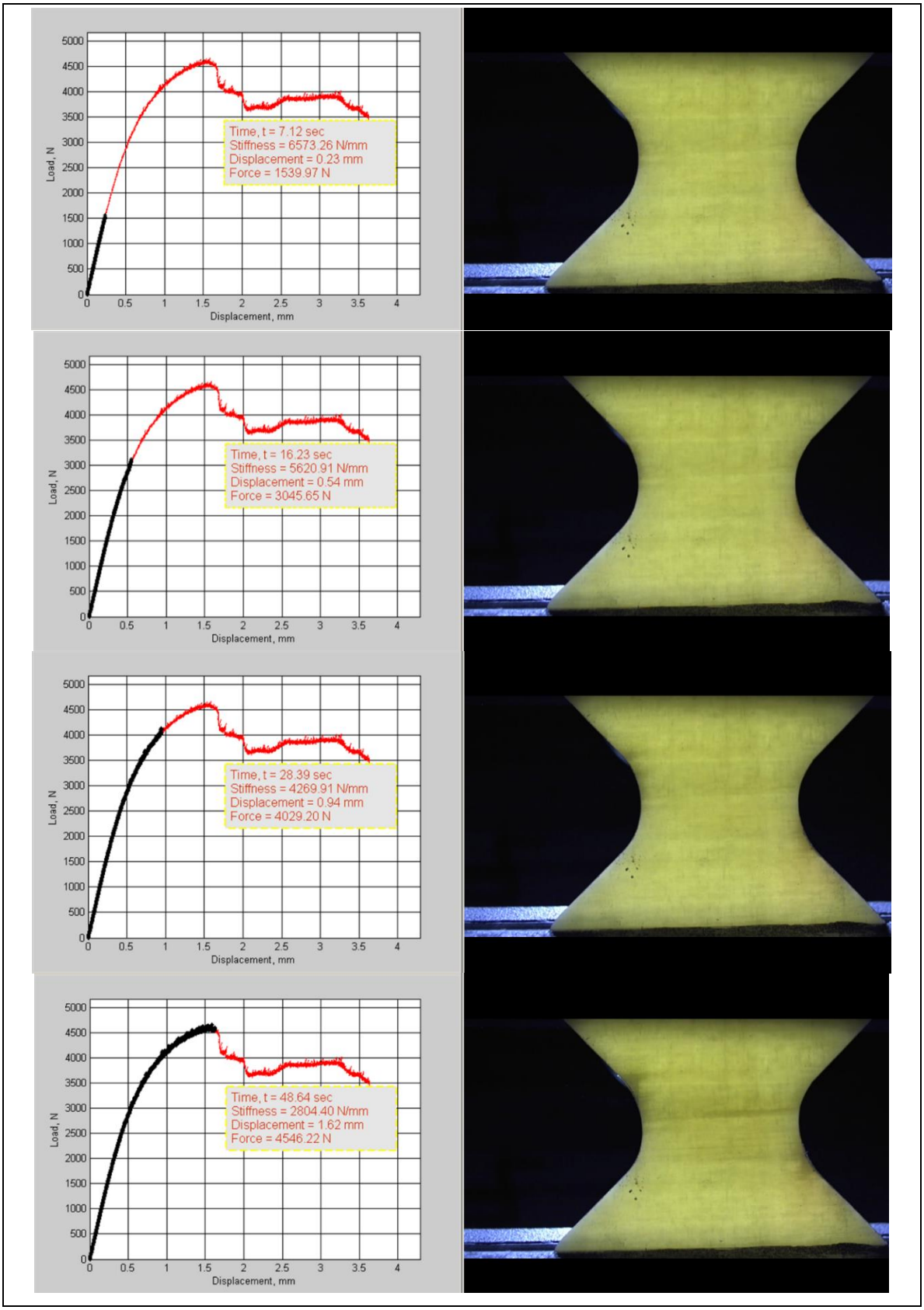

Figure 3-34: Damage development in small 2-1 Arcan specimen at 90° loading angle.

Figure 3-35 and Figure 3-36 show the final failure surfaces of small 1-2 and 2-1 Arcan specimens loaded at α = 30°, 45°, 60° and 90°, respectively. It is seen that all the 1-2 specimens failed primarily due to a combination of shear buckling and delamination. Furthermore, the amount of delamination increased as the loading angle increased. The 2-1 specimens at lower loading angles (30° and 45°) failed due to matrix cracking. At higher loading angles (60° and 90°), the final failure due to a combination matrix cracking and delamination.

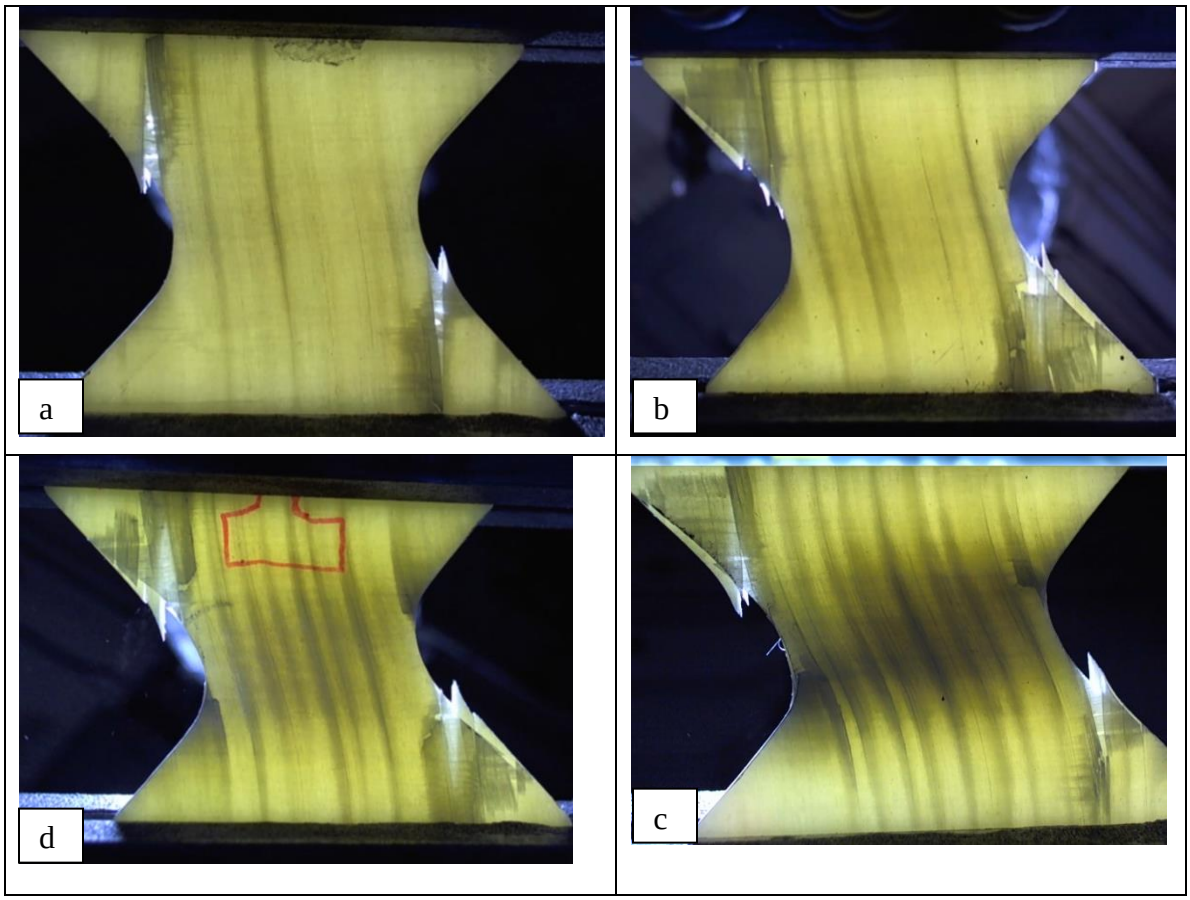

Figure 3-35: Damage development in small 1-2 Arcan specimens at 30° (a), 45° (b), 60° (c) and 90° loading angle (d).

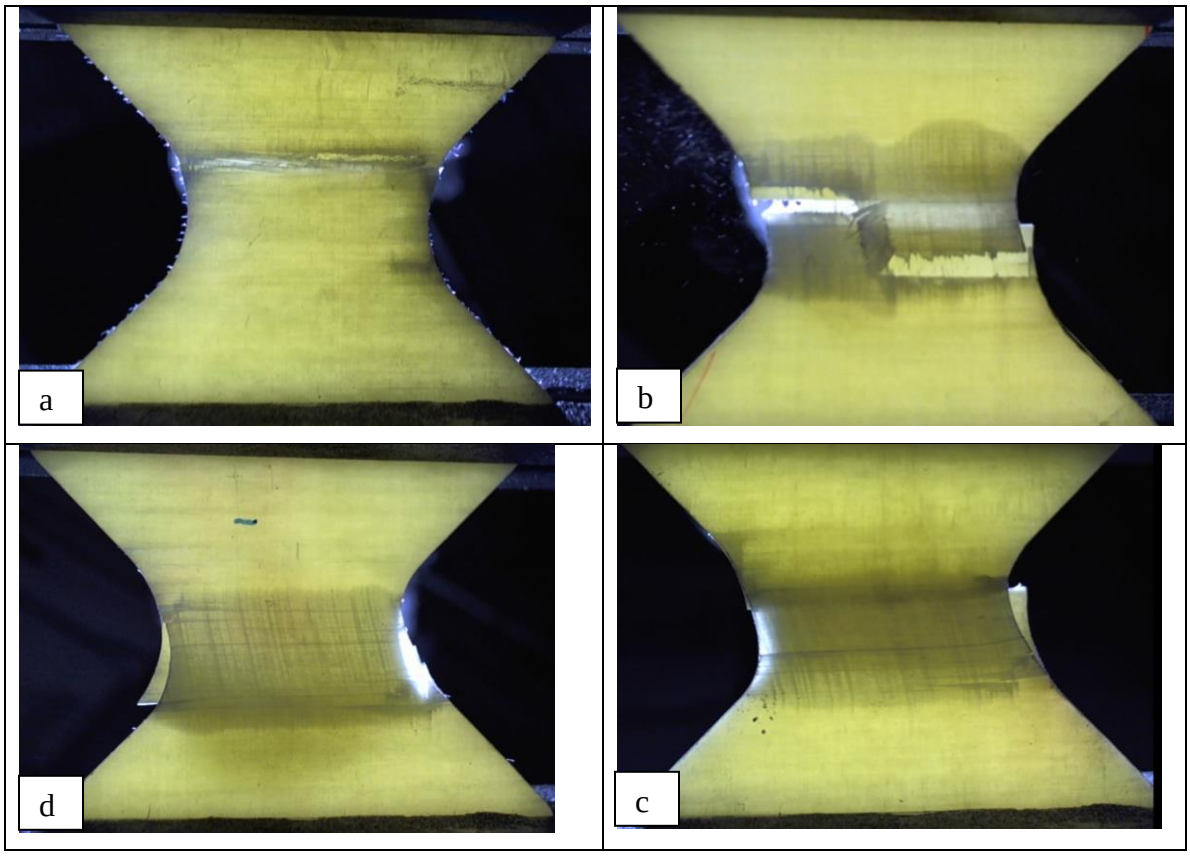

Figure 3-36: Damage development in small 2-1 Arcan specimens at (a) 30^{o} (b) 45°, (c) 60° and (d) 90° loading angles.

3.4 Failure Envelopes in Monotonic Loading based on the Peak Loads

Figure 3-37 and Figure 3-38 show the failure envelopes of 1-2 and 2-1 specimens based on the peak load. In each figure, the normal stress component of the peak load is plotted against the shear stress component of the peak load for both small and large specimens. The vertical axis corresponds to loading angle 90^{o} and the horizontal axis corresponds to loading angle 0^{o}. The stress components corresponding to the peak loads (Tables 3-2 and 3-3 for large specimens and Tables 3-5 and 3-6 for small specimens) were calculated using the area of the significant section. Each data point on these figures represents the average peak stress components as the loading angle was changed from 0^{o} to 90^{o}. It can be observed in both figures that the failure envelopes for small and large

specimens are very close to each other for both 1-2 and 2-1 specimens. For the 1-2 specimens, the failure envelope first increased as the loading mode changed from shear (at loading angle = 90°) to a combination of shear and tensile normal stress for loading angles between 90 and 45°, and then decreased as the loading angle became smaller than 45°. For the 2-1 specimens, the failure envelope decreased as the loading mode changed from shear to a combination of shear and tensile normal stress. Thus, the failure envelopes based on peak loads in monotonic loading were different for the 1-2 specimens containing mostly 0° layers and 2-1 specimens containing mostly 90° layers.

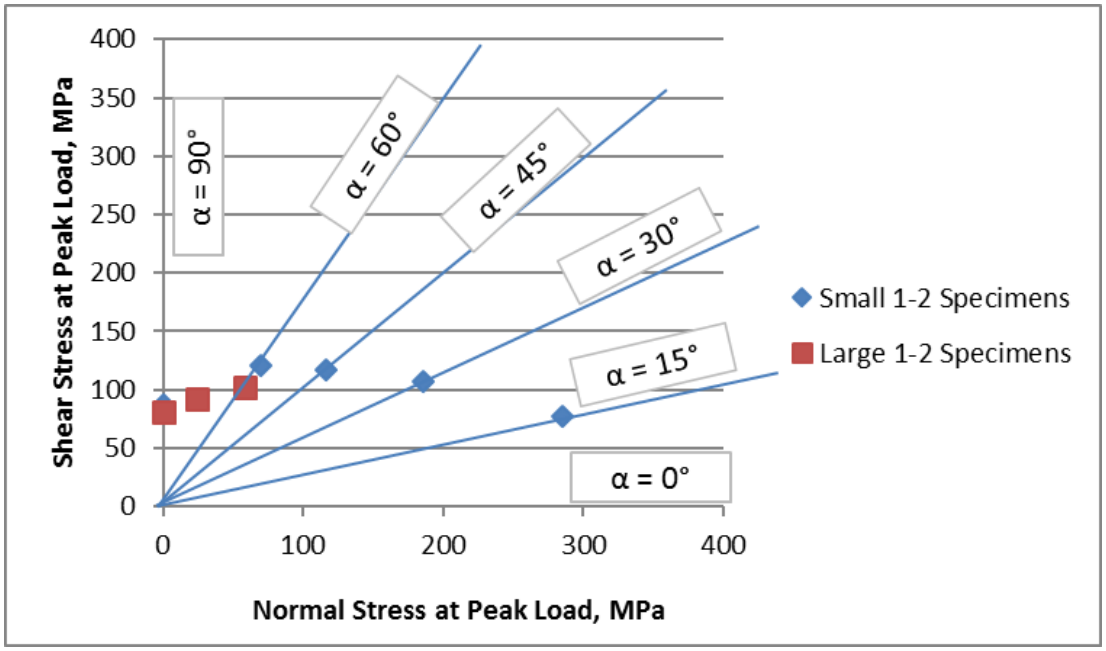

Figure 3-37: Failure envelope for 1-2 specimens based on peak loads.

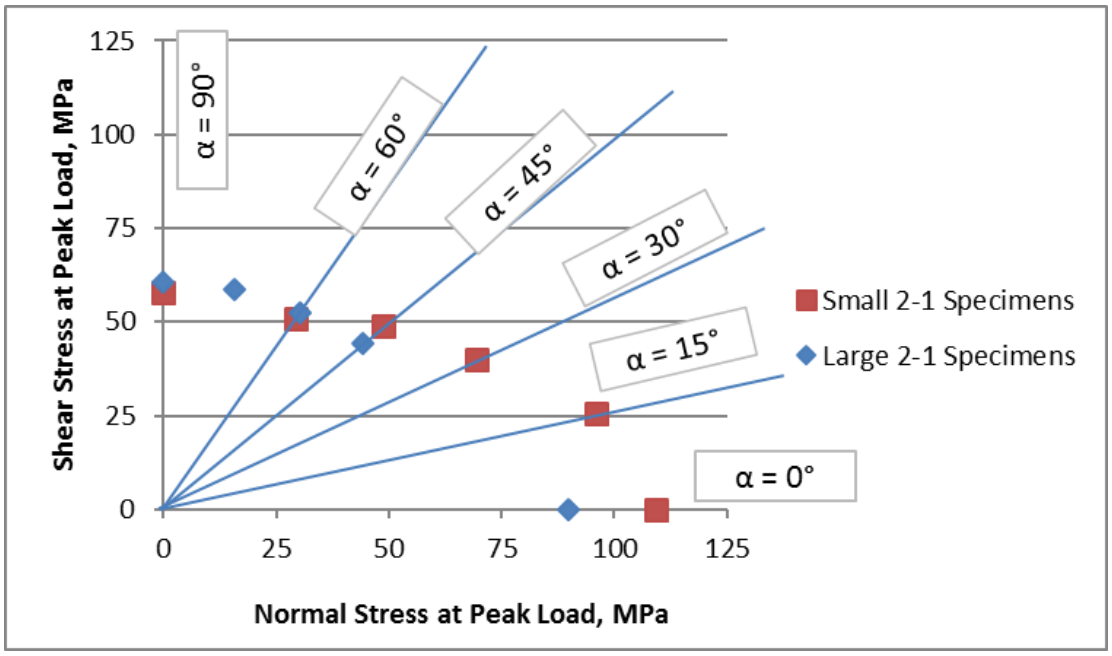

Figure 3-38: Failure envelope for 2-1 specimens based on peak loads.

3.5 Failure Envelopes in Monotonic Loading based on the Knee Loads

Figure 3-39 shows the failure envelopes of both small 1-2 and 2-1 specimens based on the knee load. The stress values used for the envelopes are the same used for Figure 3-37 and 3-38. It is seen that the failure envelopes for both 1-2 and 2-1 specimens are similar. This is primarily because of the fact that the peak stress envelopes are largely independent of the longitudinal and transverse tensile strength of the material. From Figure 3-39 it is seen that the knee load of both 1-2 and 2-1 specimens is similar at 90° loading angle but the difference between the knee loads increases as the normal stress increases.

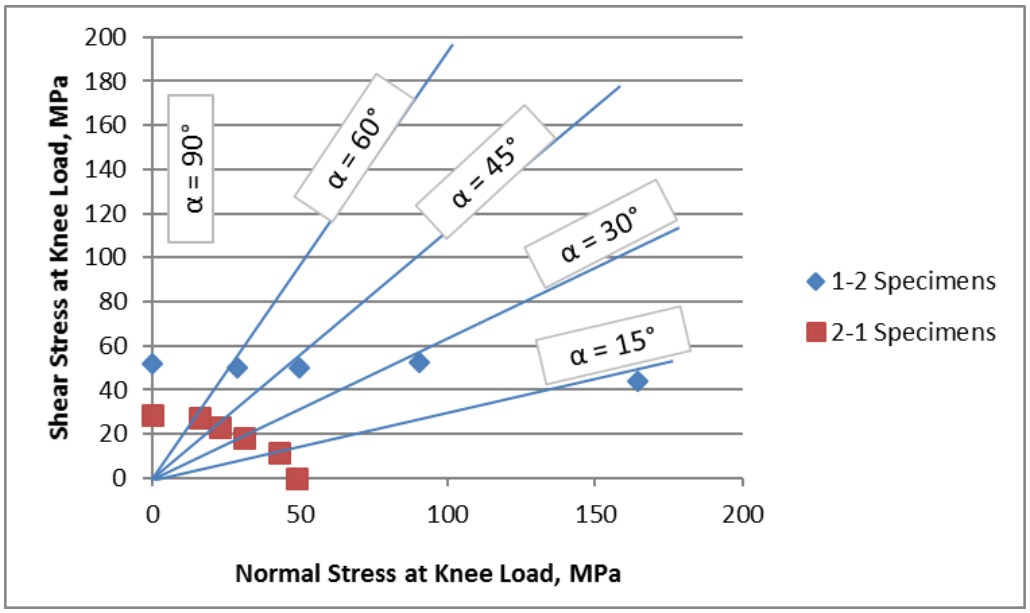

Figure 3-39: Comparison of knee stresses of small 1-2 and 2-1 Arcan specimen based on knee loads.

Azzi-Tsai-Hill failure criteria [7], described by Equation 3.5, was used to generate theoretical knee stress envelopes for both 1-2 and 2-1 small Arcan specimens using strength values listed in Table 3-8. Figure 3-40 and Figure 3-41 show the failure envelopes of 1-2 and 2-1 specimens. Shear strengths for both 1-2 and 2-1 specimens are the average experimental values corresponding to the knee load for shear loaded specimens. Similarly, transverse tensile strength at knee is the average experimental stress value corresponding to the knee load observed in the tensile loaded 2-1 specimens at a 0^o loading angle. Since no experiments were performed on the 1-2 specimens at 0^o loading angle, the tensile strength at knee, X, was estimated using the test data from 1-2 specimens loaded at 15° loading angle in Equation (3.5).

$$\left(\frac{\sigma_{11}}{X}\right)^2 - \left(\frac{\sigma_{11}}{X}\right)\left(\frac{\sigma_{22}}{Y}\right) + \left(\frac{\tau_{12}}{S}\right)^2 = 1 \tag{3.5}$$

where,

$\sigma_{11} =$ axial stress
$\sigma_{22} =$ transverse stress
$\tau_{12} =$ shear stress

$X =$ axial tensile strength at knee
$Y =$ transverse tensile strength at knee
$S =$ shear strength at knee

Table 3-8: Knee-load based failure envelope parameters used for 1-2 and 2-1 specimens.

Specimen Type	Strength Parameter	Value (MPa)	Comment
1-2	X	316	Estimated
1-2	S	51.54	Experimental Value at α = 90°
2-1	Y	48.69	Experimental Value at α = 0°
2-1	S	28.83	Experimental Value at α = 90°

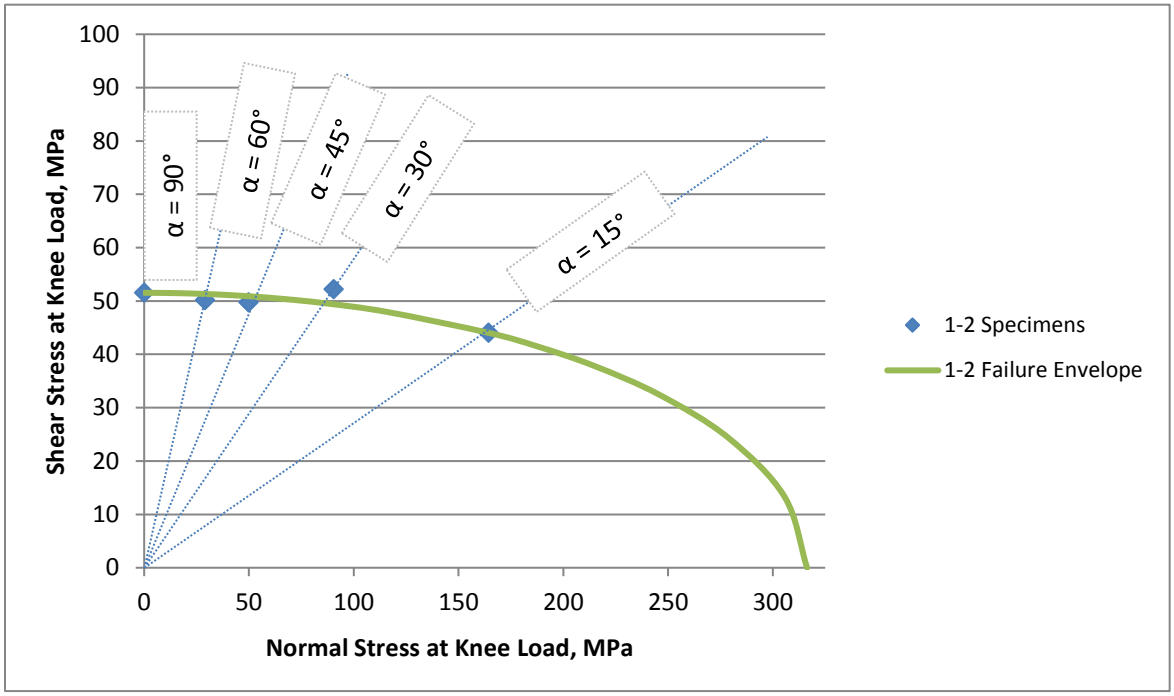

Figure 3-40: Failure envelope for small 1-2 Arcan specimens based on knee loads.

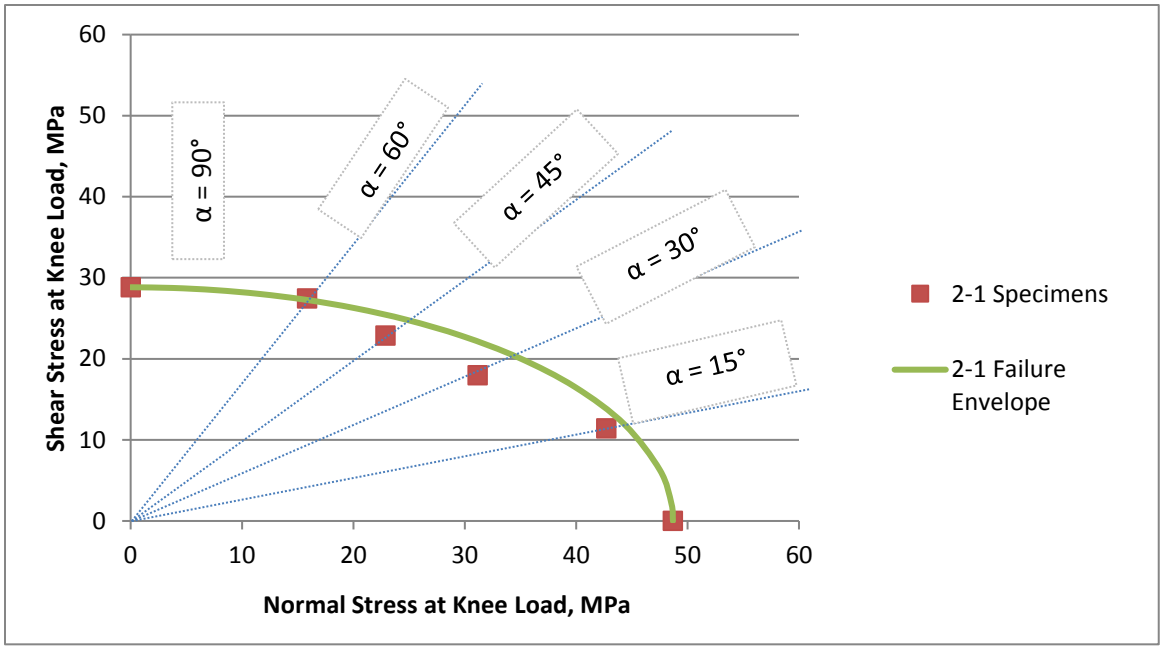

Figure 3-41: Failure envelope for small 2-1 Arcan specimens based on knee loads.

It can be observed in Figure 3-40 and Figure 3-41 that the theoretical failure envelopes based on Azzi-Tsai-Hill theory fit very well with the experimental data for both 1-2 and 2-1 specimens.

3.6 Conclusion

This study has shown the validity of using Arcan specimen to determine the quasi-static characteristics of composite laminates under a combination of tensile normal stress and shear stress. The material used in the study was an E-glass fiber reinforced epoxy and the laminate configuration was $[0/90/0_9/90/0]$. The same test method can be applied to other laminates and can also be developed to characterize composite laminates under a combination of compressive normal stress and shear stress. Unlike the tubular specimens commonly used for characterizing biaxial strength properties, the Arcan test specimens can be used for flat laminates. The Arcan test fixture is relatively simple and the Arcan test arrangement can be easily fitted in universal testing machines used for mechanical characterization of materials. It can be used to generate a wide range of biaxial normal stresses and in-plane shear stress, which makes it a very versatile test method for composite materials.

It is shown in this chapter that the failure strengths at knee of [0/90/0_9/90/0] laminates under combined tensile normal stress and shear stress fits a quadratic envelope. The load-displacement diagrams exhibit a knee at which failure initiation occurs. Above the knee load, the load-displacement diagrams become increasingly non-linear as the shear stress component increases. The knee and failure loads in the 2-1 configuration are lower than in the 1-2 configuration. The normal stress component at both knee and failure load increases as the shear stress component is decreased. Failure of the 2-1 specimens is due to shear cracking in the significant section, while failure of the 1-2 specimens is a combination of matrix cracking and shear buckling. The Azz-Tsai-Hill theory fits very well with the experimental failure envelope corresponding to the knee load.

3.7 References

[1] A. Chen and F. Matthews, "A review of multiaxial/biaxial loading tests for composite materials," *Composites*, vol. 24, no. 5, pp. 395–406, Jul. 1993.

[2] R. Olsson, "A survey of test methods for multiaxial and out-of-plane strength of composite laminates," *Composites Science and Technology*, vol. 71, no. 6, pp. 773–783, Apr. 2011.

[3] M. Arcan, Z. Hashin, and A. Voloshin, "A method to produce uniform plane-stress states with applications to fiber-reinforced materials," *Experimental Mechanics*, vol. 18, no. 4, pp. 141–146, Apr. 1978.

[4] A. Voloshin and M. Arcan, "Failure of unidirectional fiber-reinforced materials—New methodology and results," *Experimental Mechanics*, vol. 20, no. 8, pp. 280–284, Aug. 1980.

[5] A. Voloshin and M. Arcan, "Pure shear moduli of unidirectional fibre-reinforced materials (FRM)," *Fibre Science and Technology*, vol. 13, no. 2, pp. 125–134, Mar. 1980.

[6] P. B. Gning, D. Delsart, J. M. Mortier, and D. Coutellier, "Through-thickness strength measurements using Arcan's method," *Composites Part B: Engineering*, vol. 41, no. 4, pp. 308–316, Jun. 2010.

[7] P. K. Mallick, *Fiber-Reinforced Composites: Materials, Manufacturing, and Design*, 3rd ed., [Expanded and Ed.]. Boca Raton FL: CRC Press, 2008.

CHAPTER 4 : FATIGUE BEHAVIOR OF COMPOSITE LAMINATES UNDER BIAXIAL STRESSES

4.1 Introduction

The principal objective of the current research is to develop the Arcan test method for determining biaxial fatigue behavior of flat composite laminates under combined normal and shear loads. In the published literature on biaxial fatigue tests of polymer matrix composites [1]–[6] three types of specimens were used: a) flat tensile specimen under off-axis tensile loading [7]–[16] b) cruciform specimens [17], [18] under biaxial tensile loading, and c) tubular specimens [19]–[23] under combined tensile and torsional or compressive and torsional loading. The shortcomings of these three types of specimens are described in Chapter 1. The majority of the biaxial fatigue data were generated using tubular specimens. Although both normal and shear loads can be applied on tubular specimens, the specimen design itself poses a number of challenges. They need to be thin enough to prevent through-the-thickness strain variations and thick enough to prevent torsional buckling. Furthermore, special tools are required to manufacture tubular specimens. Since vast majority of polymer matrix composites are used in plate or panel form, it is important to develop biaxial test method for flat specimens.

This chapter describes the biaxial fatigue response of an E-glass reinforced epoxy [0/90/0_9/90/0] composite laminate determined by using Arcan test specimen under combinations of normal and shear loads. The test specimen development is described in Chapters 2 and 3. Monotonic biaxial tests were conducted with both small and large Arcan specimens in Chapter 3. Biaxial fatigue tests were conducted with small Arcan specimens. In these tests, the load applied on the yokes of the Arcan test fixture was cycled to create cyclic normal and shear loads. The specimen experienced only normal load at 0^o loading angle, and only shear load at 90^o loading angle. The shear component increased and the normal component of the load decreased as the loading angle was

increased from 0 to 90 degrees. As in Chapter 3, two different specimen configurations are studied: a) 1-2 specimens, in which the 0^o layers are perpendicular to the notch direction and b) 2-1 specimens, in which the 0^o layers are parallel to the notch direction. Two different off-axis specimens were also tested in biaxial fatigue. In addition to presenting the fatigue test data, a new fatigue life prediction model is proposed in this chapter and fatigue damage development under biaxial loading was considered.

4.2 Experimental

4.2.1 Material

The material used in this study is a 3.3-mm thick E-glass fiber reinforced epoxy laminate composed of 13 layers and a stacking sequence described by $[0/90/0_9/90/0]$. In this laminate, 85 percent of the layers contained 0^o layers and 15 percent contained 90^o layers. The original trade name for the material was Scotchply 1002 and it was developed by 3M, Inc. It is now available by the trade name Cyply 1002 from Read Seal Electric Co. Both Scotchply and Cyply laminates were used in this research. They are identified in this chapter as SM and CM, respectively. The nominal fiber volume fraction in the laminate is 45 percent. The longitudinal tensile modulus and strength, as reported by the laminate manufacturers, are 39.3 GPa and 965.3 MPa, respectively.

4.2.2 Specimen

Small butterfly-shaped Arcan specimens with an overall size of 75 mm x 50 mm and two opposing notches at the mid-length were used in the fatigue tests. The notch angle was 90^o and the notch root radius was 10 mm. The specimen thickness was 3.3 mm. The significant section area between the notch roots was 76.82 mm^2. The specimen dimensions are shown in Figure 4-1.

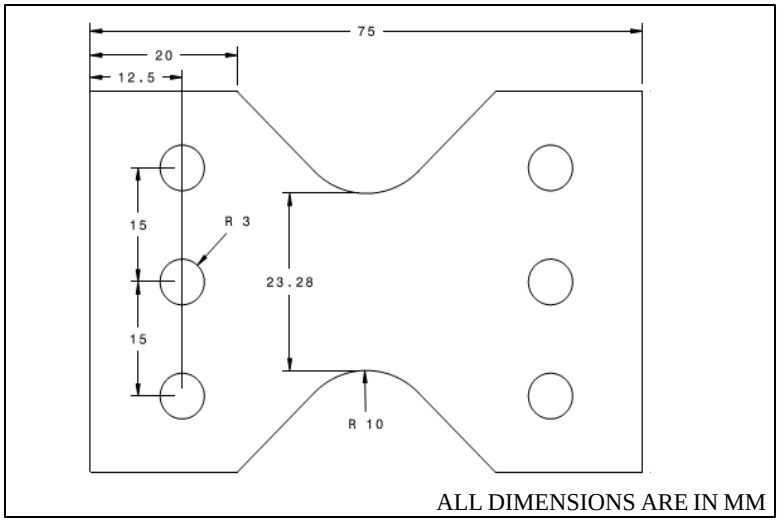

Figure 4-1: Dimensions of butterfly-shaped Arcan specimens used in this study. (thickness = 3.3 mm).

Two different specimen configurations were prepared: 1) the '1-2 specimens' or the longitudinal specimens in which the 0° layers were at a 0^o angle with the length direction of the specimen and 2) the '2-1 specimens' or the transverse specimens in which the 0° layers are at a 90^o angle with the length direction of the specimen. Figure 4-2 shows a schematic of the 1-2 and 2-1 specimens. In this figure, the 0° layers are represented by the solid lines and the 90° layers are represented by the dotted lines. In the 1-2 specimens, 11 of the 13 layers or 85%5% of the layers were the 90^o layers. As can be seen in Figure 4-2, the 0^o layers in the 1-2 and 2-1 specimens were perpendicular and parallel to the significant section, respectively. In addition to the aforementioned specimens, 30° and 45° off-axis small Arcan specimens were also used and tested under monotonic loading. In these specimens, the 0^o layers were at 30^o and 45^o angles to the length direction of the specimen.

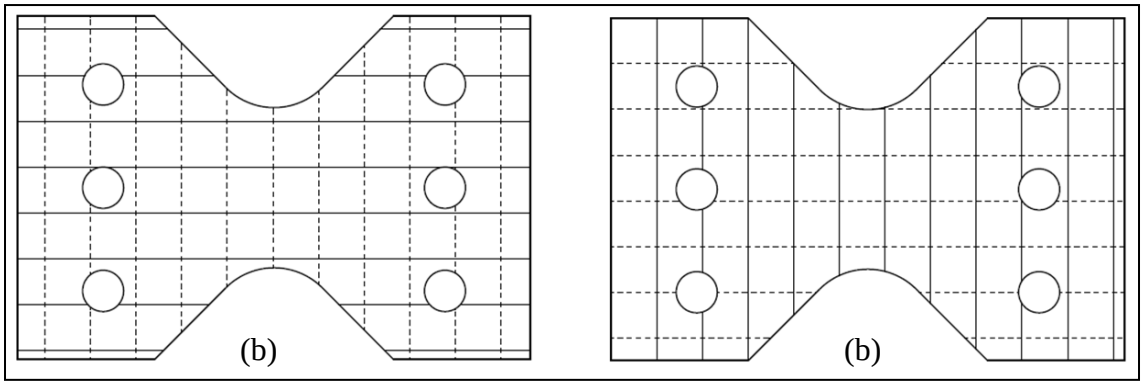

Figure 4-2: (a) 1-2 and (b) 2-1 configuration of the Arcan specimen.

4.2.3 Fatigue Test Procedure

Load-controlled tension-tension fatigue tests were conducted at room temperature using an MTS 810 servo-hydraulic test system. The fixture used for testing Arcan specimens is shown in Figure 4-3. The design of the fixture and specimen mounting method are described in Chapter 3. A cyclic frequency of 2 Hz was selected for all fatigue tests to reduce the possibility of specimen heating under cyclic loads. The maximum cyclic load was based on the peak load observed in monotonic biaxial tests and was in the range of 28 to 76% of the tensile peak load. The fatigue load ratio R (= P_{max}/P_{min}) used for all the tests was 0.1. During each test, both load and crosshead displacement signals were continuously recorded as a function of number of accumulated cycles at a rate of 100 Hz. Since the crosshead displacement increased with increasing number of cycles, the specimen stiffness determined from the slope of the load-displacement plot decreased. It was observed that the maximum and minimum cyclic loads stabilized and attained the designated load values within the first 100 cycles. Since the specimen can have a large decrease in stiffness before total rupture or separation, the cycle at which the instantaneous stiffness became half the stiffness at 100 cycles was considered the failure cycle. If a specimen did not fail in 2×10^6 cycles, cycling was discontinued and the test was considered a run-out.

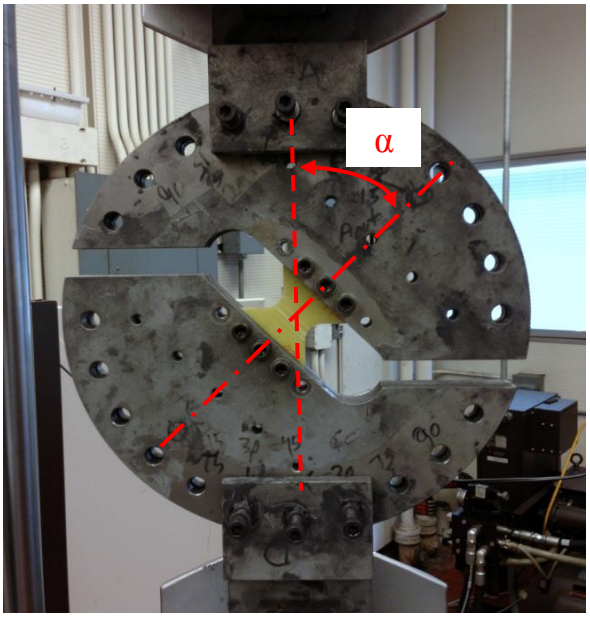

Figure 4-3. Photograph of an Arcan specimen mounted on the test fixture. The loading angle is denoted by α and is measured from the vertical axis of the loading fixture.

4.2.4 Fatigue Test Matrix

Table 4-1 shows the specimen configurations and loading angles at which the fatigue tests were conducted. For the 1-2 configuration, fatigue tests were not conducted at 0^o loading angle, since in monotonic tests, most of these specimens failed at the bolt holes instead of the significant section. For the other specimen configurations and loading angles, at least two specimens were fatigue tested for each loading condition. It is to be noted that the as the loading angle α is increased, the shear stress component increases and the normal stress component decreases. The normal stress components for the 1-2 and 2-1 specimens are σ_{xx} and σ_{yy}, respectively. For the 30 and 45^o specimen configurations, both normal components σ_{xx} and σ_{yy} are present. In addition, the shear stress component τ_{xy} is also present.

Table 4-1: Specimen configurations and the loading angles used for fatigue tests.

Loading Angle, α (°)	Specimen Configuration			
	1-2 (0^o)	2-1 (90^o)	30^o	45^o
0	-	Yes	Yes	Yes
30	Yes	Yes	-	-
45	Yes	Yes	-	-
60	Yes	Yes	-	-
90	Yes	Yes	-	-

4.3 Results

4.3.1 Load-Based Fatigue Response Diagrams

Figure 4-4 shows the maximum fatigue load vs. cycles to failure diagram obtained with 1-2 specimens. The fatigue performance of 1-2 specimens decreased with increasing loading angle; however, the difference in fatigue performance became smaller as the loading angle approached 90°. Thus, the effect of decreasing normal component and increasing shear component of the load was to reduce the fatigue performance. The lowest fatigue performance was observed at 90° loading angle, i.e., under the pure shear loading condition.

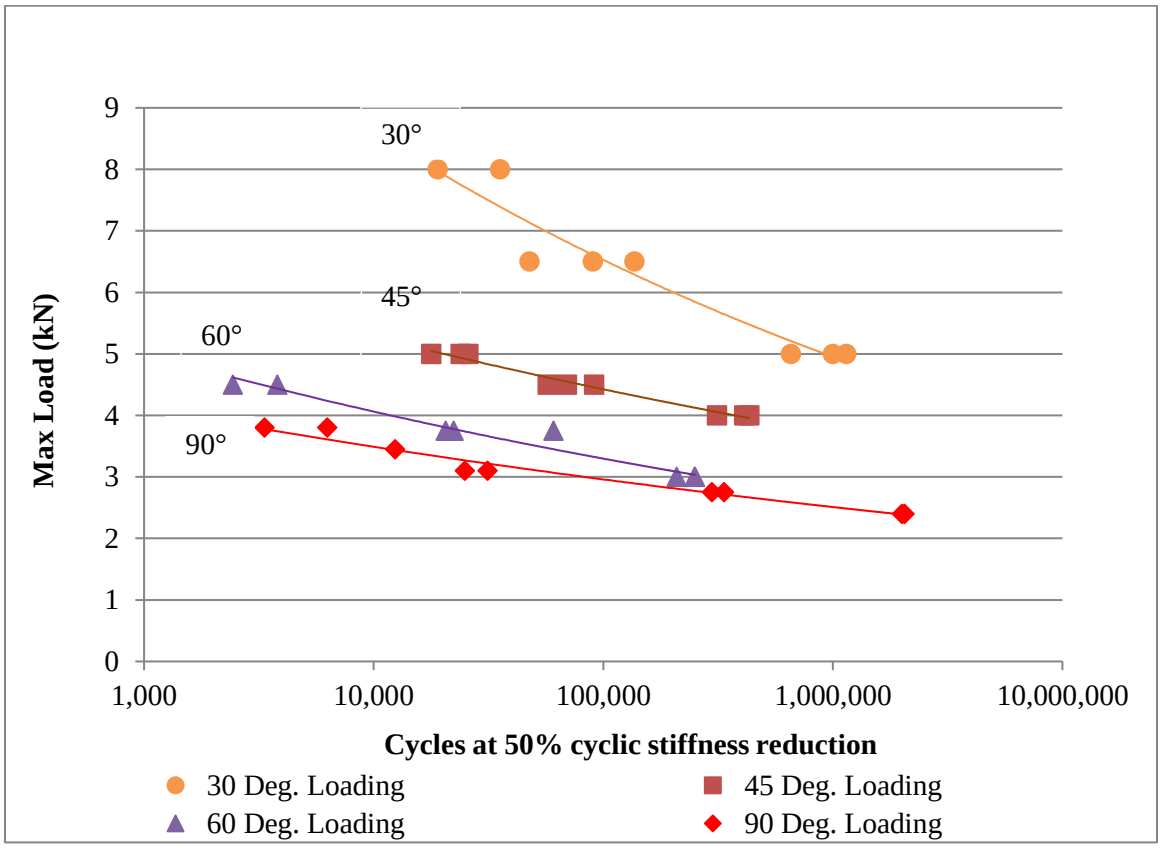

Figure 4-4: Fatigue tests results for small Arcan 1-2 specimens

Figure 4-5 shows the maximum fatigue load vs. cycles to failure diagram obtained with 2-1 specimens. The fatigue performance of the material in the 2-1 configuration was much higher at 0° loading angle than at 30° loading angle. As with 1-2 specimens, it

decreased with increasing loading angle and the difference in fatigue performance became very small as the 90° loading angle was approached.

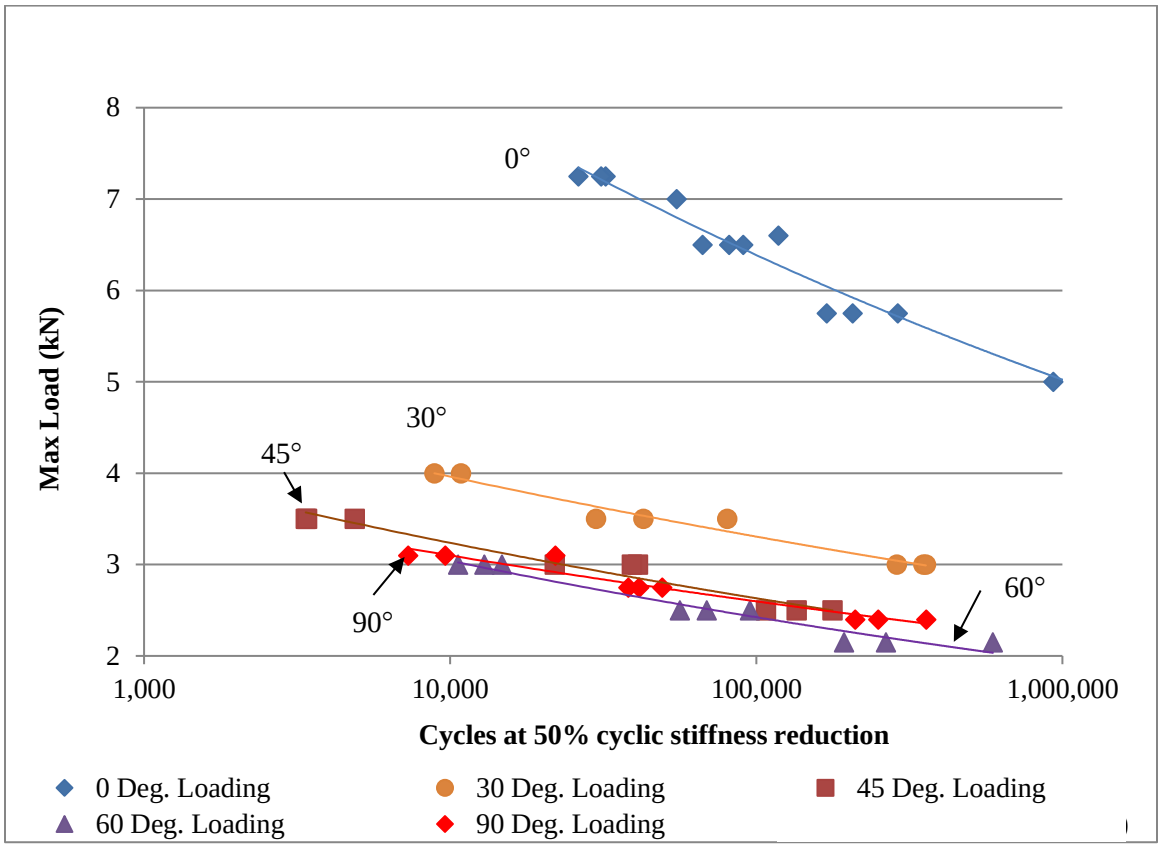

Figure 4-5: Fatigue tests results for small Arcan 2-1 specimens

Figure 4-6 shows the fatigue performance of the both 1-2 and 2-1 specimens under shear loads. Since the loading angle was 90^{o}, specimens in both configurations were subjected to only shear load and there were no normal stress components. As Figure 4-6, shows the 1-2 specimens performed better than 2-1 specimens under shear loading.

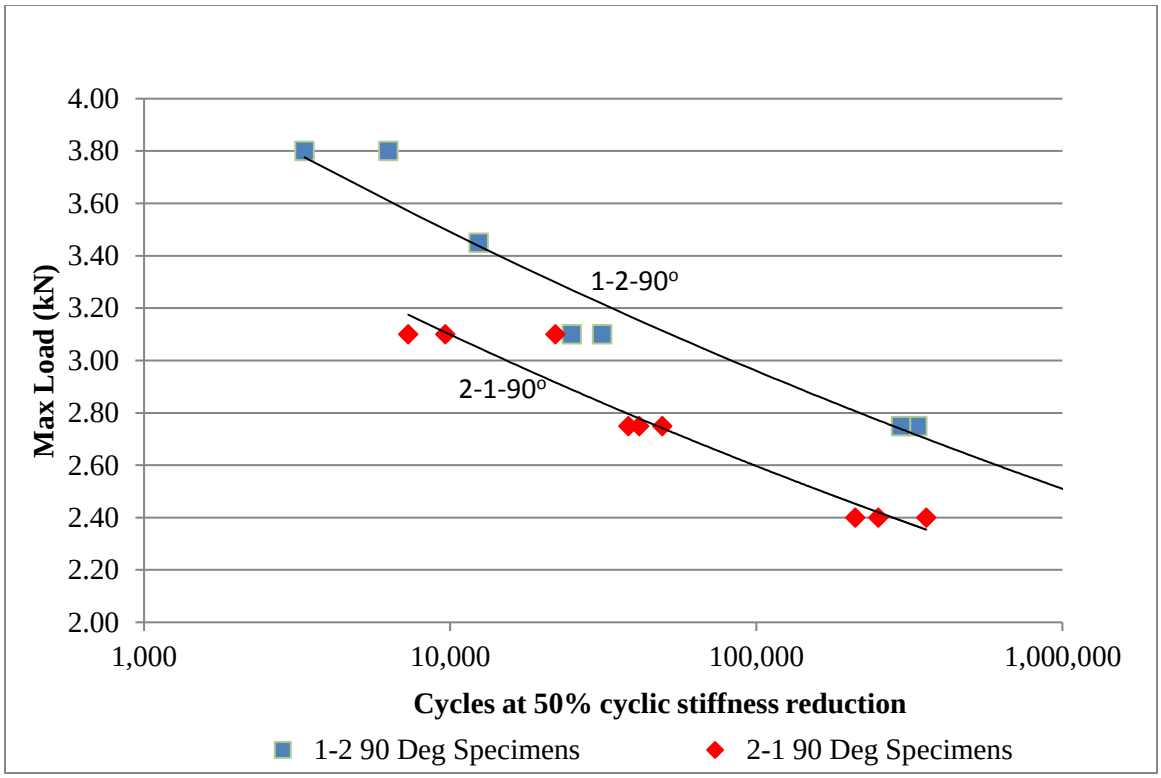

Figure 4-6: Fatigue performance of small Arcan specimens under shear load (Loading angle = 90º)

The fatigue performance of 30 and 45º specimen configurations is shown in Figure 4-7. The loading angle for these specimens was 0º. Figure 4-7 also shows the fatigue performance of the 1-2 specimens tested at loading angles of 30 and 45º. It is seen that the performance of the 1-2 specimens at 30º loading angle degrees is higher than the 30º specimens at 0º loading angle. The fatigue performance of 45º specimens at 0º loading angle and 1-2 specimens at 0º loading angle is very similar.

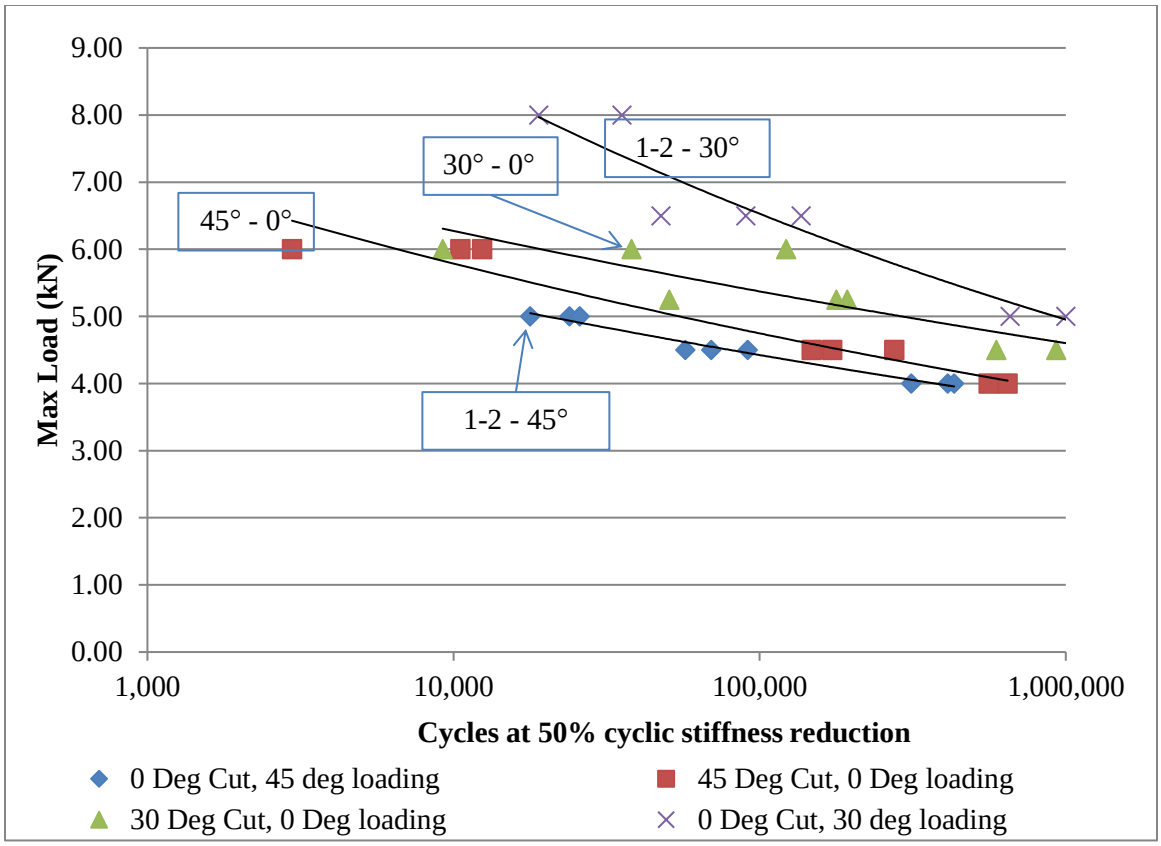

Figure 4-7: Fatigue performance of off-axis specimens at 0° loading angle and 1-2 specimens at 45° loading angle.

4.3.2 Stress-Based Fatigue Response Diagrams

In reporting load-controlled uniaxial fatigue data, it is customary to plot the fatigue response diagram using the maximum normal stress instead of maximum load as the fatigue parameter. In biaxial fatigue tests, there are two in-plane normal stresses, σ_{xx} and σ_{yy}, and a shear stress, τ_{xy}. The effects of all three stresses are represented by the normal and shear stress biaxiality ratios defined by the following equations.

(1) For the 1-2 specimens,

$$\lambda_y = \frac{\sigma_{yy}}{\sigma_{xx}} \tag{4.1}$$

$$\lambda_{xy} = \frac{\tau_{xy}}{\sigma_{xx}} \tag{4.2}$$

(2) For the 2-1 specimens,

$$\lambda_x = \frac{\sigma_{xx}}{\sigma_{yy}} \tag{4.3}$$

$$\lambda_{xy} = \frac{\tau_{xy}}{\sigma_{yy}} \tag{4.4}$$

Table 4-2 and Table 4-3 list the biaxiality ratios for the specimen configurations used for evaluating fatigue performance of small Arcan specimens.

Table 4-2: Specimen configurations and biaxiality ratios of small 1-2 Arcan specimens

Specimen Configuration	Loading angle (°)	λ_y	λ_{xy}
1-2	30	0	0.58
	45	0	1
	60	0	1.73
	90	0	∞
30°	0	0.33	0.57
45°	0	1	1

Table 4-3: Specimen configurations and biaxiality ratios of small 2-1 Arcan specimens

Specimen Configuration	Loading angle (°)	λ_x	λ_{yx}
2-1	0	0	0
	30	0	0.58
	45	0	1
	60	0	1.73
	90	0	∞
30°	0	3	1.73
45°	0	1	1

Figure 4-8 and Figure 4-9 are plotted with the maximum normal stress component acting on the 1-2 and 2-1 specimens along the y axis. Both plots include the data for 30 and 45^o specimens tested at 0^o loading angle. Since the maximum normal stress σ_{xx} for 1-2 specimens tested at 90^o loading angle is zero, the data points for this angle lie on the x-axis instead of a fatigue curve. The same is true for 2-1 specimens for

which the maximum normal stress σ_{yy} is zero tested at 90° loading angle. Figure 4-8 shows that for $\lambda_y = 0$, the fatigue performance is reduced as λ_{xy} is increased. By comparing the fatigue curves corresponding to $\lambda_y = 0$, 0.33 and 1, it can also be observed that the fatigue performance is reduced as λ_y is increased. Similar observations can be made in Figure 4-9. Thus, both normal stress biaxiality and shear stress biaxiality have adverse effects on the fatigue performance of the composite laminate considered here.

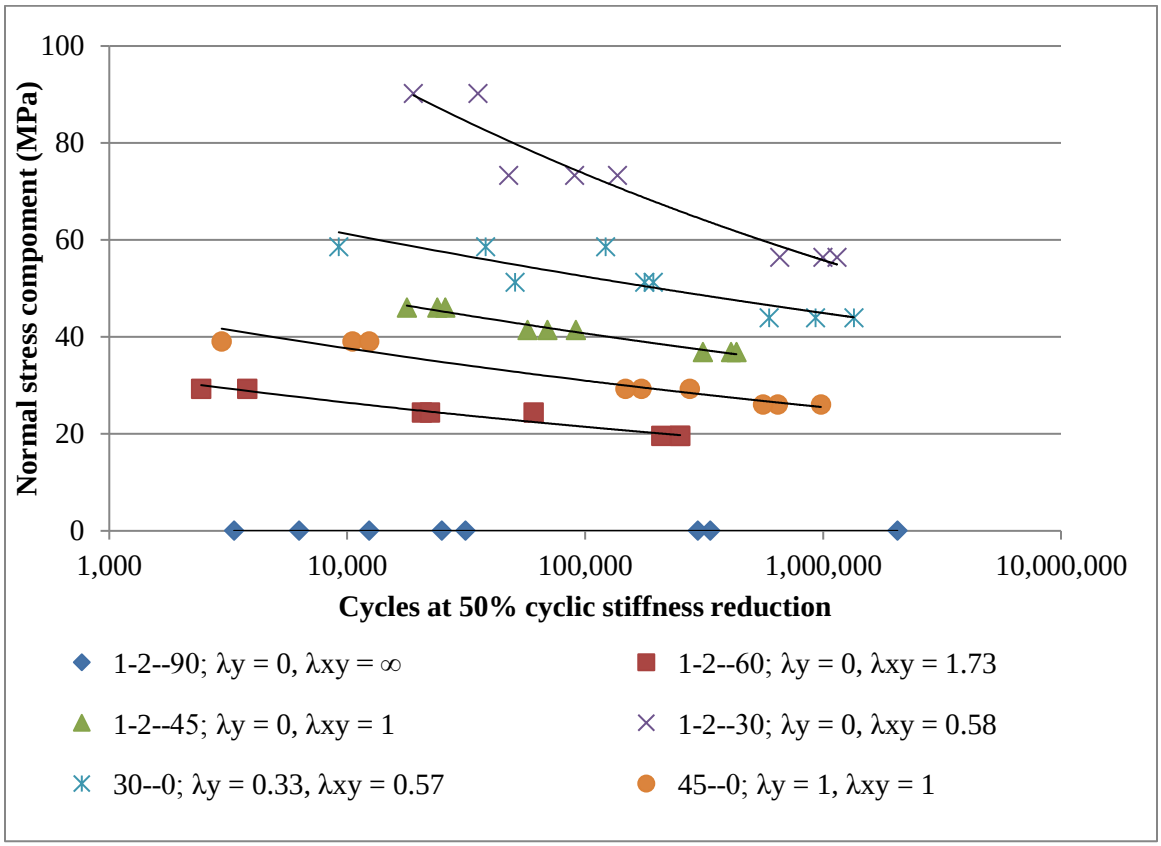

Figure 4-8: Fatigue behavior of 1-2, 30 and 45° specimens based on the normal stress component, σ_{xx}.

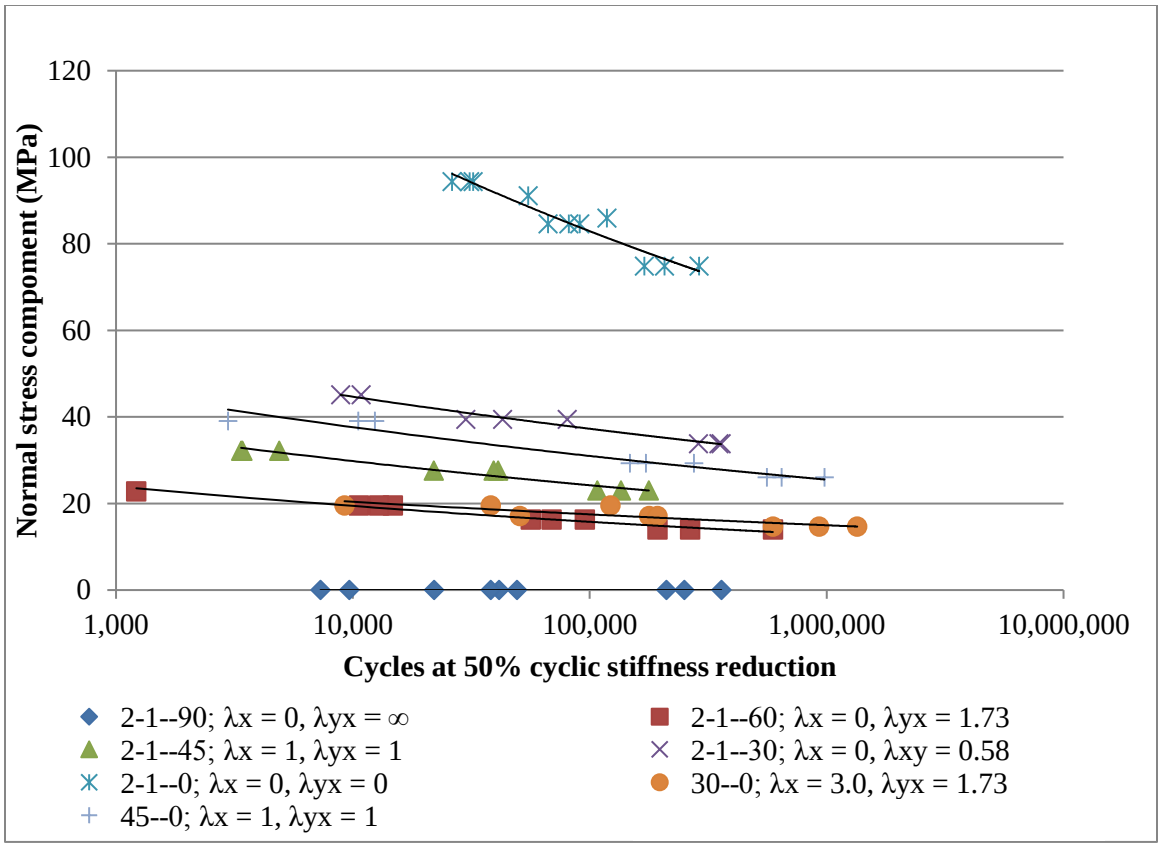

Figure 4-9: Fatigue behavior of 2-1, 30 and 45° specimens based on normal stress component, σ_{yy}.

In Figure 4-8 and Figure 4-9, the y-axis represents the maximum normal stress in fatigue cycling. There are two problems with this representation: (1) it cannot show the fatigue curves for pure shear tests in which the maximum normal stress is zero and (2) it does not take into account the combined effect of normal and shear stresses. For these two reasons, fatigue curves were generated with the maximum major principal stress representing the y-axis on the stress-life plots. The major principal stress was calculated from the following equation.

$$\sigma_{major} = \frac{1}{2}\left(\frac{\sigma_{xx}+\sigma_{yy}}{2}\right) + \sqrt{\left(\frac{\sigma_{xx}-\sigma_{yy}}{2}\right)^2 + \tau_{xy}^2} \qquad (4.5)$$

In terms of biaxiality ratios,

$$\sigma_{major} = \frac{\sigma_{xx,yy}}{2}\left[\left(1+\lambda_{y,x}\right)+\sqrt{\left(1-\lambda_{y,x}\right)^2+\lambda_{xy,yx}^2}\right] \qquad (4.6)$$

Using σ_{major} as the vertical axis, the fatigue curves were redrawn for different values of λ_{xy} and λ_{yx} in Figure 4-10 and Figure 4-11. The effects of increasing normal and shear biaxiality ratios are similar to the ones observed in Figure 4-8 and Figure 4-9. In both cases increasing normal and shear biaxialities reduce fatigue performance.

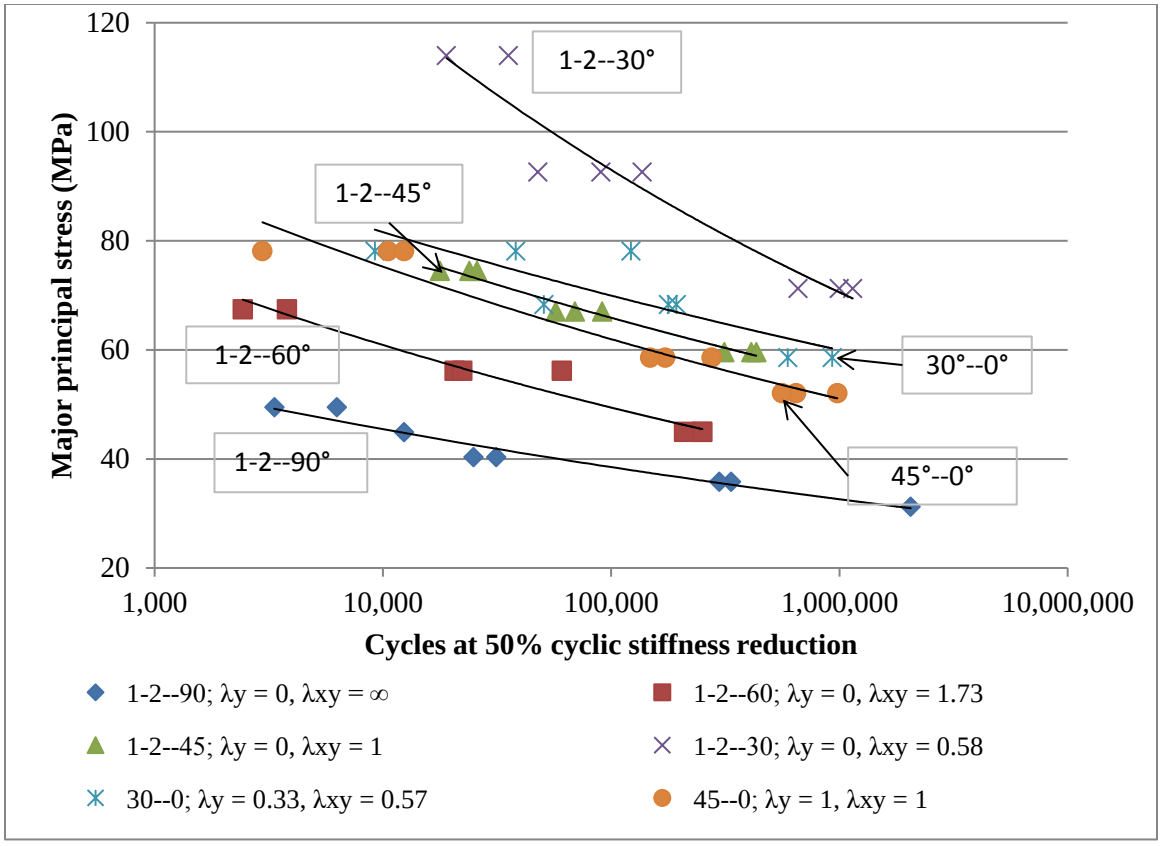

Figure 4-10: Fatigue behavior of 1-2, 30° and 45° specimens based on major principal stress.

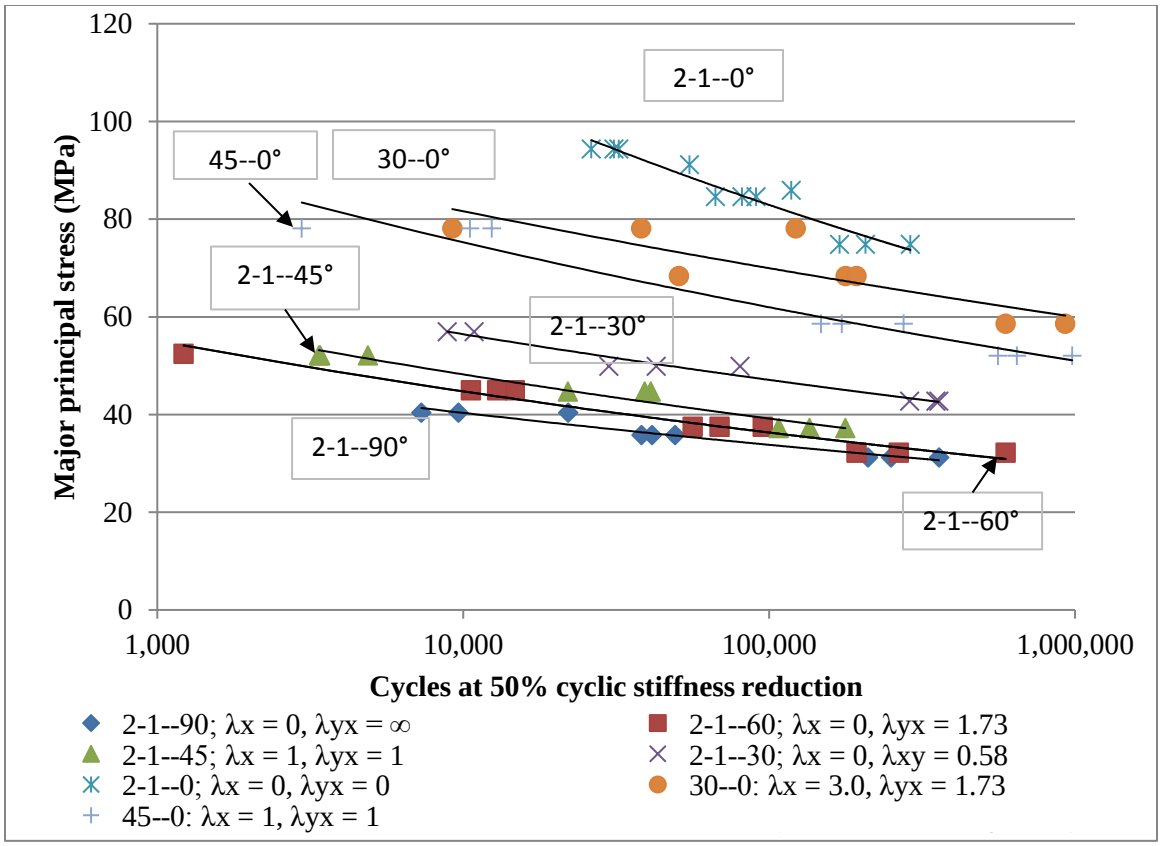

Figure 4-11: Fatigue behavior of 2-1, 30° and 45° specimens based on major principal stress.

4.3.3 Fatigue Life Prediction Model

The fatigue curves shown in Figure 4-10 and Figure 4-11 show that the fatigue life increases as the major principal stress is decreased. Within the range of major stresses considered, no fatigue limit was observed. Based on the data presented in Figure 4-10 and Figure 4-11, the following fatigue life prediction model is proposed

$$\sigma_{major} = AN_f^{-b} \tag{4.7}$$

where, σ_{major} is the major (maximum) principal stress and is calculated from Equation (4.6) using the maximum σ_{xx} and biaxiality ratios in each fatigue test. The left hand side of Equation (4.7) takes into account the normal and shear stress biaxiality ratios in the biaxial fatigue tests. A and b are determined be fitting Equation (4.7) to the fatigue data. The values of A and b are listed in Tables 4-4 and 4-5. It can be observed in both tables that A is a function of biaxiality ratios. For λ_y and λ_x, it decreases with increasing λ_{xy}. No particular trend can be observed for b.

Table 4-4: Fatigue parameters of 1-2 and off-axis specimens

Specimen Configuration	Loading angle (°)	λ_y	λ_{xy}	A	b
1-2	30	0	0.58	370.06	-0.12
	45	0	1	158.74	-0.076
	60	0	1.73	140.32	-0.091
	90	0	∞	80.327	-0.072
30°	0	0.33	0.57	151.11	-0.067
45°	0	1	1	163.82	-0.084

Table 4-5: Fatigue parameters of 2-1 and off-axis specimens

Specimen Configuration	Loading angle (°)	λ_x	λ_{yx}	A	b
2-1	0	0	0	297.14	-0.111
	30	0	0.58	116.43	-0.079
	45	0	1	110.59	-0.09
	60	0	1.73	103.12	-0.091
	90	0	∞	81.831	-0.077
30°	0	3	1.73	151.11	-0.067
45°	0	1	1	163.82	-0.084

4.3.3 Fatigue Damage Accumulation

Figure 4-12 shows the fatigue damage accumulated on 1-2 specimen surfaces fatigue tested at 30, 45, 60 and 90 loading angles. They all contain longitudinal shear cracks and delaminations along the fiber lengths. The majority of the fatigue damage accumulation occurred in the gage section and there is evidence of slight shear buckling of the 0^o fibers. There were also damages at the two diagonally opposite areas where the notch radius meets the slanted side of the specimen.

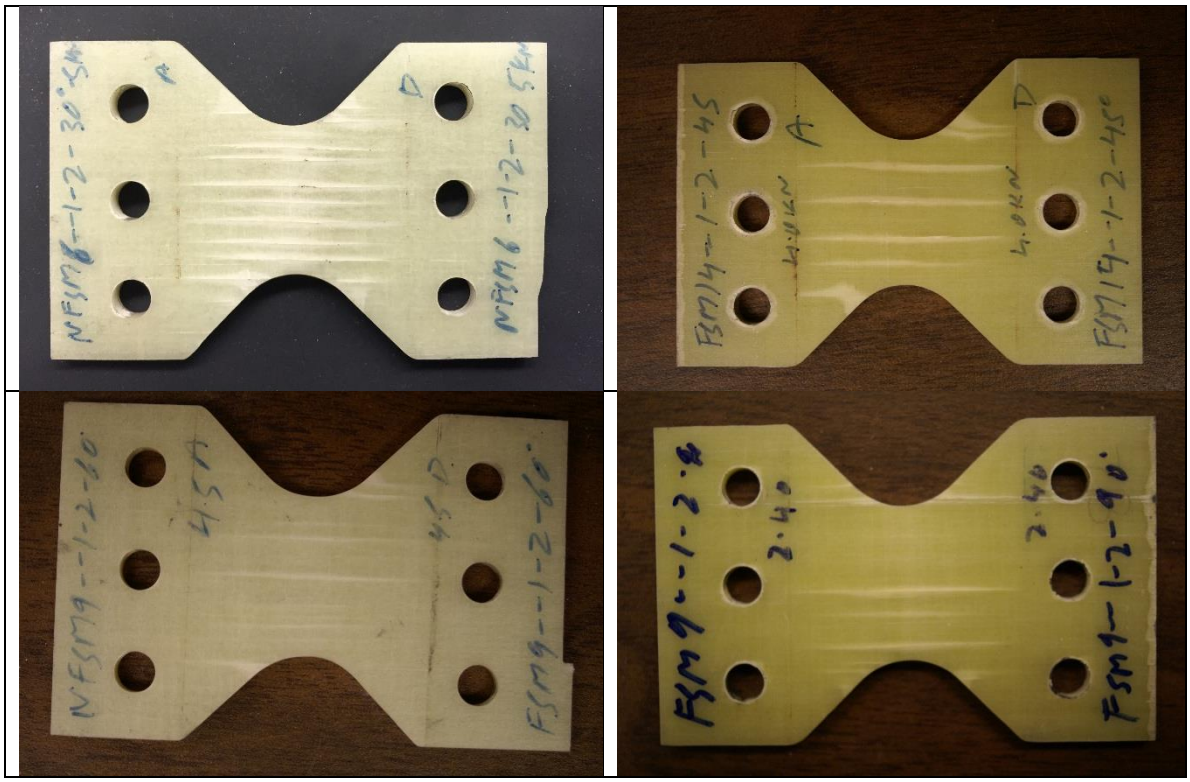

Figure 4-12: (Clockwise from top left to bottom left) Fatigue damage on small 1-2 specimens loaded at 30°, 45°, 60° and 90° loading angle.

Figure 4-13 shows the damage accumulation on the 2-1 specimen surfaces fatigue tested at 30, 45, 60 and 90 loading angles. Multiple shear cracks and slight delamination along their lengths can be seen at the notch root of all four specimens. Like the 1-2 specimens, 2-1 specimens also have damage that originated from the two diagonally opposite areas where the notch radius meets the slanted side of the specimen

Figure 4-14 shows the damage accumulation on the surfaces of 30° and 45° off axis specimens fatigue tested at 0° degree loading angle. It is seen that cracks on both these specimen surfaces followed the respective fiber angle on the surface. There was also considerable delamination surrounding these cracks.

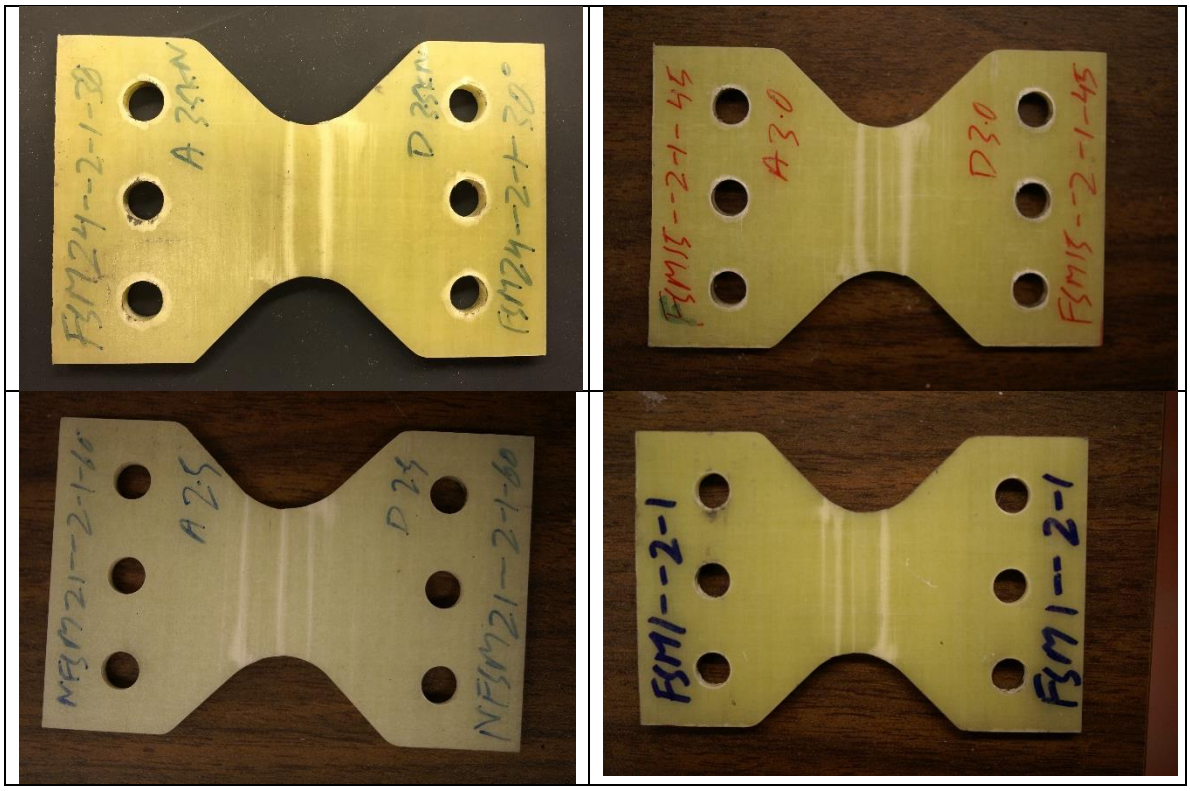

Figure 4-13: (Clockwise from top left to bottom left) Failure surface of small 2-1 specimens loaded at 30°, 45°, 60° and 90° loading angle.

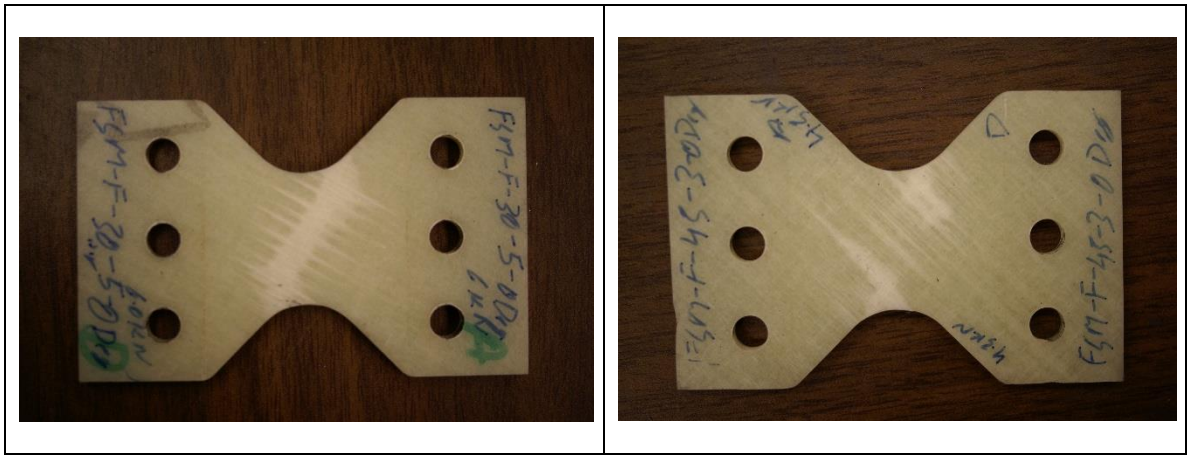

Figure 4-14: (Left to right) Failure surface of small 30° and 45° off axis specimen at 0° loading angle.

4.3.4 Stiffness Degradation

During load-controlled cycling of fatigue specimens, the instantaneous stiffness defined by the ratio of the maximum load and the maximum displacement decreased due

to increase in the maximum displacement with increasing number of cycles. This phenomenon, known as stiffness degradation, occurred due to continuous accumulation of damage in the specimens with increasing number of cycles. Figure 4-15 and Figure 4-16 show stiffness degradations for several 1-2 and 2-1 specimens at different loading angles. In these figures, the maximum cyclic stiffness is defined as follows.

$$Kmax = \frac{Maximum\ cyclic\ load}{Displacement\ at\ maximum\ cyclic\ load}$$

It can be seen for all test configurations that the stiffness degradation can be divided into two regions: 1) slow and progressive stiffness degradation followed by 2) fast and accelerating stiffness degradation. The change from the slow and progressive to fast and sudden stiffness degradation occurs at a knee. Even though there is large amount of scatter, it appears that the higher the maximum fatigue load, the higher is the stiffness degradation. The rate of stiffness degradation in the slow and progressive region is higher with increasing fatigue load.

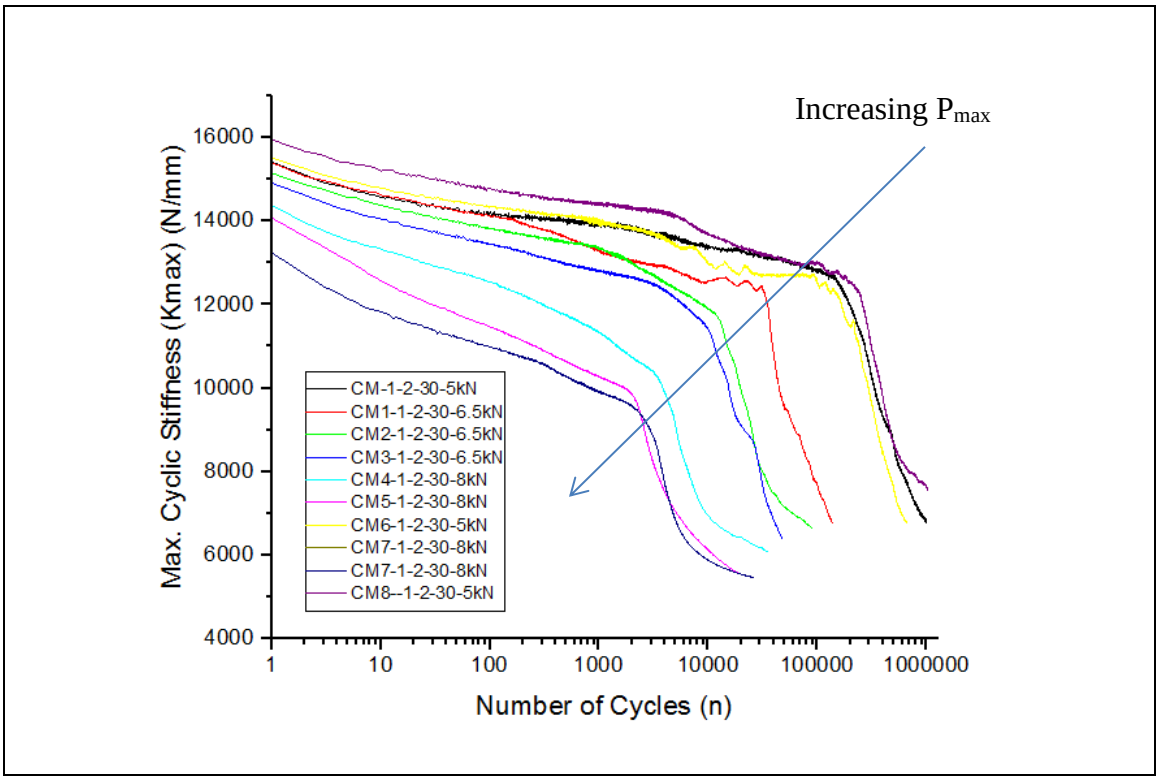

(a) 1-2 specimens at 30° loading angle

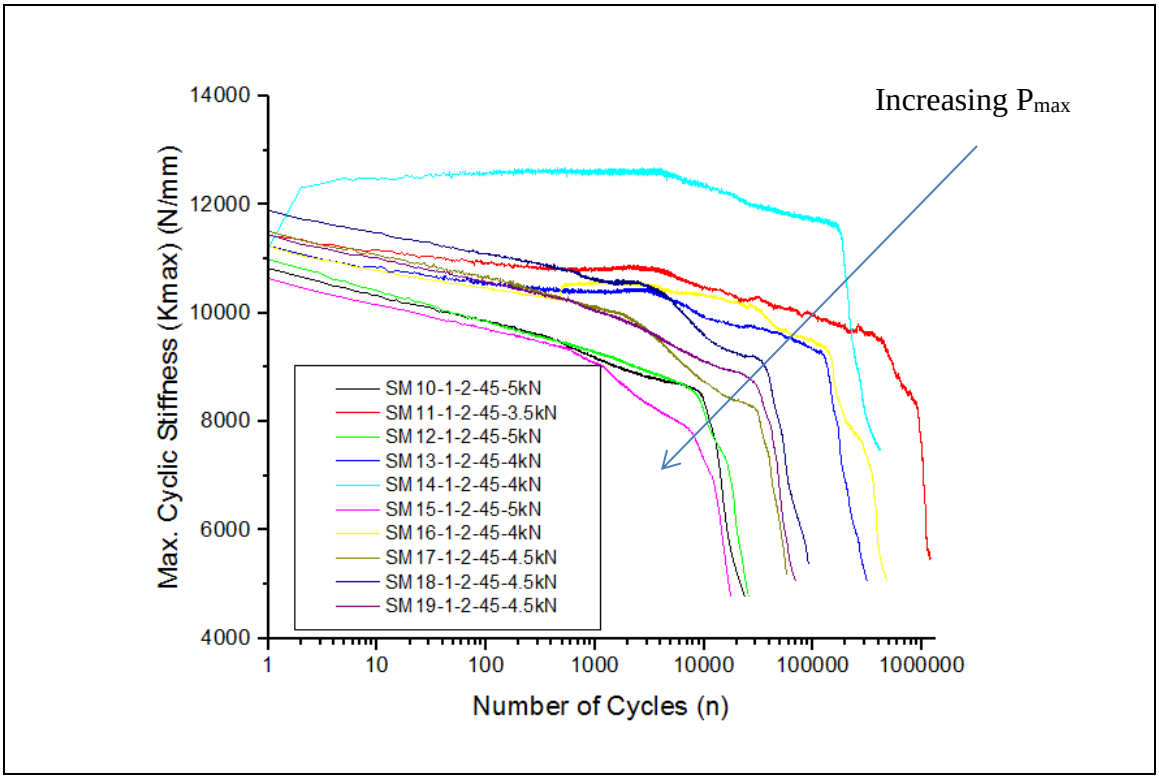

(b) 1-2 specimens at 45° loading angle

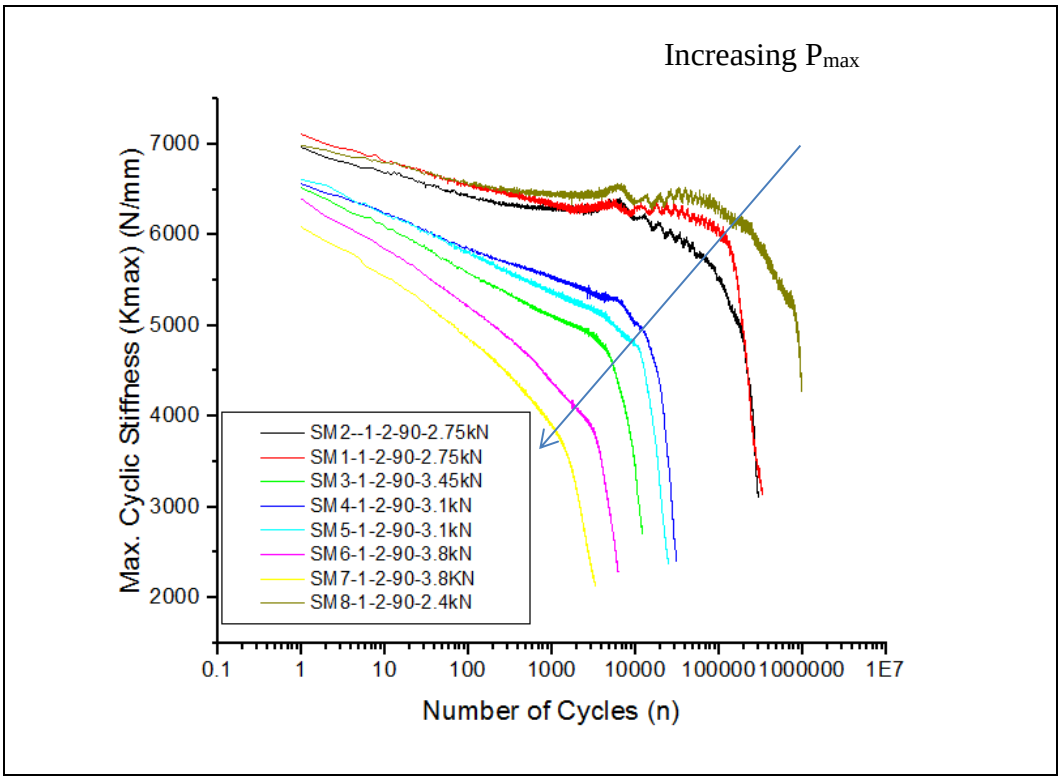

(c) 1-2 specimens at 90^{o} loading angle

Figure 4-15: Maximum cyclic stiffness of small 1-2 specimens as a function of number of accumulated fatigue cycles.

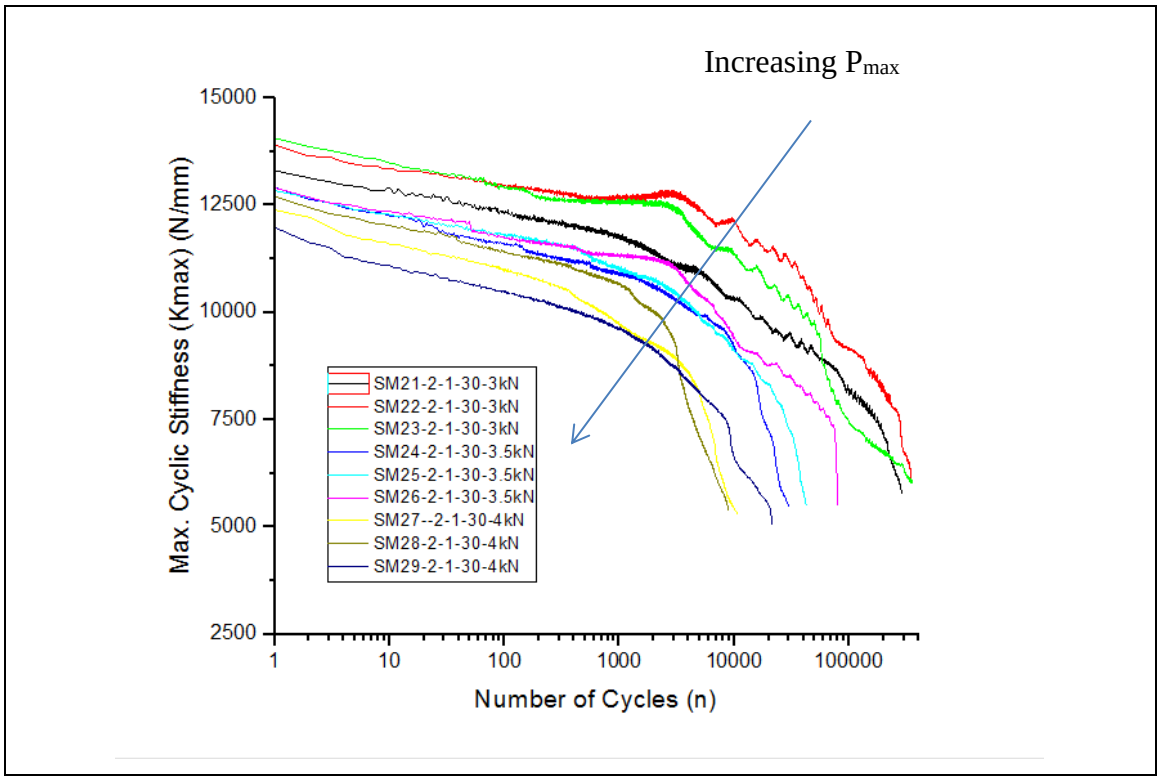

(a) 2-1 specimens at 30° loading angle

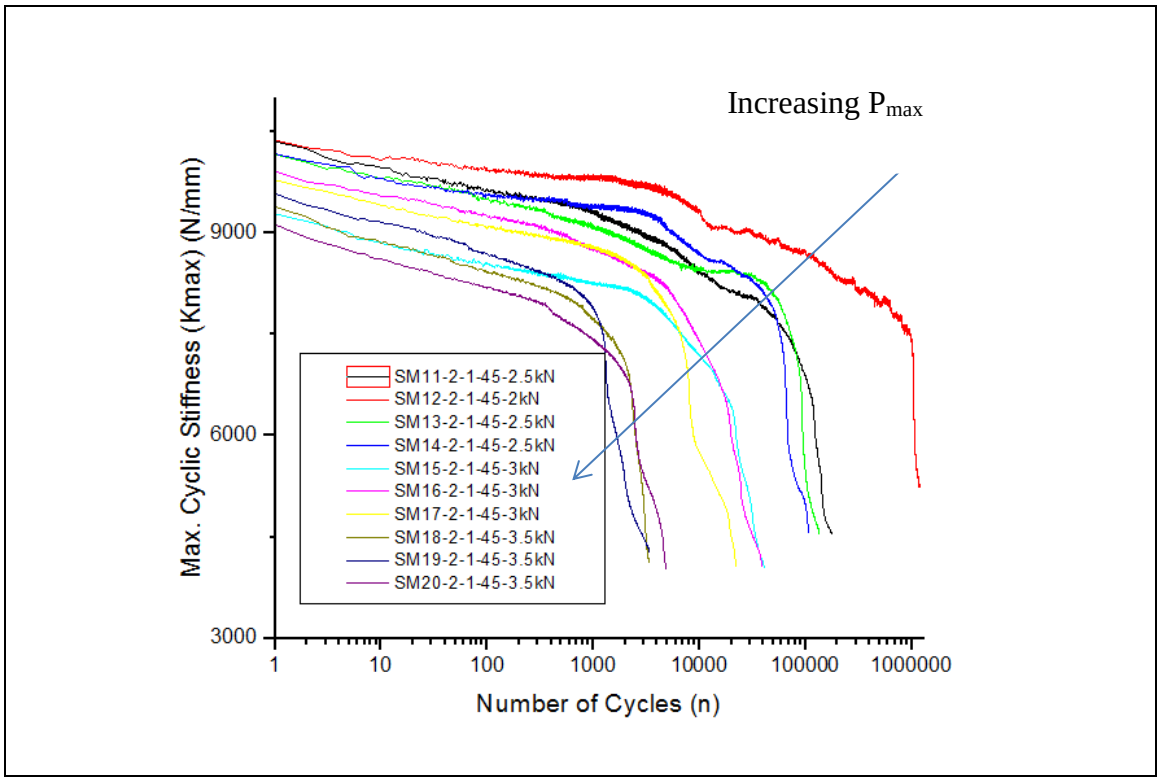

(b) 2-1 specimens at 45° loading angle

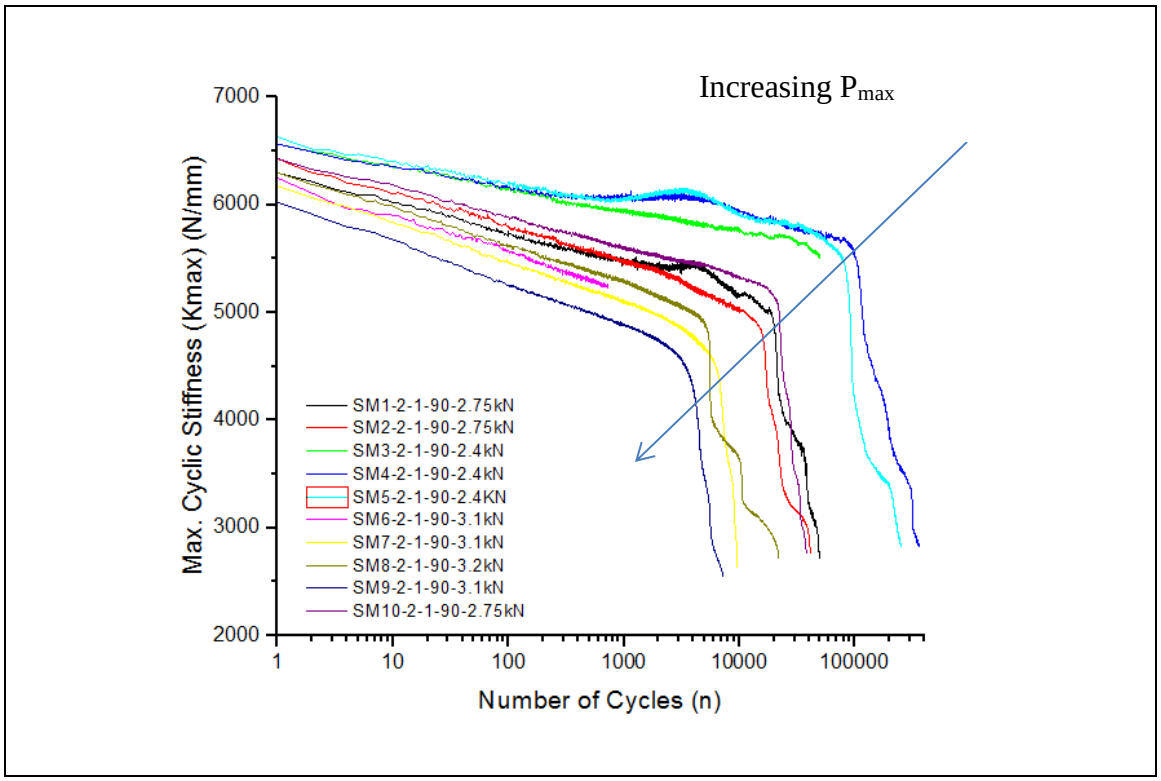

(c) 2-1 specimens at 90^o loading angle

Figure 4-16: Maximum cyclic stiffness of small 2-1 specimens as a function of number of accumulated fatigue cycles

4.4 Conclusions

In this chapter, a butterfly shaped Arcan specimen was used for biaxial fatigue testing of an E-glass fiber reinforced epoxy laminate under combined normal and shear loadings. Several different specimen configurations and loading angles were used to develop fatigue failure diagrams with different levels of stress biaxiality. It was shown that increasing shear stress biaxiality decreases the fatigue performance of the laminate. Increasing normal stress biaxiality also decreases the fatigue performance. A fatigue life prediction model is proposed which accounts for stress biaxiality. Fatigue damage occurred predominantly by shear failure. Stiffness degradation analysis shows that the material displays a knee region before which the stiffness reduction is gradual and slow, whereas after reaching the knee region the material displays a fast decrease in stiffness.

The Arcan specimen was found to be suitable for generating biaxial fatigue data for flat composite laminates in which both normal and shear stresses are present. The advantage of the Arcan test over other biaxial tests is that both normal and shear stress biaxialities can be easily varied by varying the loading angle and/or changing the fiber orientation angle. The fatigue tests conducted in this study demonstrated this advantage. However, more work needs to be done to validate the test method with different types of laminates and loading conditions.

4.5 References

[1] K. L. Reifsnider, Ed., *Fatigue of Composite Materials*. Amsterdam ; New York: Elsevier, 1991.

[2] B. Harris, Ed., *Fatigue in Composites: Science and Technology of the Fatigue Response of Fibre-Reinforced Plastics*. Boca Raton: CRC Press, 2003.

[3] P. K. Mallick, *Fiber-Reinforced Composites: Materials, Manufacturing, and Design*, 3rd ed., [Expanded and Ed.]. Boca Raton FL: CRC Press, 2008.

[4] A. P. Vassilopoulos, *Fatigue life prediction of composites and composite structures*. Boca Raton; Oxford: CRC Press; Woodhead Publishing, 2010.

[5] M. Quaresimin, L. Susmel, and R. Talreja, "Fatigue behaviour and life assessment of composite laminates under multiaxial loadings," *International Journal of Fatigue*, vol. 32, no. 1, pp. 2–16, 2010.

[6] M. Quaresimin, "50th Anniversary Article: Multiaxial Fatigue Testing of Composites: From the Pioneers to Future Directions," *Strain*, vol. 51, no. 1, pp. 16–29, 2015.

[7] Y. Xiao, M. Kawai, and H. Hatta, "An integrated method for off-axis tension and compression testing of unidirectional composites," *Journal of Composite Materials*, vol. 45, no. 6, pp. 657–669, Oct. 2010.

[8] M. Kawai and N. Honda, "Off-axis fatigue behavior of a carbon/epoxy cross-ply laminate and predictions considering inelasticity and in situ strength of embedded plies," *International Journal of Fatigue*, vol. 30, no. 10–11, pp. 1743–1755, Oct. 2008.

[9] M. Kawai and K. Kato, "Effects of R-ratio on the off-axis fatigue behavior of unidirectional hybrid GFRP/Al laminates at room temperature," *International Journal of Fatigue*, vol. 28, no. 10, pp. 1226–1238, Oct. 2006.

[10] M. Kawai, S. Yajima, A. Hachinohe, and Y. Kawase, "High-temperature off-axis fatigue behaviour of unidirectional carbon-fibre-reinforced composites with different resin matrices," *Composites Science and Technology*, vol. 61, no. 9, pp. 1285–1302, Jul. 2001.

[11] G. Schneider, "Evaluation of lamina strength criteria by off-axis tensile coupon tests," *Fibre Science and Technology*, vol. 5, no. 1, pp. 29–35, Jan. 1972.

[12] J. H. Sinclair and C. C. Chamis, "Fracture modes in off-axis fiber composites," *Polymer Composites*, vol. 2, no. 1, pp. 45–52, Jan. 1981.

[13] P.-Y. Chang, J.-M. Yang, H. Seo, and H. T. Hahn, "Off-axis fatigue cracking behaviour in notched fibre metal laminates," *Fatigue & Fracture of Engineering Materials and Structures*, vol. 30, no. 12, pp. 1158–1171, Dec. 2007.

[14] M. Kawai and H. Suda, "Effects of Non-Negative Mean Stress on the Off-Axis Fatigue Behavior of Unidirectional Carbon/Epoxy Composites at Room Temperature," *Journal of Composite Materials*, vol. 38, no. 10, pp. 833–854, May 2004.

[15] A. Plumtree, "A fatigue damage parameter for off-axis unidirectional fibre-reinforced composites," *International Journal of Fatigue*, vol. 21, no. 8, pp. 849–856, Sep. 1999.

[16] A. Varvani-Farahani, “A Fatigue Damage Parameter for Life Assessment of Off-axis Unidirectional GRP Composites,” *Journal of Composite Materials*, vol. 40, no. 18, pp. 1659–1670, Jan. 2006.
[17] J. Radon and C. Wachnicki, “Biaxial fatigue of glass fiber reinforced polyester resin,” in *Multiaxial Fatigue*, K. Miller and M. Brown, Eds. 100 Barr Harbor Drive, PO Box C700, West Conshohocken, PA 19428-2959: ASTM International, pp. 396–412.
[18] E. W. Smith and K. J. Pascoe, “Biaxial fatigue of a glass–fibre reinforced composite. Part 1: Fatigue and fracture behaviour,” in *Biaxial and Multiaxial Fatigue (EGF 3)*, M. W. Brown and K. J. Miller, Eds. London: Mechanical Engineering Publications, 1989, pp. 367–396.
[19] R. F. Foral and W. D. Humphrey, “Biaxial stress behavior of graphite and Kevlar 49 fiber/epoxy composites and hybrids,” *AIAA Journal*, vol. 22, no. 1, pp. 111–116, 1984.
[20] P. H. Francis, D. E. Walrath, D. F. Sims, and D. N. Weed, “Biaxial Fatigue Loading of Notched Composites,” *Journal of Composite Materials*, vol. 11, no. 4, pp. 488–501, Oct. 1977.
[21] S. Amijima, T. Fujii, and M. Hamaguchi, “Static and fatigue tests of a woven glass fabric composite under biaxial tension-torsion loading,” *Composites*, vol. 22, no. 4, pp. 281–289, Jul. 1991.
[22] P. Francis, D. Walrath, and D. Weed, “First ply failure of G/E laminates under biaxial loadings,” *Fibre Science and Technology*, vol. 12, no. 2, pp. 97–110, Mar. 1979.
[23] D. Qi and G. Cheng, “Fatigue behavior of filament-wound glass fiber reinforced epoxy composite tubes under tension/torsion biaxial loading,” *Polymer Composites*, vol. 28, no. 1, pp. 116–123, Feb. 2007.

CHAPTER 5 : CONCLUSIONS

5.1 Conclusions

Using finite element analysis, the effects of notch radius, notch angle, specimen size, specimen material, clamping condition and fixture material on the stress distribution in the significant section of a butterfly-shaped Arcan specimen were examined with the final intent of designing a specimen that can be used for biaxial testing of fiber reinforced composite laminates. Since the presence of opposing notches creates stress non-uniformity in the significant section (notch plane) of the specimen, the extent of stress uniformity was considered the measure of effectiveness for the specimen design. Based on this measure, a notch radius of 10 mm and a notch angle of 90^o are the optimum notch dimensions for 1-2 specimens. However, a smaller radius is found to be better for 2-1 specimens. Out of the two specimen sizes considered, the smaller specimen with overall outer dimensions of 75 mm x 50 mm produces a more uniform stress distribution than the larger specimen with overall outer dimensions of 75 mm x 75 mm. The difference in stress distribution in the unclamped and clamped specimens is very small when the specimen is either in tension or shear mode of loading. For combined loading modes, the clamped specimens produce higher stresses, which can be attributed to the horizontal reaction loads generated at the loading ends of the clamped specimen. It is shown that the magnitude of the horizontal reaction load depends on the ratio of the fixture stiffness and specimen stiffness, specimen size, loading angle as well as fiber orientation angle. Large specimen with a high ratio of fixture stiffness to specimen stiffness produces a smaller horizontal reaction load.

Validity of using Arcan specimen to determine the quasi-static characteristics of composite laminates under a combination of tensile normal stress and shear stress is established. The material used in the study was an E-glass fiber reinforced epoxy and the laminate configuration was $[0/90/0_9/90/0]$. Though the same test method can be applied to other laminates and can be developed to characterize composite laminates under a

combination of compressive normal stress and shear stress. Unlike the tubular specimens commonly used for characterizing biaxial strength properties, the Arcan test specimens can be used for flat laminates. Also unlike the tubular specimen which requires special manufacturing processes and test equipment, the Arcan specimen fabrication and test fixture are relatively simple and the Arcan test arrangement can be easily fitted in the universal testing machines used for mechanical characterization of materials. It can be used to generate a wide range of biaxial normal stresses and in-plane shear stress, which makes it a very versatile test method for composite materials.

It was shown that the strength of E-glass fiber reinforced epoxy laminates under combined tensile normal stress and shear stress fits a quadratic envelope. The load-displacement diagrams exhibit a knee at which failure initiation occurs. Above the knee load, the load-displacement diagrams become increasingly non-linear as the shear stress component increases. The knee and failure loads in the 2-1 configuration with 90^o layers are lower than in the 1-2 configuration with 0^o layers. Failure of the 2-1 specimens is due to shear buckling and matrix cracking in the significant section, while failure of the 1-2 specimens is a combination of matrix cracking and shear failure. The Azz-Tsai-Hill theory fits very well with the experimental failure envelope corresponding to the knee load.

Biaxial fatigue performance of the E-glass fiber reinforced epoxy laminate under combined normal and shear loadings was determined using the Arcan specimen. Several different specimen cofigurations and loading angles were used to develop fatigue failure diagrams with different levels of stress biaxiality. It was shown that increasing shear stress biaxility decreases the fatigue performance of the laminate. Increasing normal stress biaxiality also decreases the fatigue performance. A fatigue life prediction model is proposed which accounts for stress biaxiality. Fatigue damage was predominatly by shear faiure. Stiffness reduction analysis shows that the material displays a knee region before which the stiffness reduction is gradual and slow, whereas after reaching the knee region the material displays a fast decrease in the stiffness.

The Arcan specimen was found to be suitable for generating not only the biaxial tensile data but also the fatigue data for flat composite laminates in which both normal and shear stresses are present. The advantage of the Arcan test over other biaxial tests is

that both normal and shear stress biaxialities can be easily varied by varying the loading angle and/or varying the fiber orientation angle. Both tensile and fatigue tests conducted in this study demonstrated this unique advantage.

5.2 Recommendations and Scope of Future Work

The research conducted in this study has shown that butterfly-shaped Arcan specimens can be effective in determining biaxial strength and fatigue characteristics of composite laminates. However, research can be continued in the following areas to improve the Arcan specimen design and to further characterize composite laminates under biaxial loading conditions.

- Improvement in the Arcan specimen design to reduce stress concentrations at the ends of the notch radius tips. This may include both finite element analysis and experimental technique.
- Experimental determination of the side thrust/ horizontal reaction loads on the Arcan fixture to verify the values predicted by finite element analysis and development a corrective method to account for the horizontal reaction load.
- Application and verification of the test specimen and fixture with other laminates and loading configurations.
- Improvement of fatigue life prediction model using a mechanistic approach.
- Damage development model under biaxial loading and its dependence on biaxiality ratios through both experiments and finite element analysis.